ABSTRACT

Title of Document: FATIGUE TEST AND PROGNOSIS STUDY OF WELDED TUBULAR JOINTS IN SIGNAL SUPPORT STRUCTURES

Zhen Li, Doctor of Philosophy, 2013

Directed By: Dr. Yunfeng Zhang
Associate Professor
Department of Civil and Environmental Engineering

Steel welded tubular joints have been widely used in traffic signal support structures for economic and aesthetic reasons. However, they are susceptible to fatigue cracking which may lead to structural failure such as collapse, thus pose a threat to driver's safety. To address this issue, this study is focused on fatigue test, modeling and prognosis of the fatigue crack growth in full-scale welded tubular joints of traffic signal support structures.

Fatigue test of six full-scale welded tubular joint specimens fabricated based on real design for signal support structure is conducted to obtain crack growth data. Details of test setup and results are reported in this dissertation. Two types of fatigue crack

growth models are proposed for two regimes of fatigue crack development in welded tubular joints: the linear elastic fracture mechanics (LEFM) model for the slow crack growth regime (denoted as Stage II here) and the empirical failure model for the rapid crack growth regime (denoted as Stage III). Details of these two models including their mathematical expressions, stochastic parameters, sensitivity analysis and model application, are given in the dissertation.

A sensor-driven structural health prognosis procedure that has an explicit stochastic measurement error term and thus can model the sensor performance degradation over monitoring period is proposed. The prognosis procedure involves the Bayesian theorem and Markov Chain Monte Carlo (MCMC) sampling for updating the structural degradation model using sensor data. An extreme value theory (EVT) based tail fitting method is proposed to reduce the heavy burden on data transmission and computing involved in sensor driven prognosis. This method employs moment estimator to calculate the small quantiles of the prognosis results by using a small portion of available sensor data.

Finally, fatigue test data acquired in this study are used to examine the proposed fatigue life prognosis procedure. Both the LEFM based fatigue crack growth model and the empirical failure model are studied for fatigue life prognosis application. Prognosis results show that the prognosis procedure is able to provide good estimate of the fatigue crack growth curve of welded tubular joints in signal support structures if certain conditions are met.

FATIGUE TEST AND PROGNOSIS STUDY OF WELDED TUBULAR JOINTS IN SIGNAL SUPPORT STRUCTURES

By

Zhen Li

Dissertation submitted to the Faculty of the Graduate School of the
University of Maryland, College Park, in partial fulfillment
of the requirements for the degree of
Doctor of Philosophy
2013

Advisory Committee:
Associate Professor Yunfeng Zhang, Chair
Professor Amde M. Amde
Professor Bilal M. Ayyub
Research Professor Chung C. Fu
Professor Ali Mosleh

Acknowledgements

The work described in this dissertation was partially supported by a grant from the National Science Foundation under Grant No. CMMI-1031304.

I am deeply grateful to my advisor, Dr. Yunfeng Zhang for his years of significant support, guidance and contributions throughout this research. His wisdom, knowledge and commitment to the highest standards inspired and motivated me. I am also indebted to all my dissertation committee members, Dr. Amde M. Amde, Dr. Bilal M. Ayyub, Dr. Chung C. Fu and Dr. Ali Mosleh for their advices and assistances.

I would also like to express my deep thanks to my friends, Mr. Changjiang zhou, Mr. Linjia Bai, Mr. Feng Shi and Mr. Ruipeng Li for sharing innumerous days in the office and lab and for their encouragements and supports.

Finally, I would like to extend my special thanks to my parents for their endless love and unwavering support. Also I would like to thank my parents-in-law for their help. Most of all, I would like to express my deep gratitude and love to my wife, Ruli Xiao, for standing by my side all the time. Without her love, support and encouragement, the dissertation would not have been accomplished. A special thank is granted to my little boy Adam. His birth is a gift to my life, making it full of joys and happiness.

Table of Contents

List of Tables

List of Figures

Nomenclature

a:	:	crack depth
b	:	half plate width
A	:	constant in *S-N* equation
a_0	:	initial crack depth
a_c	:	critical crack depth
a/c	:	crack aspect ratio
$(a/c)_0$	:	initial crack aspect ratio
c	:	half the length of semi-elliptical surface crack
C	:	constant in Paris-Erdogan Law
D	:	cumulative damage in Miner's rule
DOB	:	degree of bending
G	:	constant in material failure equation
i,j	:	counters
K	:	stress intensity factor
K_c	:	fracture toughness
K_{op}	:	crack-tip-open stress intensity factor
$K_{\max}$	:	maximum stress intensity factor
$K_{\min}$	:	minimum stress intensity factor
$K_{app,max}$	:	applied maximum stress intensity factor
$K_{app,min}$	:	applied minimum stress intensity factor
L_w	:	Weld footprint length

m	:	exponent in Paris Law
M	:	bending moment
M_e	:	bending moment for equivalent load cycle
Mk_b	:	magnification factor for the bending stress case
Mk_m	:	magnification factor for the membrane stress case
n	:	total number of measurements
N	:	number of load cycle
N_0	:	initial load cycle
N_e	:	equivalent load cycle
P	:	shear force
$P_{\max}$	:	maximum shear force
$P_{\min}$	:	minimum shear force
P_f	:	probability of failure
R	:	stress ratio
R_t	:	external radius of the tube
t	:	time in service
t_0	:	initiation time
t_1		time in service at the first measurement
t_f	:	failure time from t_1
T	:	wall thickness
T_f	:	total fatigue life from t_0
X_p	:	p quantile
X_k	:	The k_{th} order statistic in n samples

y	:	degradation index
y_{cr}	:	critical degradation index value
Y	:	measurement vector
Y_b	:	correction factor for bending stress case
Y_m	:	correction factor for membrane stress case
α	:	parameter vector containing quantities related to system properties
β	:	environmental input vector
γ	:	extreme value index
γ_1	:	growth rate related parameter in empirical failure model
γ_2	:	constant in empirical failure model
δ	:	constant
ΔK	:	stress intensity factor range
ΔK_{th}	:	threshold stress intensity factor range
ΔK_{eff}	:	effective stress intensity factor range
ΔM	:	bending moment
ΔP	:	shear force range
$\varepsilon_{\mathrm{mdl}}$	:	model error
θ	:	weld toe angle
σ_b	:	bending stress
σ_m	:	membrane stress
σ_{mdl}	:	standard deviation of model error distribution
σ_{msm}	:	standard deviation of measurement error distribution
$\sigma_{\mathrm{hs,app}}$	:	applied hot-spot stress

Ω : quantity of precursor signals in empirical failure model

Chapter 1: Introduction

There have been a lot of fatigue induced structural collapses of cantilevered traffic signal support structures in many states in the United States (Dexter and Ricker 2002). Some of the accidents happen on highway and the signal mast arm falling over fast moving vehicle poses high threat to drivers. The study of the fatigue behavior of welded tubular joints in traffic signal structures has drawn growing attention in the past decade (Hartnagel and Barker 1999; Heeden 1999; Kashar *et al* 1999; Dexter and Ricker 2002; Ocel *et al* 2006). Most of the reported research work focus on fatigue design. In this dissertation study, the focus is the fatigue crack growth of the welded tubular joints in the signal support structures and how to use fatigue growth data for fatigue life prediction.

1.1 Research motivation

Tubular structures have become increasingly popular for economic and aesthetic reasons. Application of tubular elements in welded structures possesses several advantages, the main among them being low weight characteristics, reached owing to optimum geometric characteristics of sections and reduction of external loadings on the structure (Lobanov and Garf 1998). So far, tubes with different shape of sections (e.g. circular hollow section (CHS), rectangular hollow section (RHS)) are frequently used in structures such as traffic signal support structures, cranes, wind turbine supports, bridges and offshore structures etc. These sections are generally connected by welding. Many of them contain CHS or RHS members and connections that employ circumferential fillet welds.

Despite the popularity of the tubular structures in application, brittle failures subsequent to fatigue cracking have been observed. There have been many reports of cracking in the tubular structures in the vicinity of the welded connections (Dexter and Ricker 2002). Fatigue cracks typically start at highly stressed locations such as weld terminations of specific structural details. The stresses reach peak values near the weld toe of the joints. The fatigue performance of welded tubular connections is of particular importance for the safety of welded steel tubular structures subjected to repeated loading such as signal support structures. The traffic signal support accidents in the USA (Hartnagel and Barker 1999; Heeden 1999; Kashar *et al* 1999; Dexter and Ricker 2002; Ocel *et al* 2006) have demonstrated the criticality of fatigue growth modeling and prognosis of this type of tubular structure in order to develop an effective strategy for fatigue monitoring and maintenance scheduling.

Fatigue behavior of welded tubular structure has been extensively studied in the past decades while a large portion of the research work has been done on offshore structures and bridges. In comparison with the tubular joints in offshore structures and bridges, welded tubular joints commonly found in signal support structures exhibit notable differences such as member dimensions (both absolute and relative), the loads affecting the joint, and joint fabrication procedures. For example, a major difference between tubular structure in bridges and signal support structure lies in the thickness of the tubes. The thickness of the tube wall in signal support structure is much smaller, usually at the level of 6 to 10 mm (Kaczinski *et al* 1998) while tubes with wall thickness up to 70 mm is not uncommon in bridges (Dauner *et al* 1998). Evidences from the fatigue tests (Schumacher and Nussbaumer 2006) have

demonstrated the effect of size on the fatigue strength of welded tubular joints. Therefore, research on welded tubular joints in signal support structures is needed to contribute to the knowledge base on welded tubular structure such as determining the parameter values of fatigue growth model.

As for the existing research related to fatigue problem of tubular joints in traffic signal support, most of them are on the fatigue resistance evaluation and design issues (e.g., Kaczinski *et al* 1998, Fouad *et al* 2003, Dexter and Ricker 2002). Not much study has been reported on its crack growth modeling and fatigue life prognosis. In order to study the fatigue crack growth behavior of the welded tubular joints in traffic signal support structures, fatigue test has to be conducted to obtain experimental data on the crack growth behavior. Meanwhile, models that describe the fatigue crack growth behavior are in need. For fatigue crack growth model, a commonly used one is the Paris Law (Paris *et al* 1961). Bowness and Lee (1999) modified the Paris law to adapt it to the welded tubular joints in offshore structure and bridges. The limitation of the Paris law is that it is only applicable to fatigue stage II. For the failure stage of fatigue stage III, however, not much research has been done on how to model it. Yet it is of great interest since catastrophic failure could happen in this ultimate stage. If the crack growth can be properly modeled, collapse can be predicted to avoid potential catastrophic failure caused by fatigue cracking.

Besides the modeling of fatigue crack growth, another important issue about tubular joints fatigue problem is how to implement the prognosis of its fatigue life. Lots of research has been conducted on the development of fatigue prognosis methods. However, currently available structural health prognosis methods are mostly based on

conventional nondestructive testing (NDT) data, which has limited availability in both time and space. With emerging monitoring system featuring continuous and online data collection, conventional health prognosis method needs to be revised to accommodate new features and requirements for a sensor-driven health prognostic system such as continuous sensor data stream and sensor performance variation. For example, during long term monitoring project, the sensor itself could degrade in its performance. How to model the sensor degradation and its effect on prognosis result are important research topics. Also, as online structural health monitoring (SHM) system can provide continuously collected sensor data on demand, how to effectively utilize the abundant sensor data is another question being raised in practice since transmitting and processing large amount of sensor data requires considerable communication bandwidth and computing resource. A notable method is to only use those monitoring data with significant values that exceed a pre-specified performance threshold (Frangopol *et al* 2008; Strauss *et al* 2008). However, this method discards most of the information and the obtained result is deterministic. Since small quantiles or extreme values of the prognosis results (e.g. Remaining Useful Life (RUL)) are often of more interest, an alternative solution could be the use of tail fitting techniques (e.g. the extreme value theory (EVT)) to obtain the prognosis result. Yet how to apply the tail fitting techniques in fatigue prognosis needs to be explored.

1.2 Research objectives and scopes

The primary goal of this research is to study the fatigue crack growth and fatigue life prognosis for steel welded tubular joints in traffic signal support. To accomplish this goal, the following specific objectives are defined: (1) select proper models for

fatigue crack growth modeling at different stages of the fatigue process; (2) conduct full-scale fatigue test of welded tubular joints from signal support structures and record the crack propagation pattern during the fatigue test; (3) develop a sensor-driven structural health prognosis procedure which is applicable to fatigue problems; (4) apply the proposed fatigue model and the prognosis procedure to welded tubular joints using fatigue test data and examine their performance in the tubular joints fatigue problem.

To achieve the above objectives, the following analytical and experimental research tasks are carried out for this research:

(1) A linear elastic fracture mechanics (LEFM) model and an empirical failure model are introduced for fatigue crack growth modeling of welded tubular joints in traffic signal structure. The LEFM model is modified from the Paris Law to describe the fatigue crack propagation behavior of welded tubular joints in traffic signal structure. Factors and parameters of the model are discussed. The empirical failure model applies to fatigue stage III. It directly includes the fatigue life as an explicit parameter in the equation. Details and discussions of these two models are provided such as model derivation, model parameters, sensitivity study and limitations, etc.

(2) Fatigue tests of six full-scale welded tubular joints specimens from traffic signal support. The specimens comprised of CHS mast arm welded to transverse plate are fabricated based on real signal support design for the state of Maryland. MTS servo-hydraulic loading system is used to apply constant amplitude loading to the specimens. Beach-marking is implemented in one test specimen to observe

the crack growth behavior. Strain gauges are installed on specimens to obtain the stress data. Various nondestructive techniques (microscope, dye penetrant etc.) are used to track the crack propagation during the fatigue test. The crack surface features are also examined after test.

(3) A sensor-driven structural health prognosis procedure is proposed. The proposed procedure utilizes Bayesian theorem for updating of the structural degradation model. Markov Chain Monte Carlo (MCMC) sampling is used to calculate the posterior distributions of the stochastic parameters in the structural degradation model. Limit state function and risk acceptance level are defined to obtain the fatigue life. The prognosis procedure is extended to study the two features of sensor-driven prognosis: sensor performance degradation over long-term monitoring and excessive amount of data obtained from structural health monitoring system.

To incorporate the sensor performance degradation in long-term monitoring process, the error term in the structural degradation model is split into two terms: the measurement error term and the model error term. Stochastic process (e.g. Gaussian process, Wiener process) is used to represent the measurement error term. In order to effectively extracting key prognosis information from massive amount of sensor data that could be generated by on-line SHM system, an EVT based tail fitting method is proposed which can reduce the computation demand by 80% while still preserving key information.

(4) With the obtained data from fatigue test, the proposed fatigue prognosis procedure is applied to the fatigue test data to examine its performance in welded

tubular joints fatigue application. Both the LEFM model and the empirical failure model are employed as the degradation model for the prognosis of fatigue life in different fatigue stages respectively. Prognosis results such as crack growth curve and fatigue lives for both cases are compared and discussed.

1.3 Organization of dissertation

This dissertation is organized as follows: Chapter 2 reviews the current state of knowledge on tubular structure fatigue modeling and prognosis. Chapter 3 presents the two fatigue growth models: the LEFM model and the empirical failure model. Chapter 4 presents the test setup and results for the fatigue test of six full-scale welded tubular joint specimens. Chapter 5 describes a sensor-driven structural health prognosis procedure which utilizes Bayesian theory and the Markov Chain Monte Carlo (MCMC) sampling. Sensor degradation is introduced into the model by the measurement error term. An EVT based prognosis method is also described. In Chapter 6, the proposed fatigue models and the prognosis procedure are applied to welded tubular joints using the fatigue test data. Finally, Chapter 7 summarizes the major findings of this dissertation research and future work.

Chapter 2: Literature Review

This chapter reviews the state of knowledge of fatigue modeling and prognosis, in the context of welded tubular joints. The review is presented in two sections. Section 2.1 presents the general approaches of fatigue modeling followed by a brief description of fatigue tests conducted on welded tubular joints in traffic signal structures in Section 2.2. Section 2.3 introduces prognosis methods. Knowledge about nondestructive testing (NDT) based prognosis and sensor-driven prognosis is also presented in this section.

2.1 Fatigue modeling

2.1.1 Stress-life approach

The stress-life approach is the most commonly used approach in industry to estimate the fatigue life. This approach states that three factors determine the fatigue life of a steel structure: (1) the number of loading cycles the structure undertakes; (2) the stress range induced by the load at the fatigue detail location; (3) the type of structures including fatigue detail geometry and materials (Fisher *et al* 1998). A regression analysis of experiment data for a specific type of structural detail would reveal a linear relation between the logarithm of stress range and fatigue life. This forms the base of the AASHTO fatigue design rules. In the stress-life approach, the fatigue life of a specific steel structure can be expressed as Eqn. (2.1),

$$\log N = A - m\log(\Delta\sigma) \tag{2.1}$$

In Eqn. (2.1), N is the fatigue life (in cycles). m and A are the slope and intercept obtained from regression analysis of experiment data (Chotickai 2005). In the

AASHTO LRFD Bridge Design Specifications (3th edition, 2004), each type of steel structure is classified into fatigue category A to E'. For each category, the value of *A* is provided. For steel structure, *m* is approximately 3.0 for simplicity of use (Keating and Fisher 1986).

2.1.2 Linear elastic fracture mechanics method

Fatigue assessment based on linear elastic fracture mechanics (LEFM) is related to the stress distribution analysis in the vicinity of a crack tip. Since it is based on theory of elasticity, linear stress-strain relationship is assumed (Fisher *et al* 1998). In the LEFM approach, stress intensity factor *K* is defined to characterize the stress field around the crack tip. The stress intensity factor is a function of the crack size and the applied remote stress. It is often expressed as,

$$K = WY\sigma\sqrt{\pi a} \tag{2.2}$$

In Eqn. (2.2), σ represents the applied remote stress. *a* is the crack size (e.g. crack length, crack depth etc.). *Y* represents the correction of stress due to geometry of the structure and crack (e.g. semi-elliptical shape of the crack or existence of welded attachment at the crack tip etc.). *W* represents the non-uniform distribution of the stress around the crack tip caused by residual stress, stress concentration etc. (Fisher *et al* 1998) The detailed expression of Eqn. (2.2) would vary for different fatigue details. A great number of expressions for *W* and *Y* have been developed by researchers using either regression from experiment data or finite element analysis.

Paris and Erdogan (Paris *et al* 1961) developed the well-known equation as the Paris Law, which is given below as Eqn. (2.3).

$$\frac{da}{dN} = C\left(\Delta K\right)^m \tag{2.3}$$

In Eqn. (2.3), *da/dN* is the crack growth rate. *ΔK* is the stress intensity factor range which is the subtraction of K_{min} from K_{max}. *C* and *m* are material related constants. It can be observed from Eqn. (2.3) that linear relation exists between the logarithm of crack growth rate (*da/dN*) and the stress intensity factor range (*ΔK*). As the intercept and slope, *C* and *m* can thus be obtained from linear regression of fatigue test data.

Eqn. (2.3) can only be used for the stable stage of fatigue crack growth. It cannot be applied to the initiation stage or the final rapid crack growth stage. At the initiation stage, the crack growth is very slow and unpredictable. At the final stage, the crack growth rate accelerate rapidly and the linear relation between log(*da/dN*) and log(*ΔK*) no longer holds. Three stages are distinguished based on this. The initiation stage is considered as stage I. The linear stage shown in Figure 2.1 is considered as stage II and the final stage is considered as stage III. Also two limits are defined using the value of *K* for the fatigue crack growth. One limit is the threshold value ΔK_{th}. If *ΔK* is below ΔK_{th}, the crack would not propagate. The other limit is the facture toughness K_c. When the maximum stress intensity factor K_{max} approaches K_c, unstable crack growth would occur (Sobczyk and Spencer Jr 1992). Figure 2.1 shows the relation between *da/dN* and *ΔK*.

2.1.3 Cumulative fatigue damage analysis

As a linear cumulative fatigue damage theory, the Palmgren-Miner's rule is first proposed by Palmgren in 1924 and further developed by Miner in 1945 (Miner 1945). Based on the Palmgren-Miner's rule, the fatigue damage induced by cyclic loading is

defined as Eqn. (2.4).

$$D = \sum_{i=1}^{k} \Delta D_i = \sum_{i=1}^{k} \frac{n_i}{N_i} \tag{2.4}$$

In Eqn. (2.4), N_i is the fatigue resistance at stress range i. n_i is the loading cycles at stress range i. Palmgren-Miner's rule assumes that the damage fractions resulting from a specific stress range level is proportional to the number of load cycle applied at that stress range level. It neglects the effect of load sequence and average stress. The damage caused by each cycle in the load history is considered to be independent. Despite these assumptions, this method gives reasonable correlation with test data. It is advised by AASHTO LRFD Bridge Design Specifications (3rd Edition, 2004) to estimate the cumulative damage due to its ease of use.

2.2 Fatigue tests on tubular joints in signal support structure

Traffic signal support arm mast collapse has been seen in the past several decades (Dexter and Ricker 2002). After the accident in Michigan in 1990 (Culp *et al* 1990), AASHTO mandated the revision of the design code for traffic signal structures. Its fatigue problem started to draw more attention from researchers (Ocel *et al* 2006; Hartnagel and Barker 1999; Heeden 1999; Kashar *et al* 1999). A few experiments have been conducted to study the fatigue strength of welded tubular joints commonly found in traffic signal structures. Those experiments examined a variety of fatigue related design issues for the welded tubular joints in signal structures. A brief review of some of these experiments is provided next.

2.2.1 Test for fatigue resistance evaluation

An important objective of a majority of the fatigue tests on tubular joints in signal

support structure is to study the fatigue resistance (Gilani and Whittaker, 2000a, b; Koenigs 2003; Ocel *et al* 2006).

Gilani and Whittaker (2000a, b) conducted analytical and experimental study on fatigue behavior of traffic tubular structures. Four types of specimens tested, one with pole section and three with mast arms. Results show that the fatigue performance of the pole specimen is between Category D and C while the fatigue performance of the the mast arms is between Category E and D.

Valmont is a large company manufacturing signal support structures etc. It conducted fatigue test to proof-test its signal support structure design after the release of the 2001 AASHTO specifications (Ocel *et al* 2006). The tube-to-transverse plate connections were tested with three different details: fillet-welded sockets, fillet-welded sockets reinforced with gusset plates, and full-penetration welds. 20 specimens were tested. Results of the Valmont testing showed that the fatigue resistance described by the 2001 AASHTO Specifications for all details tested is conservative with only one exception.

Koenigs (2003) did experiment on mast arm socket connections to examine if it should be categorized as fatigue category E' detail. A total of 59 specimens were tested. Their test data falls into Category E' and it was concluded by Koenigs (2003) that the tested socket connection belongs to Category E' detail.

2.2.2 Test for stress evaluation

Researchers from Illinois Department of Transportation and University of Missouri-Columbia (South 1997) investigated the stress level and stress concentration for the traffic signal structure separately (South 1997; Alderson 1999).

In the second phase of the research conducted by South (1997) at the Illinois Department of Transportation Physical Research Laboratory, cantilevered signal structure was instrumented with strain gauges placed on the mast arms and the anchor bolts in their lab test. Wind load is simulated in the lab test. Rainflow data of the stress calculated from measurements are reported. Strain gauges were placed to measure the hot-spot stress. They were placed 0.79 mm away from the weld toe with the gauge grid center 1.20 mm from the weld toe. In order to calculate the stress concentration factor (SCF), the nominal stress range was also calculated from mechanics equations. With both hotspot stress and nominal stress, the calculated SCFs have a mean value of 1.78 and a standard deviation of 0.014.

For the research conducted by Alderson (1999) at the University of Missouri-Columbia, two real signal support structures were short-term monitored in field with strain gauges in addition to lab test of five specimens. The recorded maximum truck gust induced stress range was 14.1 MPa. The measured out-of-plane stresses caused by wind gust have larger value than the in-plane stresses. The percentage of out-of-plane stresses exceeding the CAFL is 35.1% while all the in-plane stresses were below it. Also, No observation about galloping was obtained.

2.2.3 Test for weld evaluation

A few researchers (Miki *et al* 1981; Alderson, 1999) have conducted fatigue test to study the fatigue strength of fillet welded tube-to-transverse-plate connections.

Miki *et al* (1981) conducted fatigue test of 12 specimens at Lehigh University. 6 of 12 specimens have equal-leg fillet welds and the other 6 specimens have unequal-leg fillet welds (longer weld on the tube side). The test result shows that equal-leg fillet

welds have a resistance slightly worse than Category E', and the unequal-leg fillet welds had a fatigue resistance slightly better than Category E'.

Researchers at the University of Missouri-Columbia (Alderson 1999) conducted research to investigate the fatigue problem of tubular joints in traffic signal structure. Five mast arm specimens were tested under constant amplitude fatigue loading with a stress range of 55.2 MPa. Three specimens have unequal weld leg and two with equal weld leg. Results do not suggest improved fatigue resistance with unequal weld leg design which is different from the conclusion drawn from tests conducted by Miki *et al* (1981).

2.2.4 Test for non-destructive method evaluation

Following the collapse of two cantilevered traffic signal poles in Wyoming (Deschamp 2002), the Wyoming Department of Transportation sponsored a research project to investigate non-destructive methods suitable for crack inspection of these structures including acoustic emissions (AE). The majority of the specimens tested were in-service structures. Test was also conducted using a hydraulic actuator to apply the cyclic loads. The actuator was operated in displacement control.

2.3 Fatigue prognosis

2.3.1 NDT based prognosis

Conventional NDT-data driven structural health prognosis techniques have been studied by researchers (see, e.g., Lu and Meeker 1993; Zhao *et al* 1994, 1996; Zheng and Ellingwood 1998; Enright and Frangopol 1999; Zhang and Mahadevan 2001; Chung *et al* 2006; Wang *et al* 2008). Madsen (1987) developed a strategy to use NDT

measurements to update the failure probability through a probabilistic degradation model. Lu and Meeker (1993) proposed a general degradation model with Gaussian error term of independent identical distribution (i.i.d) to predict the time-to-failure distribution. Zhao and Haldar (1994) studied the uncertainty in the NDT measurements and its effect on the prognosis procedure. Detectability and accuracy were explicitly modeled as two uncertainty sources in the measurements. Zhang and Mahadevan (2000) also used Bayesian theorem to update the selected probabilistic model for prognosis purpose. Robinson and Crowder (2000) extended the application of degradation model for prognosis by incorporating the Markov Chain Monte Carlo (MCMC) algorithm in the updating process. The MCMC algorithm enables sampling from posterior distribution of model parameters so more complicated degradation model can be used. Perrin *et al* (2007) also implemented Bayesian updating and MCMC simulation for fatigue fracture prognosis application. All these prognosis methods are based on the use of limited amount of NDT data.

2.3.2 Sensor driven prognosis

Sensor may degrade in its performance over long-term monitoring. However, not too much work has been done on incorporating the special features of sensors in a continuous monitoring system into structural health prognosis procedure. Gebraeel *et al* (2005) used stochastic procedures to model sensor measurements and derived a closed-form posterior distribution for both exponential and linear sensor degradation model. In their research, two stochastic models for general random error term were used and it was found that Wiener process fits the data better than the i.i.d. Gaussian process.

Popularity in using structural health monitoring (SHM) system to generate sensor data for quantitative condition assessment and prognosis is growing. Using multiple sensor data has the advantage of reduced uncertainty in general degradation model through estimating the likelihood function in Bayesian updating with measured data. In a study by Coppe *et al* (2009), all available sensor data were used for the prognosis to obtain the distribution of the likelihood function in Bayesian updating.

As online SHM system can provide continuously collected sensor data at demand, how to transmit massive sensor data is another question being raised in practice since transmitting and processing large amount of sensor data requires considerable communication bandwidth and computing resource. For example, the Wind and Structural Health Monitoring System (WASHMS) installed on the Tsing Ma Bridge in Hong Kong, has over 800 sensors which are currently generating 140 Mbytes-per-hour sensor data (Ko 2003). An even higher data rate could be produced with the use of high-resolution or high dynamic range sensors such as 24-bit sensors. This is especially true in the context of wireless data transmission and post hazardous events like strong earthquakes. A notable method is to only use those significant monitoring data that exceed a pre-specified performance threshold (Frangopol *et al* 2008; Strauss *et al* 2008). The prognosis will then be based on these extreme data only. By doing so, the amount of sensor data transmitted and consequently prognosis computation can be considerably reduced.

Many structural deterioration phenomena such as corrosion or fatigue-induced cracking are usually slowly evolving processes that take quite some time to develop. Therefore, periodical or on-demand monitoring can be carried out for such structural

limit states under normal operating conditions. Periodical monitoring at proper time interval could reduce the risk of unexpected failure while keeping the costs of data acquisition, transmission, storage and processing down.

On-demand monitoring is triggered whenever severe loading events such as overload or earthquake happen. Even for periodical monitoring, performing prognosis such as computing RULs using full sensor data set can be a daunting task due to the heavy demand on computational resources. Since unexpected failure might lead to catastrophic consequence, it is critical to know the small quantiles of the estimated RULs. Considering the fact that decision makers are often more interested in the small quantile or extreme values of the estimated RULs, it is not necessary to obtain the full probabilistic distribution of the RULs as a random variable. Therefore, estimation of the tail parts or extreme values of the RUL distributions based on a selected and thus reduced sensor data set would be of interest to SHM applications.

Continuous monitoring generates scattered data set due to uncertainties associated with environment conditions and instrumentation measurement error. To use the full sensor data set for RUL calculation could be very time consuming. The extreme value theory (EVT) is employed to reduce computation demand without losing much accuracy. EVT makes statistical inference about the upper tail of a random variable without the need of knowing its true distribution. EVT is employed to allow only a small percentage of total available sensor data to be actually used for estimating the tail quantile of the RUL. Estimators from EVT are often used to predict high quantile values for the distribution of prognosis results. A variety of estimators have been developed for EVT, such as the Hill estimator (Hill 1975), PWM estimator (Hosking

and Wallis 1987), and moment estimator (Dekkers *et al* 1989), etc. Moment estimator is selected here for its ability to discern a light tail distribution more efficiently than the Hill estimator (Resnick 1997). In many applications such as fatigue life prognosis or corrosion prognosis, the distribution of the RULs is usually bounded and not heavily tailed.

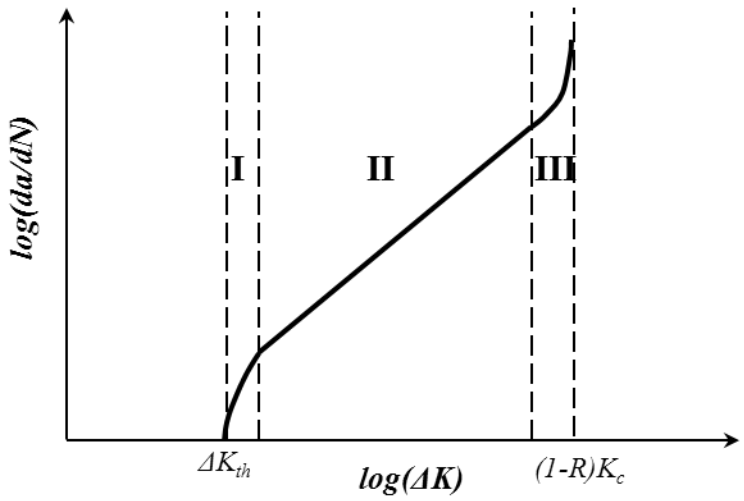

Figure 2.1. Schematic of typical fatigue-crack-growth behavior

Chapter 3: Fatigue Deterioration Models for Welded Tubular Structure

3.1 Introduction

Welded tubular joints are commonly used structural joint form in traffic signal support. There have been many reports of the fatigue cracking in the vicinity of the welded connections (Dexter and Ricker 2002). The fatigue behavior of this type of welded tubular joints is the study object of this chapter. For fatigue crack development, usually three stages can be distinguished, as shown in Figure 3.1. Stage I is the initiation stage. At this stage, the crack propagation is very slow and difficult to predict. Its propagation rate depends on the microstructure of the material. Stage II is the rapid propagation stage. Paris Law governs the crack propagation rate and linear relation exists between the logarithm of crack growth rate and stress intensity factor (SIF) range in this stage. Stage III is the final stage when the crack growth becomes unstable as maximum stress intensity factor (K_{max}) approaches fracture toughness (K_c). Considering the different features of crack growth associated with these three stages, different deterioration models may be proposed for each stage.

This chapter presents two distinct types of fatigue growth models for welded tubular joints: the linear elastic fracture mechanics (LEFM) model and the empirical failure model. Both models take crack size data as the input. The LEFM model has been used for the modeling of crack growth at stage II while the empirical failure model is intended for the modeling of crack growth at stage III. As for stage I, since the crack size is very small and its growth rate is hard to determine, no discussion of prognosis

in this early stage of fatigue growth will be made here.

In Chapter 3.2, the LEFM model is introduced. It is modified from the Paris Law to adapt to the specific application in welded tubular joints. Equations to calculate factors (correction factors and magnification factors) in the LEFM model are introduced to consider the stress concentration at the hot-spot of tubular joints. Size effects of the tubular joints (e.g. tube diameter, tube wall thickness) are taken into account by the LEFM model. Certain parameters in the LEFM model are treated as stochastic parameters to incorporate the uncertainty inherent in the fatigue deterioration process. Sensitivity study of the stochastic parameters is conducted. The LEFM model governs the second stage of fatigue crack growth. However, it is not applicable to the third stage of fatigue crack growth. In order to model the crack growth in stage III, the empirical failure model is introduced in Chapter 3.3. It is derived from the material failure equation (Voight 1989). Parameters of the empirical failure model are discussed. Examples are presented to illustrate its use for real crack growth data modeling.

3.2 LEFM model

3.2.1 Model description

3.2.1.1 Model assumptions

A schematic plot of the tubular joint studied is given as Figure 3.2. Crack usually happens along the weld toe due to the high stress level caused by stress concentration. A general assumption made in this study is that initial defects in the welded tubular joints are small, semi-elliptical surface cracks along the weld toe. Its major radius is denoted as c and minor radius is denoted as a. The ratio between these two radiuses

(*a/c*) is called aspect ratio. The relation between *a* and *c* for the semi-ellipse suggested by Vosikovsky *et al* (1985) for welded T-joints is adopted in this study and listed in Eqn. (3.1).

$$a/c = \begin{cases} x_1 \cdot (a/T)^2 + x_2 \cdot (a/T) + x_3 & \text{if a/T} < 0.25 \\ 0.2 & \text{if a/T} \geq 0.25 \end{cases} \tag{3.1}$$

In which,

$$x_1 = \frac{(a/c)_0 - 0.2}{(a_0/T)^2 - 0.5 \cdot (a_0/T) + 0.0625},$$

$$x_2 = -0.5 \cdot x_1,$$

$$x_3 = (a/c)_0 - x_1 \cdot (a_0/T)^2 - x_2 \cdot (a_0/T)$$

In Eqn. (3.1), *T* denotes the thickness of the plate where the crack initiates. Figure 3.4 gives a schematic plot of how the crack locates at the welded *T*-butt joint. Eqn. (3.1) shows that aspect ratio is related to the initial crack length a_0, initial aspect ratio $(a/c)_0$ and the plate thickness *T*. An example of aspect ratio evolvement is given as Figure 3.3 with a_0=0.2 mm and $(a/c)_0$ =0.5. Also, the wall thickness *T* is assumed to be 6.4 mm. In Figure 3.3, the aspect ratio is at its maximum value at the beginning and then monotonically decreases at the early stage of the crack propagation. It enters a plateau when the crack depth penetrates 1/4 of the tube wall thickness and becomes constant.

3.2.1.2 General model

According to Walbridge (2005), the fatigue model based on the Paris-Erdogan Law (Paris *et al* 1961) is modified as Eqn. (3.2) for tubular joint.

$$\frac{da}{dN} = C \cdot (\Delta K_{eff}^m - \Delta K_{th}^m) \tag{3.2}$$

In Eqn. (3.2), ΔK_{th} is the threshold stress intensity factor range. ΔK_{eff} is the range of

effective stress intensity factor (SIF) expressed as Eqn. (3.3),

$$\Delta K_{eff} = \max(K_{app,\max} - K_{op},\ 0) - \max(K_{app,\min} - K_{op},\ 0) \tag{3.3}$$

In which, $K_{app,\max}$, $K_{app,\min}$ denotes the maximum and minimum applied SIF. K_{op} denotes the applied stress intensity level at which the crack tip would open upon loading.

To calculate $K_{app,\max}$ and $K_{app,\min}$, finite element analysis can be used. However, finite element analysis is very demanding in computing, especially for complex structures like welded tubular joints. For practical application of the prognosis method, approximation needs to be made when calculating effective SIF. The equation proposed by Bowness and Lee (1999) for welded tubular joints is used in this study as Eqn. (3.4),

$$K_{app} = [Mk_m \cdot Y_m \cdot (1 - \mathrm{DOB}) + Mk_b \cdot Y_b \cdot \mathrm{DOB}] \cdot \sigma_{hs,app} \cdot \sqrt{\pi a} \tag{3.4}$$

where Mk_m and Mk_b are the magnification factors for the membrane and bending stress cases. These two factors are used to quantify the stress intensity as a result of the presence of the weld and attachment. Y_m and Y_b are correction factors for the membrane and bending stress cases given the crack as surface semi-elliptical crack. $\sigma_{hs,app}$ is the applied hot-spot stress at the location of interest, usually at the weld toe. Extrapolation method is used to acquire this number from measured strain data. DOB is the degree of bending.

In this study, the crack closure effect and the threshold for the SIF range are not considered, thus K_{op} and ΔK_{th} are set to be zero. Eqn. (3.3) is simplified into Eqn. (3.5):

$$\Delta K_{eff} = K_{app,\max} - K_{app,\min} \tag{3.5}$$

Consequently Eqn. (3.2) can be transformed into Eqn. (3.6):

$$\frac{da}{dN} = C \cdot [(Mk_m \cdot Y_m \cdot (1 - \mathrm{DOB}) + Mk_b \cdot Y_b \cdot \mathrm{DOB}) \cdot (\sigma_{hs,app,\max} - \sigma_{hs,app,\min}) \cdot \sqrt{\pi a}]^m \tag{3.6}$$

3.2.1.3 Factors and parameters

Magnification factors: Mk_m and Mk_b

Equations to calculate Mk_m and Mk_b were proposed by Bowness and Lee (1999) using parametric study based on finite element analysis. The original equations are derived based on the T-butt joint as shown in Figure 3.4. Equations are derived from the database obtained from finite element analysis. These equations are approximately used for tubular joints in practice (Bowness and Lee 1999; Walbridge 2005). One thing to note is that the equations for *Mk* are only valid for cracks with a depth less than ninety percent of the tube wall thickness. Equations for magnification factor at the deepest point of as-welded tubular joints are provided in Appendix A.

Correction factors: Y_m and Y_b

Equations to compute Y_m and Y_b were originally proposed by Raju and Newman (1979) based on the SIF acquired from a three-dimensional, finite element analysis of semi-elliptical cracks in finite elastic plates. Figure 3.5 shows a schematic plot of the semi-elliptical crack in the finite plate concerned. Equations for the correction factors are provided in Appendix B.

DOB

Degree of bending is defined as Eqn. (3.7):

$$DOB = \frac{\sigma_b}{\sigma_b + \sigma_m} \tag{3.7}$$

In Eqn. (3.7), σ_b is the bending stress and σ_m is the membrane stress.

Hot-spot stress: $\sigma_{hs,app}$

Extrapolation method is applied to acquire the hot-spot stress range. In order to implement extrapolation method, several strain gauges needs to be put next to the welding toe in parallel. The extrapolation region for the strain gauges is provided in Table 3.1 (Romeijn 1994; Zhao *et al* 2001). *T* denotes the thickness of the tube wall. R_t denotes the external radius of the tube. Linear extrapolation method is adopted here for calculation of the hot-spot stress range. Two strain gauges are spaced from $L_{r,\min}$ to $L_{r,\max}$. A sketch of the extrapolation region is given as Figure 3.6.

3.2.1.4 Fatigue life

In order to estimate the fatigue life, critical crack depth a_c needs to be defined. For the critical crack depth a_c, full wall thickness or half wall thickness have been used (Zhao and Haldar 1996; Cremona 1996). Since a majority of the fatigue life will be spent at the crack initiation stage, small variation in critical crack depth definition would only have minor effect on the estimated total fatigue life (Moan and Song 2000). Thus the critical crack depth for the welded tubular joints is defined as 0.9 of the tube wall thickness in this study which is consistent with the conditions for equations of factors *Mk* and *Y*.

After defining a_c, fatigue life *N* can be calculated by integrating Eqn. (3.2) from a_0 to a_c. The expression of *N* is given as Eqn. (3.8). N_0 denotes the initial load cycle.

$$N_c = \int_{a_0}^{a_c} \frac{da}{C \cdot [(Mk_m \cdot Y_m \cdot (1-\mathrm{DOB}) + Mk_b \cdot Y_b \cdot \mathrm{DOB}) \cdot (\sigma_{hs,app,\max} - \sigma_{hs,app,\min}) \cdot \sqrt{\pi a}]^m} + N_0 \tag{3.8}$$

3.2.2 Stochastic parameters

Fatigue behavior bears a lot of uncertainty. The values of the parameters in the LEFM

model thus differ a lot from case to case. Type of structures, material properties and environment etc. would all have impact on the parameters. A lot of fatigue tests on different type of structures with different material properties and environment conditions have been conducted to obtain a statistic data for those model parameters. In order to consider those uncertainties, it is necessary to make the general model stochastic. Here, selected parameters in the model are considered as stochastic parameters to represent the uncertainties in the model.

Common to the LEFM fatigue model, a_0 and C are considered as the two stochastic parameters. Examples of the recommended distributions for different cases of a_0 and C are listed in Table 3.2 and Table 3.3 (Chung 2005). As for the application to welded tubular joint fatigue, Walbridge (2005) suggested that a_0 follows a lognormal distribution with a mean value of 0.2 mm and standard deviation of 0.045; C follows a lognormal distribution with a mean value of 2.33×10^{-13} and standard deviation of 1.38×10^{-13}. Also, for welded tubular joints, aspect ratio is an important parameter to its fatigue. Yet the initial aspect ratio is very difficult to determine. Therefore, it is also assumed to be a stochastic parameter which follows a lognormal distribution with a mean value of 0.5 and a standard deviation of 0.16. In sum, three parameters a_0, C, $(a/c)_0$ are selected as stochastic parameters in this study. Due to the lack of data specifically for the tubular joints in signal support structure, recommended values for those three stochastic parameters (a_0, C, $(a/c)_0$) from Walbridge (2007) for the application of tubular joints in bridges are adopted here as an example. The values are summarized in Table 3.4. In later chapters, the fatigue test results based on full-scale lab tests of tubular joints in signal support structure conducted at University of

Maryland, College Park will be used to derive the values for those stochastic parameters. All other parameters are considered deterministic.

Figures 3.7 to 3.9 show examples of the crack growth curves. All values for deterministic parameters in Eqn. (3.6) are listed in Table 3.5. All values for stochastic parameters are given in Table 3.4. Two parameters out of the three stochastic parameters are made deterministic by fixing at their μ values while the third parameter is set to be varying from its μ value to μ±2σ. The correspondent curves of mean, 2.3% quantile and 97.7% quantile are plotted for each case. It can be seen that in Figure 3.9, the three curves have the largest dispersion while in Figure 3.7, they have the smallest dispersion. This shows that *C* has the most significant impact on their crack growth curves while $(a/c)_0$ has the smallest effect among all three stochastic parameters.

Because Paris Law is only valid for fatigue stage II, the proposed LEFM model for welded tubular joint structure fatigue is naturally only applicable in fatigue stage II.

3.3 Empirical failure model

3.3.1 Introduction of basic model

Many material failure phenomena are preceded by clear accelerating rates of strain, displacement and seismicity (Cornelius and Scott 1993). Voight (1989) proposed a relation between the acceleration in a geophysical precursor Ω (such as strain or number of earthquakes) and its rate for conditions of constant stress and temperatures, shown below as Eqn. (3.9) (Bell *et al* 2011).

$$\frac{d^2\Omega}{dt^2} = G\left(\frac{d\Omega}{dt}\right)^{\alpha} \tag{3.9}$$

Quantities that can be represented by Ω include strains for deforming alloys, metals, polymers, concrete, soil, rock, or ice. Fields of potential application of Eqn. (3.9) include materials science, various branches of engineering, and the earth sciences. Eqn. (3.9) may also apply (at least approximately) to predominantly rate-independent applications, such as some cases of fatigue (rate-independent repeated loading) (Voight 1989).

According to Main et al (1991), rates of crack growth increase exponentially with crack length in many cases (Kilburn and Voight 1998). Eqn. (3.9) can be implemented for such case of material failure (e.g. volcano eruption). As for the case of fatigue cracking, at its final stage with the presence of large "unstable" crack, the crack growth rate would increase sharply. According to the Forman Equation shown in Eqn. (3.10) (Forman *et al* 1967), clear acceleration of crack growth rate occurs at the final stage when ΔK approaches $(1\text{-}R)\cdot K_c$. K_c denotes the fracture toughness of the steel specimen. R is the stress ratio (S_{min}/S_{max}).

$$\log(da/dN) = \log(C) + m \cdot \log(\Delta K) - \log[(1-R) \cdot K_c - \Delta K] \tag{3.10}$$

Thus, potentially Eqn. (3.9) can be applied to estimate the fatigue failure time, for which the crack length can be taken as the precursor signal.

3.3.2 Derivation of explicit model

Eqn. (3.9) can be transformed into Eqn. (3.11) to represent the final stage of cracking before catastrophic failure (Kilburn and Voight 1998).

$$\left(\frac{d\Omega}{dt}\right)^{-1} = \left(\frac{d\Omega}{dt}\right)_0^{-1} - \gamma(t - t_0) \tag{3.11}$$

In Eqn. (3.11), Ω denotes the damage index. γ is an rate related coefficient. t_0 is the

initiation time. t_f is the total life from t_0. By letting t_0 = 0, Eqn. (3.11) can be transformed into Eqn. (3.12)

$$\Omega(t) = -\gamma \ln(t_f - t) + \gamma \ln t_f \tag{3.12}$$

Based on many curve fitting test of fatigue test data, Eqn. (3.12) is further modified by making the second term at right hand side of the equation an independent parameter as shown in Eqn. (3.13). Eqn. (3.13) is chosen as the empirical failure model for fatigue failure.

$$\Omega(t) = -\gamma_1 \ln(t_f - t) + \gamma_2 \tag{3.13}$$

In this study, the damage index, $\Omega(t)$ is the fatigue crack length although other parameters such as hot-spot strain potentially could also be used as the damage index . t_f is the fatigue failure time (counted from t_0). γ_1, γ_2 and t_f are parameters which depend on the material properties, geometrical properties and external loading conditions. One advantage of applying the empirical failure model for prognosis is that the failure time t_f is explicitly treated as a parameter in the equation and its value can be directly obtained by updating its distribution using sensor data. In this way, no additional failure criterion needs to be defined (e.g., for the LEFM based prognosis, a critical fatigue size has to be defined first). In this dissertation study, the potential use of Eqn. (3.13) for fatigue prognosis is examined using real fatigue test data.

In the empirical failure model described by Eqn. (3.13), γ_1 determines the growth rate of the damage index Ω. γ_2 represents the intersection with y-axis. Figures 3.10 to 3.12 show the effect of the three parameters on the curve. The initial values are γ_1 = -13.312, γ_2 = 173.64, t_f = 5.34×10^5. For each figure, the value of one of the three parameters is varied while the other two parameters are kept constant.

A case study is presented next to show the feasibility of using the empirical failure model for fatigue prognosis.

3.3.3 Case study

In order to examine how well the empirical failure model would fit real fatigue crack growth data, fatigue crack data from the experiments done by Virkler *et al* (1978) is used for curve fitting. In their test (Virkler *et al* 1978), 68 replicate fatigue tests with the same loading on specimens with the same design were implemented on 2024-T3 aluminium alloy under constant load amplitudes. Crack length trajectories were recorded for each test. All tests started with an initial crack length of 9.0 mm and tests were terminated at the crack length of 49.80 mm. Mean values of the crack length data at specific load cycles are calculated from these test data. This crack growth data set has also been used in statistical analysis of fatigue crack growth and prognosis by other researchers (Perrin *et al* 2007; Guan *et al* 2012). A set of the mean crack length data is used here. The crack length data is fitted with the empirical failure model. Figure 3.13 shows the fitted curve with the fitted model expressed as: $\Omega(t)$=-13.312*ln($5.34\text{x}10^5$-t)+173.64. In Figure 3.13, the residuals of the fitted curve are also plotted. They are all quite small comparing with the measurements indicating that the model fits the data well. Moreover, the coefficient of determination (R^2) is selected as the index to evaluate how well the model describes the behaviour of the data. More details about R^2 application can be found in Steel and Torrie 1960. The closer R^2 value is to 1, the better the model describe the data. In this case, R^2 is calculated to be 0.9989. It suggests that the model fits the crack growth data very well.

3.4 Conclusions

The LEFM model can be used to describe the fatigue growth of welded tubular joints at fatigue stage II. Stochastic parameters are introduced to incorporate the uncertainty in the fatigue crack propagation. Sensitivity studies show that C has greatest impact on the crack growth rate in the LEFM model. One advantage of the LEFM model is that it represents the effect of structural/material properties (C, m) and external loading ($\Delta\sigma$) using three parameters and have been validated by many fatigue data. However, one fundamental assumption for the LEFM model is that the crack shape is assumed to be semi-elliptical. Also, it is limited to the application on cracks with depth less than 0.9 of the tube wall thickness. When fatigue crack depth exceeds this limit, the LEFM model is no longer valid.

To complement the LEFM model for later stage crack propagation modelling, the empirical failure model is proposed. It can be used to model fatigue crack propagation till failure. One feature of the empirical failure model is that it includes the failure time t_f as an explicit parameter in the model (The failure time t_f is defined as the time when the specimen becomes unstable and is no longer able to carry load). In prognosis practice, t_f is directly obtained by model updating of the empirical failure model. A case study of real fatigue data is performed to demonstrate that the empirical failure model can fit real fatigue crack growth data. A detailed comparison of the LEFM model and empirical failure model is given in Table 3.6.

Table 3.1. Extrapolation region

CHS	$L_{r,min}$	$0.4T$
	$L_{r,max}$	$0.09R_t$

R_t: external radius of the tube

Table 3.2. Examples of a_0 distribution for different applications

Detail	Initial crack size a_0 (unit: mm)			Reference source
	D.T.	Mean	COV	
Tubular joint	Exponential	0.110	1	Kirkemo (1988)
Tubular joint	Lognormal	0.730	1.07	Shetty and Baker (1990)
Tubular joint	Lognormal	0.200	0.225	Walbridge (2005)
Cover plate	Lognormal	0.508	0.5	Yazdani and Albrecht (1987)
Gusset Plate	Lognormal	0.100	0.2	Righiniotis and Chryssanthopoulos (2003)
Fillet welded joint	Lognormal	0.124	0.34	Engesvik and Moan (1983)
Stiffener to Bottom Flange	Lognormal	0.600	0.1	Cremona (1996)

D.T. = Distribution type; COV = Coefficient of Variation

Table 3.3. Examples of C distribution for different applications

Material	Environment	C (mm/cycle)·(N/mm$^{-3/2}$)^m			Reference source
		D. T.	Mean	COV	
A36	Air	Lognormal	1.783×10^{-12}	0.221	Klingerman and Fisher (1973)
A514	Air	Lognormal	5.335×10^{-13}	0.088	Barsom and Novak (1977)
HSLA Steel	Air	Lognormal	1.54×10^{-12}	0.226	Yazdani and Albrecht (1989)
A36, A588	Air	Lognormal	1.97×10^{-12}	0.076	Barsom and Novak (1977)
A36, A588	Aqueous	Lognormal	5.58×10^{-12}	0.15	Yazdani and Albrecht (1989)

D.T. = Distribution type

Table 3.4. Stochastic parameter values of the LEFM based fatigue growth model

	C (mm/cycle)·(N/mm$^{-3/2}$)^m	Initial crack depth a_0 (mm)	Initial crack aspect ratio $(a/c)_0$
Mean	2.33×10^{-13}	0.2	0.5
Standard deviation	1.38×10^{-13}	0.045	0.16

Table 3.5. Deterministic parameter values used for steel welded tubular fatigue model

Tube wall thickness T (mm)	6.4	DOB (degree of bending)	1
Weld toe angle θ (°)	45	Hot-spot stress range $\Delta\sigma$ (MPa)	100
Weld footprint length L_w (mm)	6.4	m	3.0
Half plate width b (mm)	200		

Table 3.6. Comparison of the LEFM model and the empirical failure model

	LEFM model	Empirical failure model
Form	differential equation	explicit model
Input	crack length, stress range	crack length
Failure time estimation	additional failure criteria needed	t_f explicitly expressed in model as a parameter
Application	fatigue stage II only	Late stage of fatigue stage II & stage III

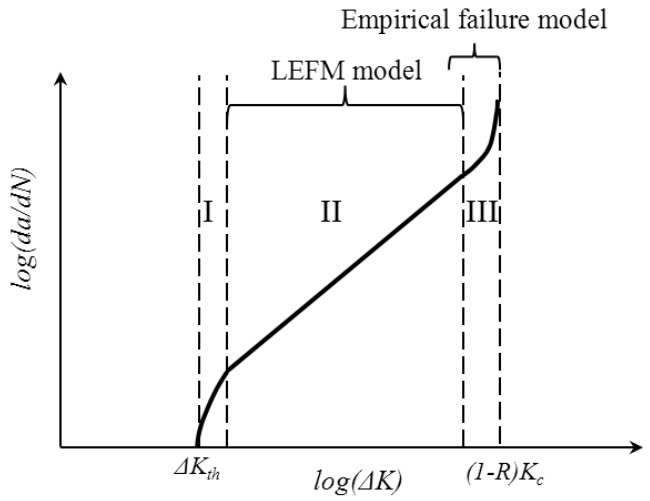

Figure 3.1. Fatigue crack propagation

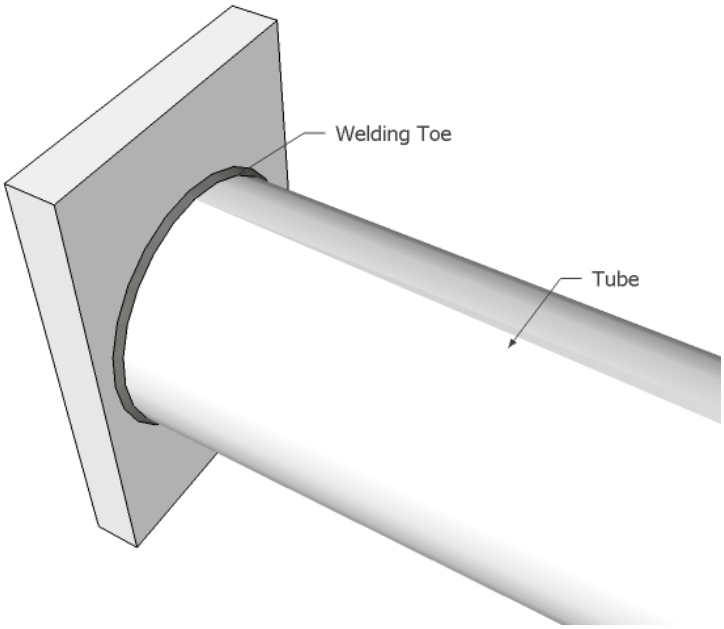

Figure 3.2. Example of tubular structure

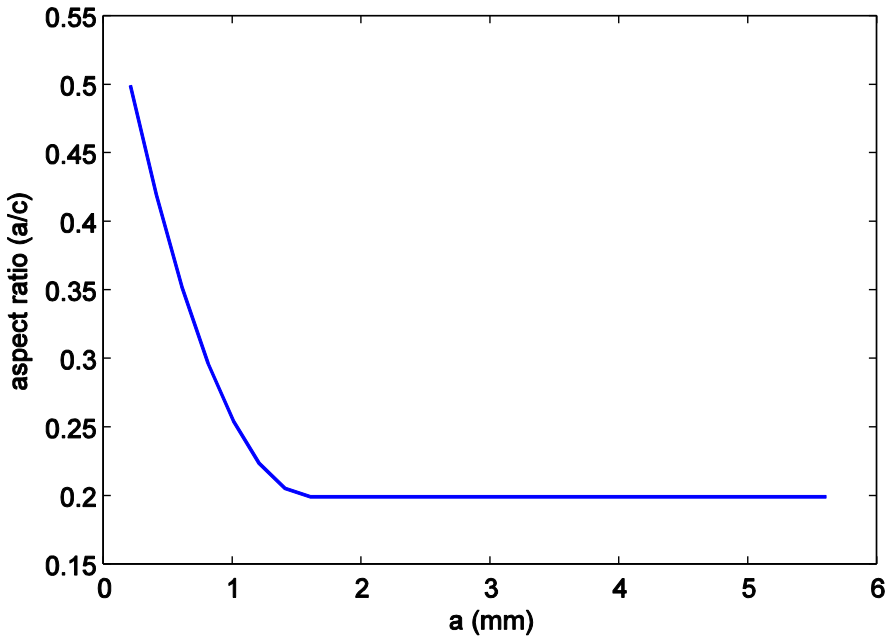

Figure 3.3. Fatigue crack aspect ratio curve with a_0=0.2 mm and $(a/c)_0$ =0.5; (T=6.4 mm)

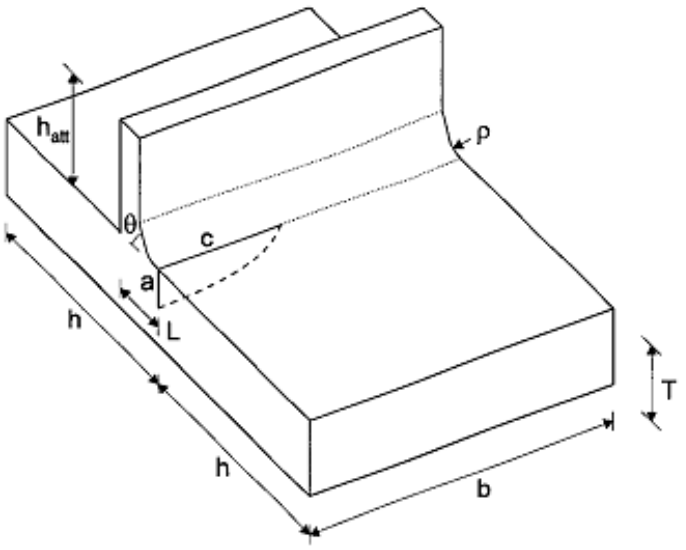

Figure 3.4. Nomenclature for T-butt joint (Bowness and Lee, 1999)

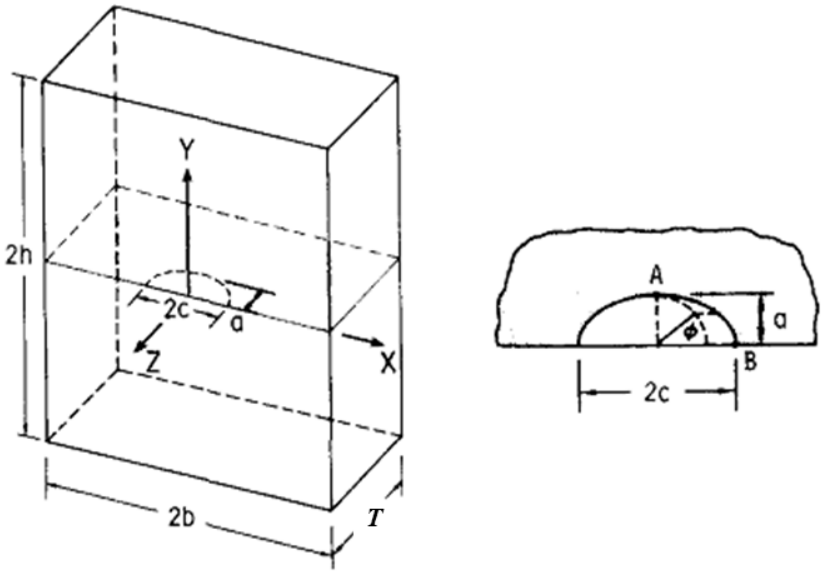

Figure 3.5. Semi-elliptical surface crack in a finite plate (Newman and Raju, 1981)

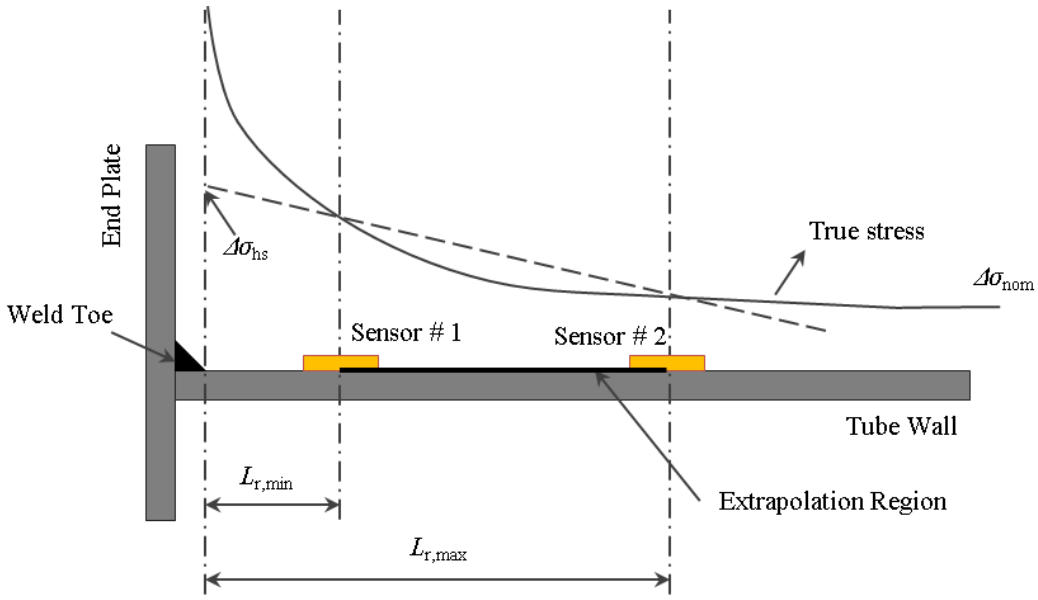

Figure 3.6. Hot-spot stress extrapolation region

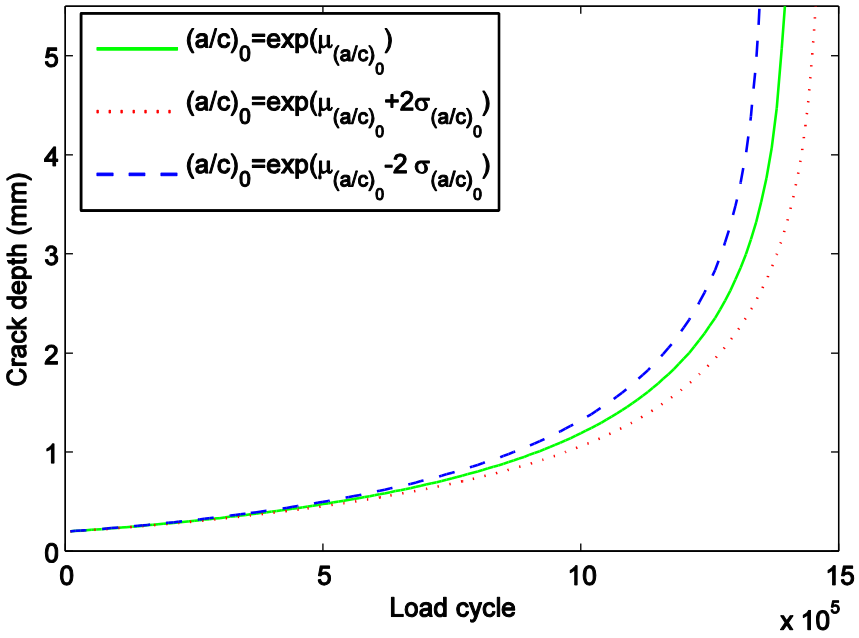

Figure 3.7. LEFM model with varying values of $(a/c)_0$

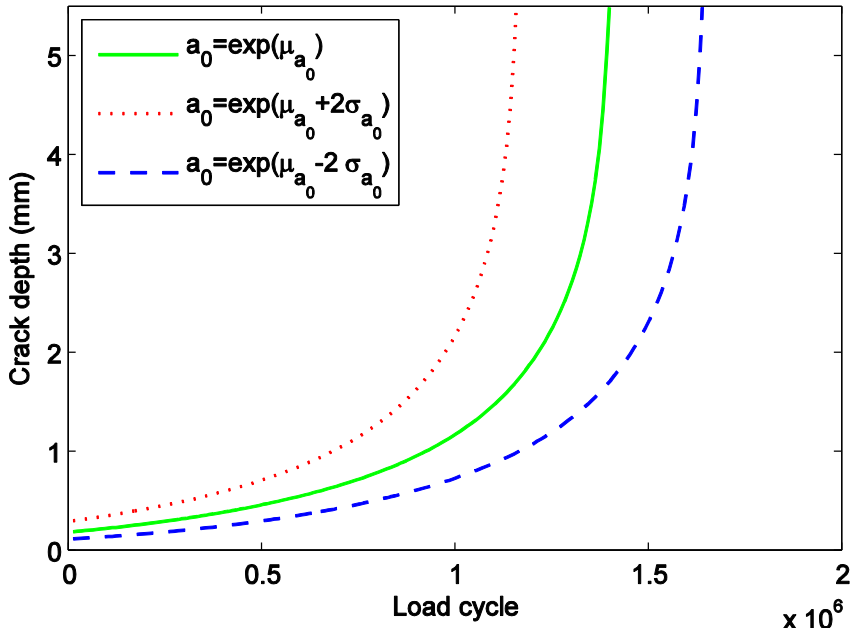

Figure 3.8. LEFM model with varying values of a_0

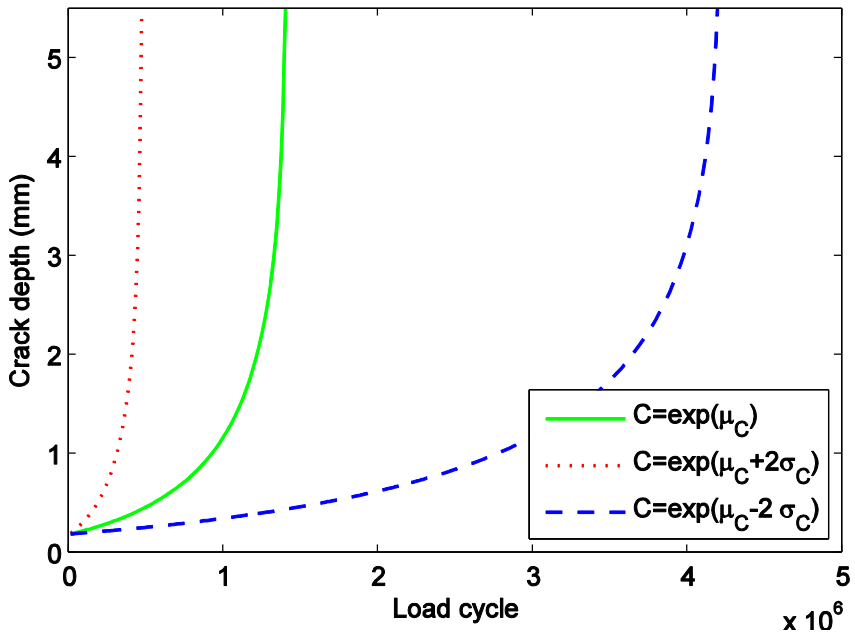

Figure 3.9. LEFM model with varying values of C

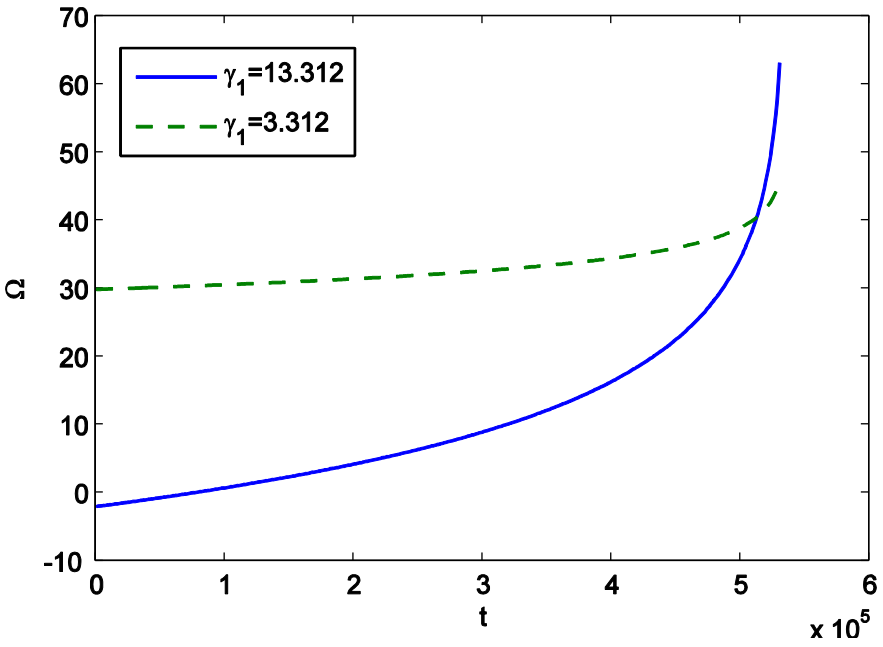

Figure 3.10. Empirical failure model with varying values of γ_1

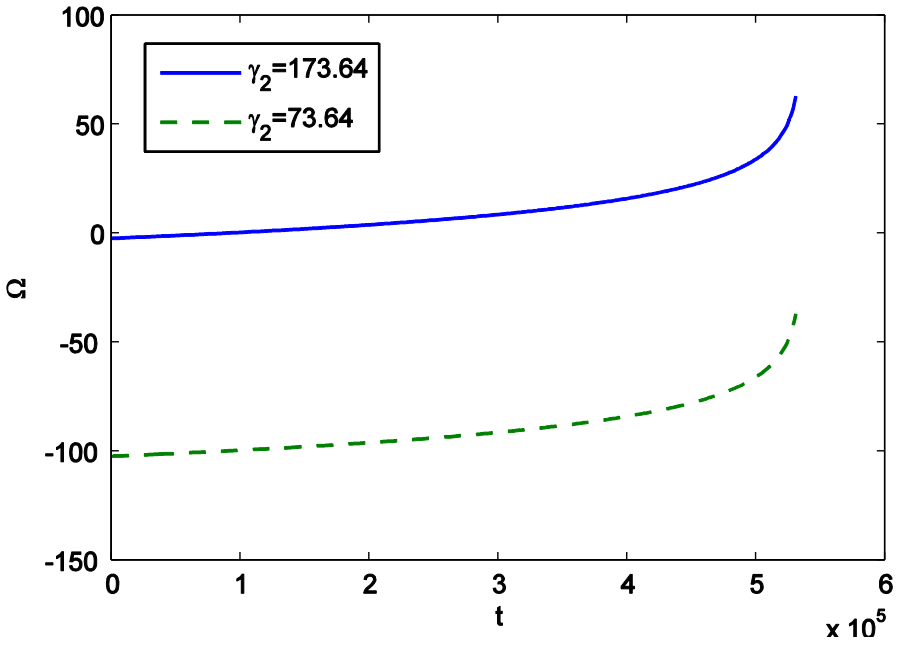

Figure 3.11. Empirical failure model with varying values of γ_2

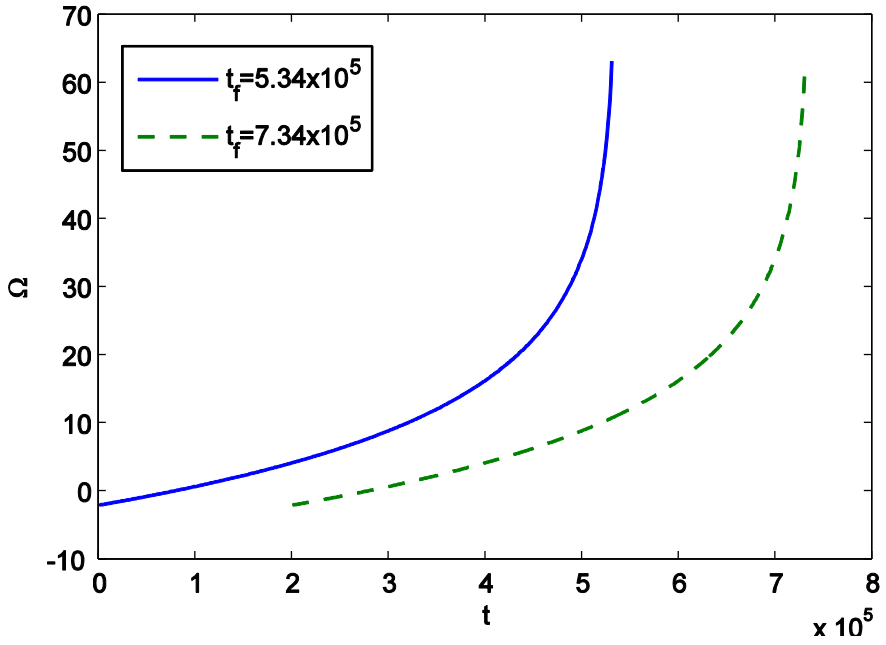

Figure 3.12. Empirical failure model with varying values of t_f

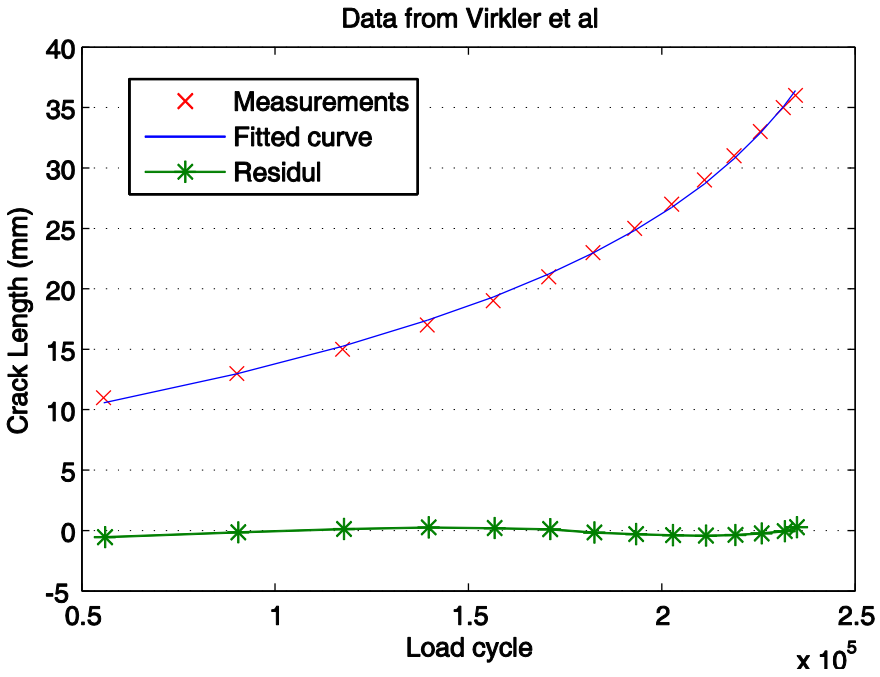

Figure 3.13. Curve fitting of data from the fatigue experiment reported by Virkler et al (1978)

Chapter 4: Fatigue Test of Welded Tubular Joints in Signal Support Structure

4.1 Introduction

Fatigue behavior of weleded tubular structure has been extensively studied in the past decades. However, most of the research have been focused on offshore structure or bridges. In comparison with tubular joints in offshore structures and bridges, welded tubular joints commonly found in signal support structures and cranes exhibit notable differences such as member dimensions (both absolute and relative), the loads affecting the joint, and joint fabrication procedures. For the research related to tubular joints in signal support structure, most of them are based on stress-life approach. During the lab test, only the fatigue life is recorded with little information about the crack propagation.

In order to obtain experiment data about the fatigue crack propagation for tubular joints on signal support structure and gain some experience on the fatigue behavior of such structures, full-scale lab fatigue test on typical tubular joints from signal support structure is carried out. Crack propagation data are recorded. Details of the fatigue test are introduced in this chapter. Description of the test program is firstly provided including the introduction of test specimen, test setup, loading plan and instrumentation. Next, test result is provided followed by discussion. Fatigue tests were carried out on six welded tubular joint specimens. The full-scale round signal mast arms with welded transverse plate were fabricated based on real signal support design for the state of Maryland. Static tests were first carried out to investigate the

hot-spot stress distribution at the welded toe of the joint. Then, cyclic fatigue loading was implemented. During the fatigue test, fatigue crack size was monitored with a digital microscope. Tubular members were instrumented with uni-axial metal foil strain gauges. Data of crack location and size, applied load range and hot-spot/nominal strain were recorded. Those data were used for fatigue prognosis later.

4.2 Description of the test program

4.2.1 Test specimen

In the report by Kaczinski *et al* (1998), fatigue details of structural supports for traffic signal are listed. Among them, Detail 16 is a typical fatigue detail of welded tubular joints, which is a fillet-welded tube-to-transverse-plate connection (See Figure 4.1). This fatigue detail is selected for fatigue test because it is commonly used as column-to-base-plate or mast-arm-to-flange-plate socket connections in traffic signal supports. The detail is categorized as fatigue category E' (Kaczinski *et al* 1998).

Six identical full-scale specimens were fabricated in accordance with the mast-arm-to-flange plate connection design for signal support structures in Maryland. The full-scale test specimens were fabricated by Millerbernd Manufacturing Co. These specimens are labeled as WTJ1 to WTJ6 for later reference. Dimensions of these test specimens are shown in Figure 4.2. The specimen is comprised of two components - a tapered seam-welded steel tube made of ASTM A572 steel and a traverse plate made of ASTM A36 steel. The steel tube is inserted into the transverse plate and welded together using fillet weld, as shown in Figure 4.2. The transverse plate is a rectangular plate measuring 0.4572 m (18 inches) x 0.3048 m (12 inches) x 0.0508 m (2 inches). The tube's length is 1.524 m (5 feet). A taper rate of 0.0118 m/m (0.14 inches/foot)

for the diameter is applied, which leads to a variation of external diameter tapering from 0.254 m (10 in) to 0.236 m (9.3 in) at its open end. The thickness of the tube wall is 6.35 mm (1/4 inches).

4.2.2 Test setup and loading plan

Figure 4.3 shows a picture of the test setup. The transverse plate of the test specimen is anchored to the reaction frame with bolts. MTS servo-hydraulic loading system (dynamic 244.31 linear hydraulic actuator and FlexTest GT controller) was used to apply cyclic loading to the test specimen. Cyclic load with constant amplitude is applied vertically at the free end of the specimen with the servo-controlled hydraulic actuator. However, test of WTJ6 used a different loading scheme in order to apply a beach-marking method for fatigue growth marking which employs an alternating loading scheme with two different load ranges. According to Aghakouchak and Stiemer (2001), almost all signal support structures that have been tested in the field have natural frequencies in the range 0.5 Hz to 2 Hz. Therefore, the loading frequency in this test is set to be 1.5 Hz.

4.2.3 Instrumentation

Two types of data are acquired during the fatigue test: surface crack length (only for three specimens WTJ4 to WTJ6) and strains at specified locations (for all 6 specimens). For strain measurement, metal foil strain gauges (Vishay model EA-06-125AC-350 and EA-06-250BF-350) were used. Each test specimen has ten strain gauges, labeled as SG1 to SG10 for reference. The instrumentation plan for the strain gauges is shown in Figure 4.4. Nine out of the ten gauges are placed at the two sections of the specimen. Section A is located at the weld toe and Section B is 0.305

m (12 inches) away from the weld toe. SG1 and SG2 are placed at the top of the tube at 0° from the top ridge line of the tube to measure hot-spot stress. SG1 is the one closer to the weld toe. Extrapolation method is applied with the readings of those two strain gauges to calculate the hot-spot stress range (Zhao *et al* 2001). SG3, SG4 and SG5 are placed at the 22.5°, 45° and 180° position in Section A to monitor the hot-spot strain distribution along the perimeter of the weld toe. SG7 to SG10 are placed at 0°, 90°, 180°, 270° in Section B (see Figure 4.4) to measure the nominal strain. SG6 is to measure the hoop strain.

Figure 4.5 illustrates the strain instrumentation. Figure 4.5a shows the position of the strain gauges on the test specimen. The strain gauges are connected to the data acquisition system (Pacific Instruments 6000, strain gage card 6038) using cables. Figure 4.5b provides a close-up view of the hot-spot strain gauges. It is seen that SG1, SG3 and SG4 are next to the weld toe and perpendicular to circumferential weldment while SG6 is parallel to the weldment.

For crack monitoring and sizing, a digital microscope (model AM7013MZTS polarizing microscope) is used. In the test, a magnification factor of 50 is used to see the fatigue crack. Larger magnification is not possible because of blocked view by the 90 degree angle between the transverse plate and the tube at the weld toe, which makes it impossible to get the smaller view depth required for higher magnification factor. The detection and size measurement of fatigue cracks using the digital microscope depends on crack opening width under cyclic loading. Once the crack opening width is large enough to be identified in microscope image, the crack is detected. During the fatigue test, crack growth is periodically monitored using the

digital microscope. At the early stage of crack growth, crack length is measured every 10,000 cycles while at the final stage of the crack propagation; measurement is taken every 5,000 cycles. Figure 4.6 shows the microscope on the specimen tube.

4.3 Test result and discussion

Fatigue tests were terminated after crack propagation became unstable. Strain and load data was recorded in all specimens. For crack length data, specimens WTJ1 to WTJ2 were used for crack measurement technique training and adjustment purpose. Crack length propagation data was not kept. WTJ3 failed prematurely at 2.18×10^5 load cycle which was totally unexpected and thus no crack measurement was performed. In addition to the digital microscope for crack measurement, alternative methods such as dye penetrant, phased array ultrasonic sensor were also tested to examine techniques for early-stage crack propagation measurement, but did not work as well as the digital microscope on the steel tube specimens. It is found in this test that microscope can identify initiating crack earlier than dye penetrant or phased array ultrasonic technique.

4.3.1 Crack length measurement

Table 1 lists the total load cycle numbers and the final overall crack length at the test termination for all six specimens which show a large dispersion. It is noted that for WTJ1 and WTJ2, the test was terminated at a smaller overall crack length than the other four specimens because these two specimens are mainly tested for training and adjustment purpose. However, they both entered the final unstable crack propagation stage at the time of test termination. These data points of total load cycles falls

between the AASHTO fatigue category C and E although the AASHTO fatigue category designation for this detail is category E'. This result is also found to be in agreement with the test results reported by Archer and Gurney *et al* (1970) on similar test specimens.

An image of WTJ1 specimen showing the fatigue crack highlighted with dye penetrant is presented in Figure 4.7. The crack can be clearly seen as a dark red line along the weld toe and the crack is approximately 6 cm in length when this picture was taken. Figure 4.8 gives two pictures of fatigue cracks taken by the digital microscope on WTJ6. Figure 4.8a shows the crack with a length of 2.4 cm which was imaged at 1.22×10^5 load cycle. Figure 4.8b shows the crack imaged at 3.55×10^5 load cycle (near the end of its loading) when the crack length is about 30 cm.

Figures 4.9 to 4.11 show the crack length growth pattern recorded for specimens WTJ4 to WTJ6. For all three specimens, the crack almost always initiated near the top ridge of the specimen where the maximum stress range occurs at the weld toe (this is also the location where steel tube seam weld meets the circumferential fillet weld, supposedly leading to a higher chance for weld defect) and then gradually propagate in both directions along the weld toe. For all three specimens, the crack propagates faster on the south side of the tube. This might be due to the imperfect alignment between the actuator and the specimen. The actuator position is slightly away from the center of the tube towards the south side. Therefore, the strain level on the south side of the tube would be slightly higher than that of the north side. It leads to the faster crack propagation on the south side.

Using the digital microscope, crack can be identified as early as when its length

reaches 10 mm. For example, for WTJ5, the crack was first identified at 13 mm. At the final stage of the fatigue test, the fatigue crack penetrates the full thickness of the steel tube and crack opening width can reach about 2 mm under the peak load. Crack growth curves for specimens WTJ4 to WTJ6 are plotted in Figure 4.12. For WTJ6, Miner's rule is applied to correct the recorded data from beach-marking loading into that of constant amplitude loading with bending moment range at weld toe section ΔM = 39.55 MPa-m as given in Table 1. Detailed descriptions of the crack measurement for each specimen are provided below,

WTJ1

The crack was first seen with naked eye at load cycle number N = 560,687 cycles. Dye penetrant was immediately applied to highlight the crack. The crack length was approximately 60 mm at that time point. For the initial 565,068 load cycle, a steel extension tube with the length of 0.2286 m (9 inch) and diameter of 0.2032 m (8 inches) was installed at the free end of the test specimen as a loading fixture connecting the actuator and the specimen. However, friction between the steel extension tube and the test specimen caused strong noise which overwhelmed the acoustic emission signal in the piezoelectric paint AE sensor mounted on the specimen. Therefore, the test specimen was repositioned by shifting a distance of 0.305 m (1 foot) towards the actuator and the actuator is directly on top of the test specimen after removing the extension tube. The fatigue test was terminated at load cycle number N = 619,000 when the overall crack length reached 251 mm.

WTJ2

Crack was not visible to naked eye until load cycle number N = 941,700. Since the

load cycle was already 1.5 times that of the previous specimen, load range was increased from 22.06 kN to 22.58 kN at load cycle number N = 941,700 cycles to accelerate the test. Digital microscope, dye penetrant and phased array were applied to measure the crack length. Conclusion is drawn that phased array and dye penetrant techniques are not working well to perform crack length measurement when crack length and opening is still very small. Digital microscope gives the most reliable result among the three methods in terms of crack length measurement. Multiple cracks were identified at different locations along the fillet weld toe. The test was terminated at load cycle number $N = 12.46 \times 10^5$ cycles. At that time point, the multiple cracks merged into one long crack with an overall length of 181 mm.

WTJ3

WTJ3 was cyclically loaded to 120,462 loading cycles and no crack was identified. Based on the experience gained from specimens WTJ1 and WTJ2, it was believed that no crack should happen before load cycle number N = 200,000 cycles. Therefore, overnight fatigue loading was applied without checking the crack. However, in the next morning when N = 217,800 cycles, a crack with the length of over 30 cm had already occurred along the weld toe in the specimen. The test was then terminated and thus no crack length data was measured.

WTJ4

The crack was firstly seen at load cycle number $N = 3.87 \times 10^5$ with a length of 10 mm using the digital microscope. Crack length was then periodically measured. At N = 582,281 cycles, the test was terminated with a total crack length of 342 mm.

WTJ5

The crack was first identified at N = 191,251 with a crack length of 13 mm. Test was terminated at N = 390,098 with a total crack length of 337 mm.

WTJ6

Crack was first identified at N = 122,620 cycles with a crack length of 24 mm. The crack was not symmetric about the seam weld of the tube. The crack length grew to 35.8 mm at load cycle number N = 355,171 cycles. Beach marking loading of 10,000 load cycle with a load range from 14.63 kN to 27.78 kN was applied five times at N = 180,000 to 190,000; N = 220,000 to 230,000; N = 260,000 to 270,000; N = 300,000 to 310,000 and N = 340,000 to 350,000 to generate beach marks on fracture surface.

Figures 4.9 to 4.11 give the crack initiation and propagation plots for WTJ4 to WTJ6.

4.3.2 Load and strain

Loading parameters for fatigue test of WTJ4 to WTJ6 are listed in Table 4.1. The loading history for WTJ4 is shown in Figure 4.13. Its amplitude varies from 0.91 kN to 27.43 kN with the load range of 26.52 kN. For WTJ4, displacement control mode was used to operate the servo-hydraulic actuator. At the final stage, the crack became very large. The stiffness of the test specimen dropped. The applied load range dropped consequently with the constant displacement range of loading. As seen in Figure 4.13, the load range started to drop gradually at around 5.0×10^6 load cycle and it eventually went below 15 kN at the test termination. For WTJ5, mixed displacement control mode and force control mode were used to keep the load range constant. The load range is 26.48 kN as shown in Figure 4.14. Figure 4.15 shows the load history of WTJ6. Before $N = 1.8 \times 10^5$, the load range was kept constant. Starting from $N = 1.8 \times 10^5$, alternating loading scheme with two different load ranges were

executed every forty thousand load cycle, among which first ten thousand cycles have a load range from 14.63 kN to 27.78 kN and the following thirty thousand cycles have a load range of 1.39 kN to 27.78 kN. As mentioned before, this alternating loading scheme was implemented to generate beach-marks in fracture surface.

The strain distributions under static loading for specimens WTJ4 to WTJ6 at the two sections along the tube are plotted in Figures 4.16 to 4.18. It is observed that for all three specimens the SG1 strain at the top of the steel tube always had the maximum value. Additionally, the strain measurements close to the weld toe at Section A are much larger than those at Section B. This signifies the existence of large stress concentration close to the weld toe.

For all three specimens, the strain levels at Section B are close to each other except for the reading of SG7 of WTJ6 which is smaller than that of WTJ4 and WTJ5. This might be caused by the seam weld on the top of the tube. Because of the existence of the seam weld, SG7 has to be placed away from the center line instead of putting exactly on top of the weld (see Figure 4.5a). The different width of the seam weld for each specimen caused the location of SG7 on the tube section to be slightly different from specimen to specimen. For WTJ6, the width of the seam weld is a little wider than WTJ4 and WTJ5, makes the placement of SG7 further away from the center line which leads to reduced strain readings.

As for Section A, strain readings from specimen WTJ4 and WTJ6 have similar strain reading while the readings from WTJ5 are smaller for SG1, SG3 and SG4. This difference signifies different stress concentration levels in these three specimens. Strain histories of SG1, SG2 and SG7 in specimens WTJ4 to WTJ6 are shown in

Figures 4.19 to 4.21 respectively. For WTJ4, Figure 4.19 shows that the strain readings from all three gauges remained relatively unchanged at the initial stage but dropped rapidly at final stage. One thing worth noting here is that for SG1 and SG2, their reading started dropping as early as around $N = 4.4\text{x}10^5$ load cycle due to local strain relaxation caused by the propagating crack. On the contrary, the reading of SG7 dropped later at $N = 5.0\text{x}10^6$ due to reduced load range. This feature of local strain relaxation caused by fatigue crack can be used for fatigue failure warning or even fatigue life prognosis. For WTJ5, it is seen in Figure 4.20 that the readings of SG7 at Section B kept nearly constant even at the final stage when the crack reached enormously large size. However, for SG1 and SG2, since they are located very close to the crack, the strain at their locations dropped substantially due to cracking. The strain history of WTJ6 in Figure 4.21 also shows decreasing strain at the final stage of fatigue loading. Also, Figure 4.21 shows the impact of beach-marking on strain readings.

Using the strain recordings from SG1 and SG2, the hot-spot stress range can be derived by adopting a linear extrapolation method. The distances of SG1 and SG2 from weld toe are 3.84 mm and 14.06 mm respectively. For example, the strain ranges for SG1 and SG2 of WTJ5 is 1137.0 με and 606.9 με respectively. The extrapolated strain at the hot-spot location is 1337.7 με for which the calculated stress range is 267.5 MPa. Schematics of hot-spot strain extrapolation for specimens WTJ4 to WTJ6 are plotted in Figures 4.22 to Figure 4.24. Table 4.2 lists the hot-spot strain range readings for WTJ4 to WTJ6. All three specimens have large strain ratio between SG1 reading and SG2 reading (between 1.78-1.87). This confirms again that large stress

concentration did occur at the weld toe of the welded tubular joint specimens. These hot-spot stress will be used in fatigue prognosis study in the following chapter.

4.3.3 Fracture surface features

The facture surfaces of specimens WTJ1, WTJ4, WTJ5 and WTJ6 were opened and examined for surface features after the completion of the fatigue test. Three zones of fatigue propagation are identified from the fracture surface of all four specimens: the origin zone, the slow fracture zone and the fast fracture zone, as shown in Figures 4.25 to 4.32. This is consistent with current understanding of fatigue fracture surface features (see, e.g., Sachs 2005). At the origin zone, the crack development is very slow and the fracture surface is darker in color. For the slow fracture zone, the fracture surface become lighter in color and is relatively smooth since the propagation of crack at this stage is steady and stable. The last phase of crack development corresponds to the fast fracture zone on the fracture surface, which becomes rough and irregular compared with the slow fracture zone. In Figures 4.25 to 4.32, pictures of these three zones are shown for specimens WTJ1, WTJ4, WTJ5 and WTJ6.

For WTJ1, dye penetrant was applied when the crack was first seen with naked eye. The dried red ink of the dye penetrant left a red water mark on the fracture surface, as shown in Figure 4.33. The red watermark recorded the crack front at the time when the dye penetrant was sprayed. The watermark clearly shows a semi-elliptical shape, which has a length ($2c$) of 62 mm and a depth (a) of 6 mm. The aspect ratio for the semi-elliptical crack front is thus around 0.2. This is in good agreement with the assumed aspect ratio value of 0.2 suggested by Vosikovsky *et al* (1985). Therefore for WTJ1, the aspect ratio assumption is supported with experimental observation.

For specimen WTJ6, beach-marking method is applied to generate crack front prints on the fracture surface at specified load cycles. A total of five marks are supposed to occur according to the loading plan. From Figure 4.34, it can be seen that there are only three beach marks visible on the fracture surface. Those three are believed to be the marks from the first three beach marking loading. This is confirmed using digital microscope. The last two marks are missing because the crack has penetrated the tube wall thickness before these two marks could occur and the specimen entered the fast propagation stage. The crack in specimen WTJ6 has multiple initiations which correspond to the multiple dark spots at the origin in Figure 4.31. Therefore, the shape of the beach mark is not semi-elliptical as expected. The first beach mark has a surface length of 33 mm and a depth of 1.5 mm. The second beach mark has a length of 55 mm and depth of 2.5 mm. The third beach mark has a length of 94 mm and depth of 5m. The aspect ratio is no longer consistent with the assumed aspect ratio value since it is applicable for single crack initiation only.

Schematics of fatigue crack growth over the fracture surface of specimen WTJ1, WTJ4, WTJ5 and WTJ6 are also presented in Figures 4.35 to 4.38. The three crack propagation zones are marked in the figures.

4.4 Conclusions

Fatigue tests on six identical welded tubular joint specimens are carried out. Test data of applied load, strain and crack information are acquired. The strain data shows that high stress concentration occurred at hot-spot locations near weld toe. Fatigue crack initiates at the weld toe on the top ridge of the tube specimens and propagate along the weld toe in both directions. Recorded load data shows that with crack propagating

along the weld toe, the stiffness of the test specimen decreases considerably due to reduced tube section area at the fractured section location.

As for the crack length measurement, three different techniques were tested including dye penetrant, phased array ultrasonic and digital microscope. It is found that digital microscope is able to detect small cracks before the other two techniques could. Generally speaking, crack detection and measurement is very challenging when the crack length is small (e.g., less than 10 mm).

By applying dye penetrant on WTJ1 and beach marking on WTJ6, the crack front shape is recorded on fracture surface. The water mark left on the fracture surface of WTJ1 by dye penetrant ink has a semi-elliptical shape with an aspect ratio of 0.2, which is in close agreement with the assumed aspect ratio value at that stage. Yet for the beach marks on WTJ6, because of multiple crack initiations, they are not exactly semi-elliptical in shape and have aspect ratio values much larger than the assumed aspect ratio values for single crack.

By examining the crack surface of specimens WTJ1, WTJ4, WTJ5 and WTJ6, it can be concluded that crack propagation can be divided into three stages according to the surface features of the fracture surface: the origin zone, the slow fracture zone and the fast fracture zone. Each stage corresponds to a different surface features over the fracture surface.

Table 4.1. Fatigue test parameters of the six test specimens

	Shear Force			Bending Moment			Test termination load cycle & crack length	
	P_{max} (kN)	P_{min} (kN)	ΔP	M_{max} (kN-m)	M_{min} (kN-m)	ΔM	($x10^5$ cycles)	(mm)
WTJ1	25.35	3.43	21.92	45.72	6.19	39.53	6.19	251
WTJ2	24.82	2.76	22.06	37.20	4.14	33.06	12.46	181
WTJ3	27.93	1.77	26.16	41.86	2.65	39.20	2.18	320
WTJ4	27.43	0.91	26.52	41.11	1.36	39.74	5.82	342
WTJ5	28.30	1.82	26.48	42.41	2.73	39.68	3.90	337
WTJ6	27.78	1.39	26.39	41.63	2.08	39.55	3.55	358

Table 4.2. Strain range at hot-spot

	SG1 (με)	SG2 (με)	Ratio (SG1/ SG2)
WTJ4	1390.7	779.6	1.78
WTJ5	1137.0	606.9	1.87
WTJ6	1301.2	717.6	1.81

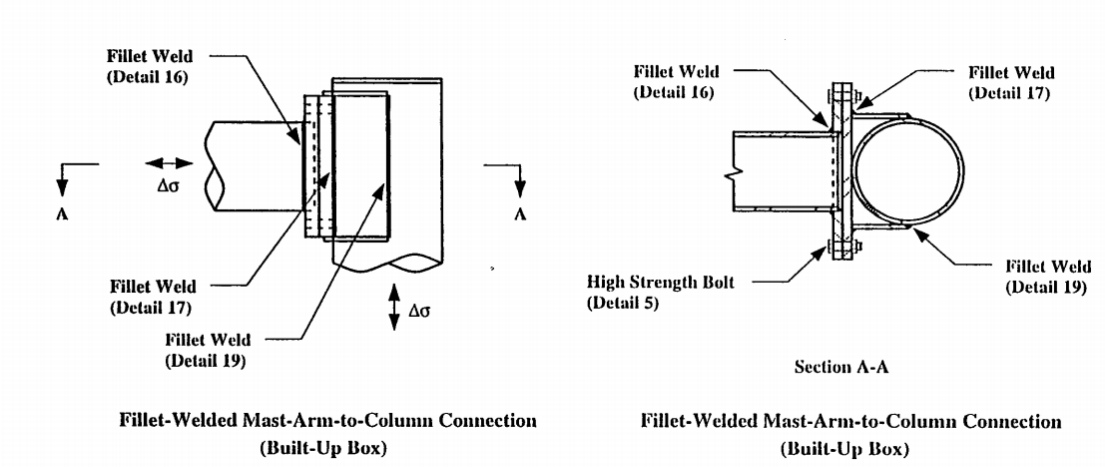

Figure 4.1. Fatigue detail of fillet-welded Mast-Arm-to-Column connection (Detail 16) (from Kaczinski et al 1998)

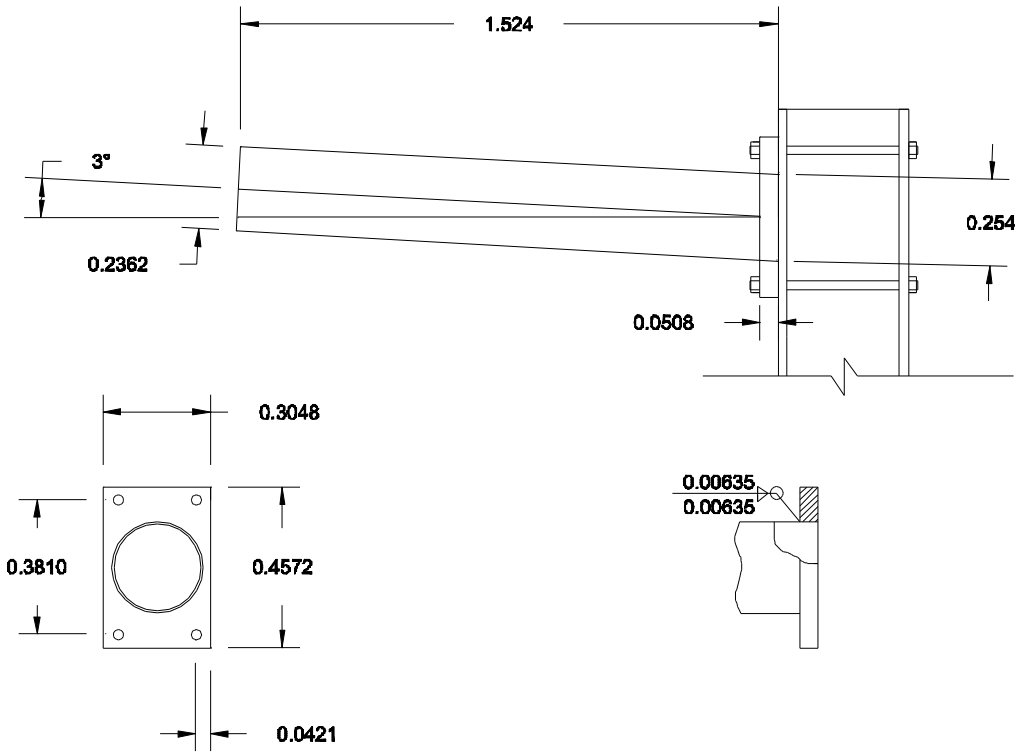

Figure 4.2. Dimension of test specimen (unit: m)

Figure 4.3. Fatigue test setup

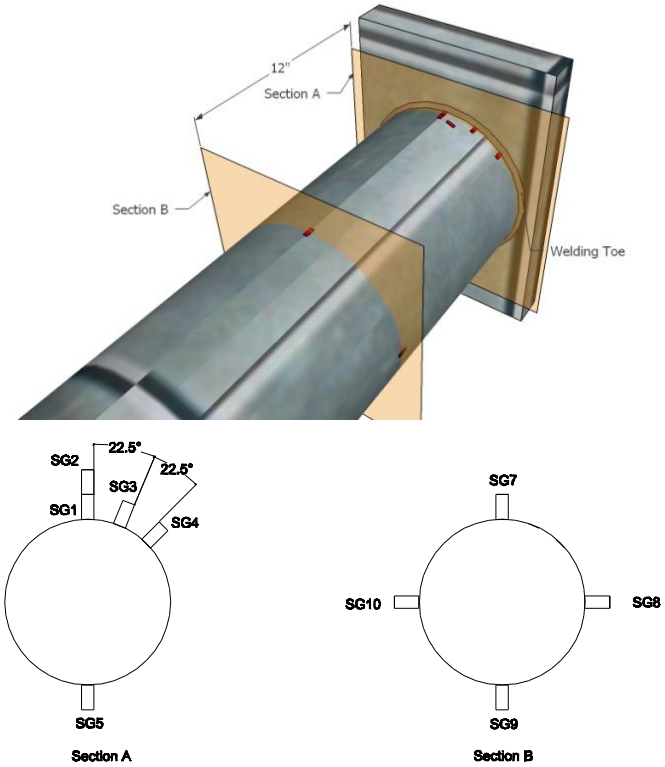

Figure 4.4. Location of strain gauges

(a)

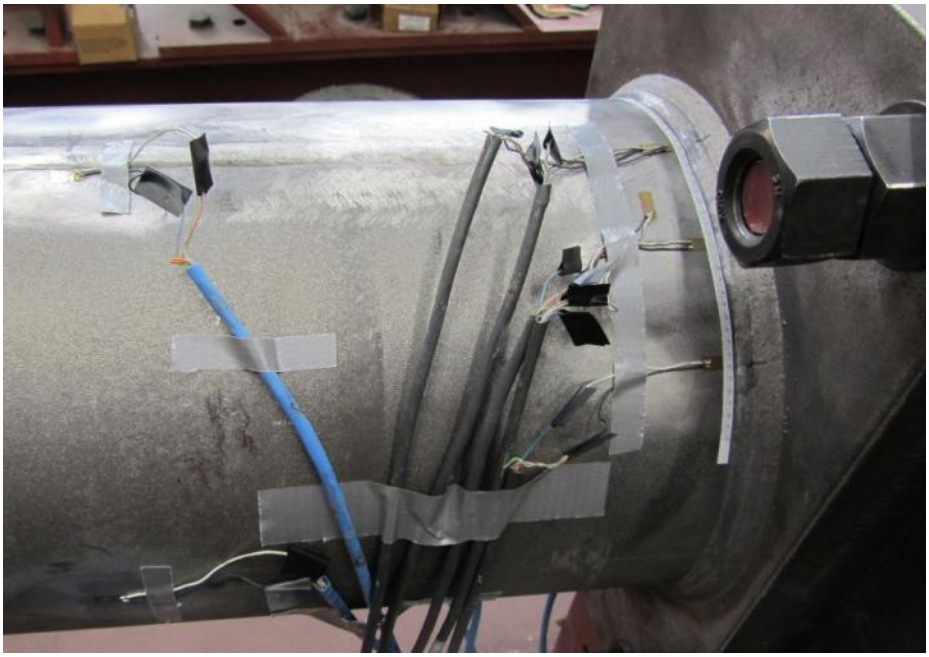

(b)

Figure 4.5. View of strain gauges on specimen

Figure 4.6. Measuring crack size using digital microscope

Figure 4.7. Crack at the weld toe of test specimen (dark red line identified with dye penetrant)

(a) Load cycle N = 127,800

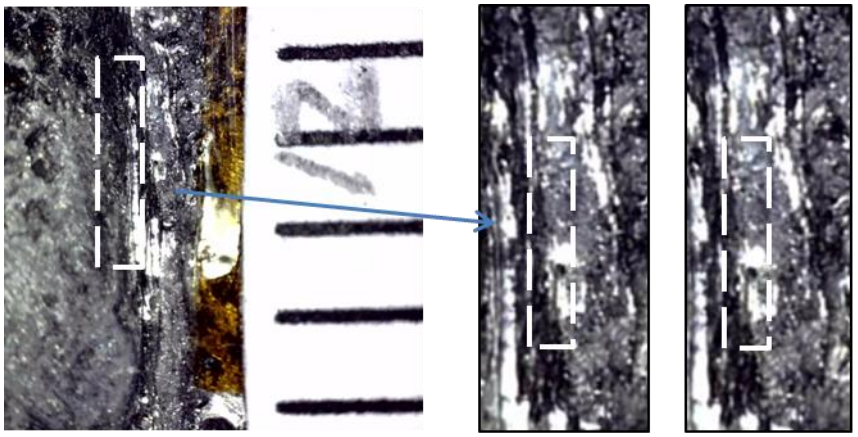

(b) Load cycle N = 355,100

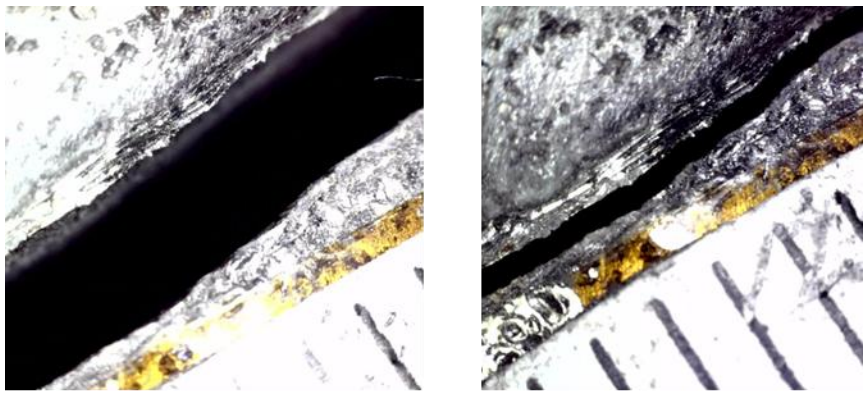

Figure 4.8. Microscope image of fatigue crack growth in WTJ6: (a) Initial stage; (b) Crack at failure

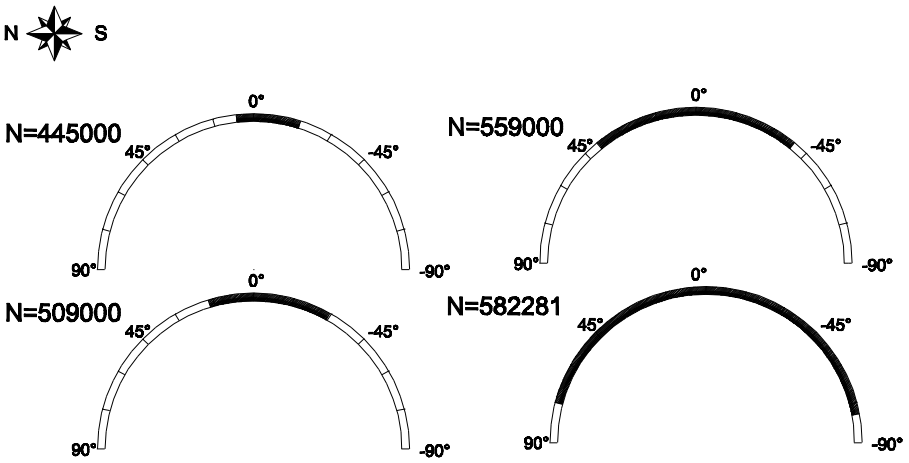

Figure 4.9. Fatigue crack initiation and propagation on WTJ4

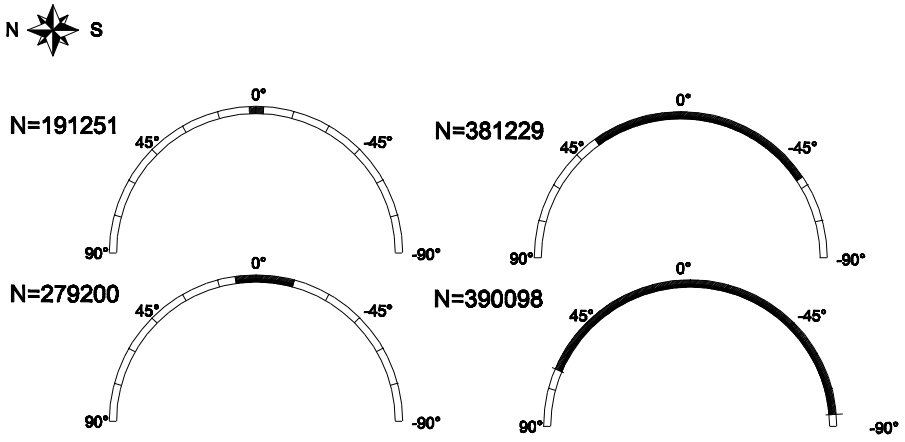

Figure 4.10. Fatigue crack initiation and propagation on WTJ5

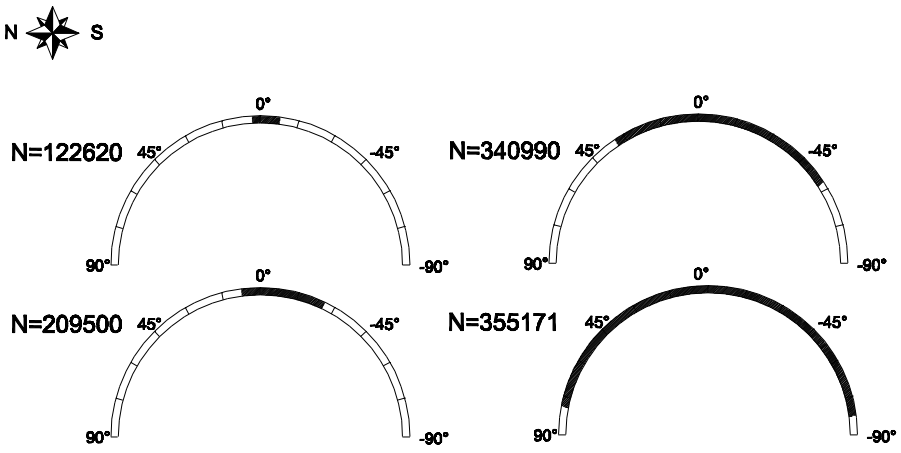

Figure 4.11. Fatigue crack initiation and propagation on WTJ6

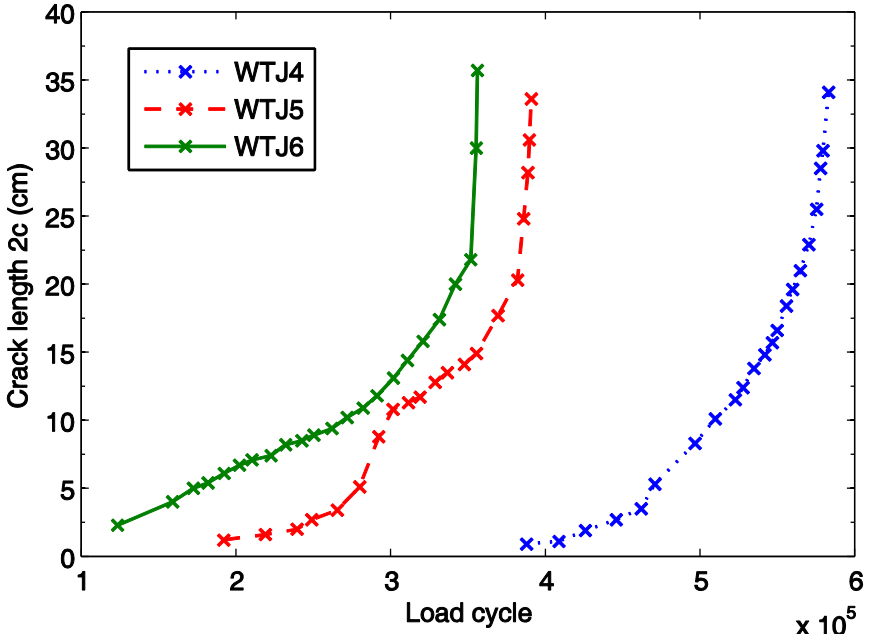

Figure 4.12. Crack growth curves

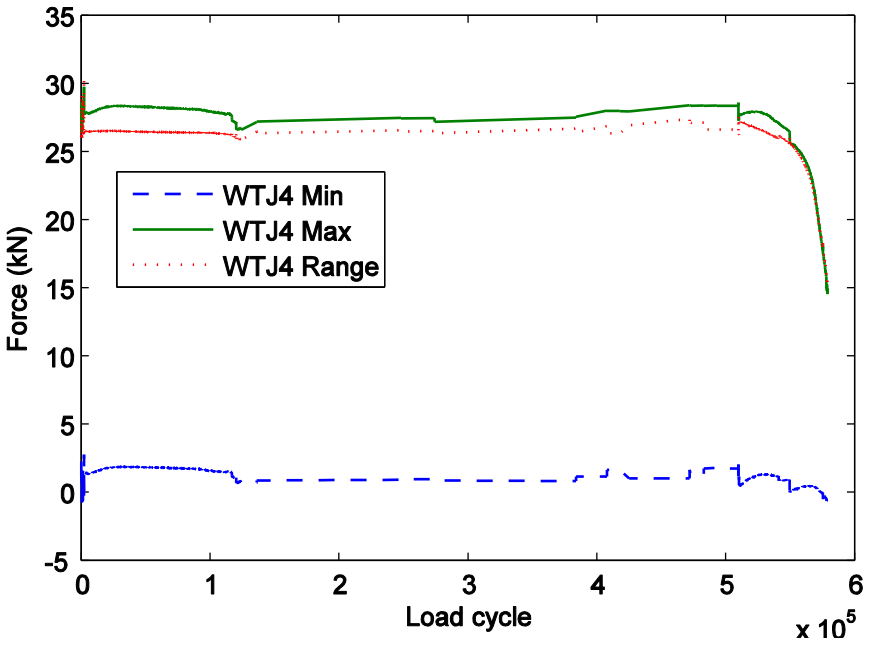

Figure 4.13. Load history of fatigue test for WTJ4

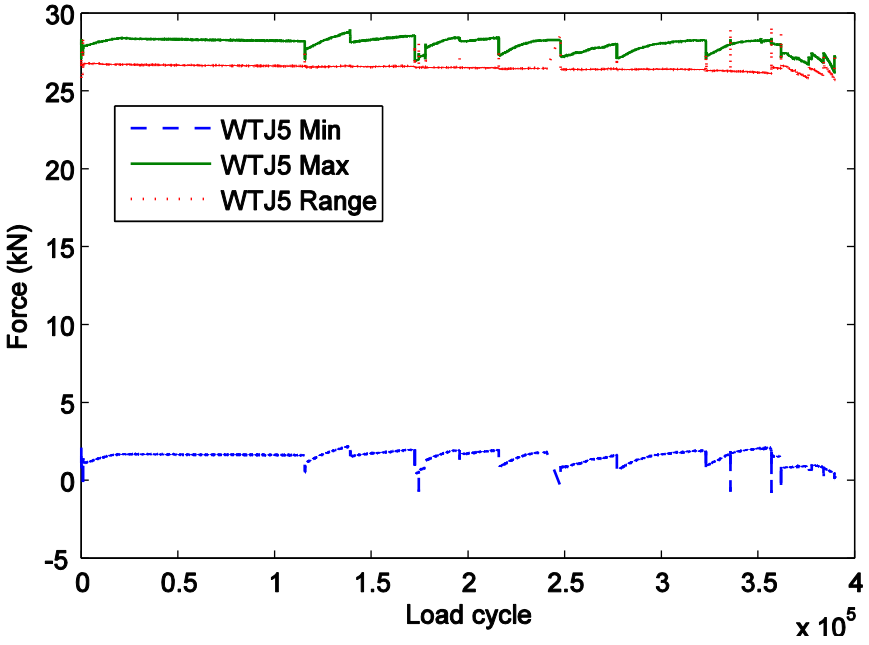

Figure 4.14. Load history of fatigue test for WTJ5

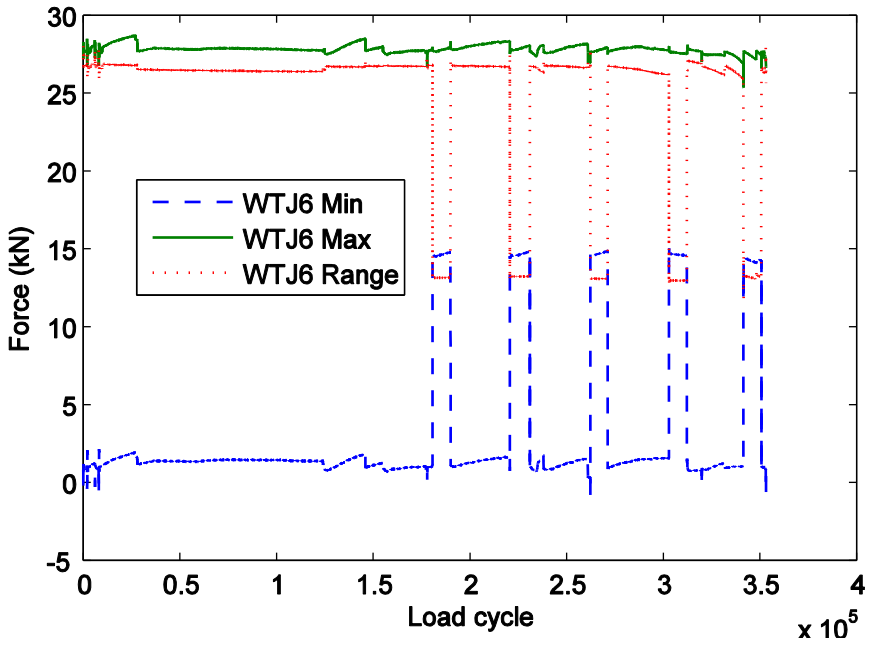

Figure 4.15. Load history of fatigue test for WTJ6

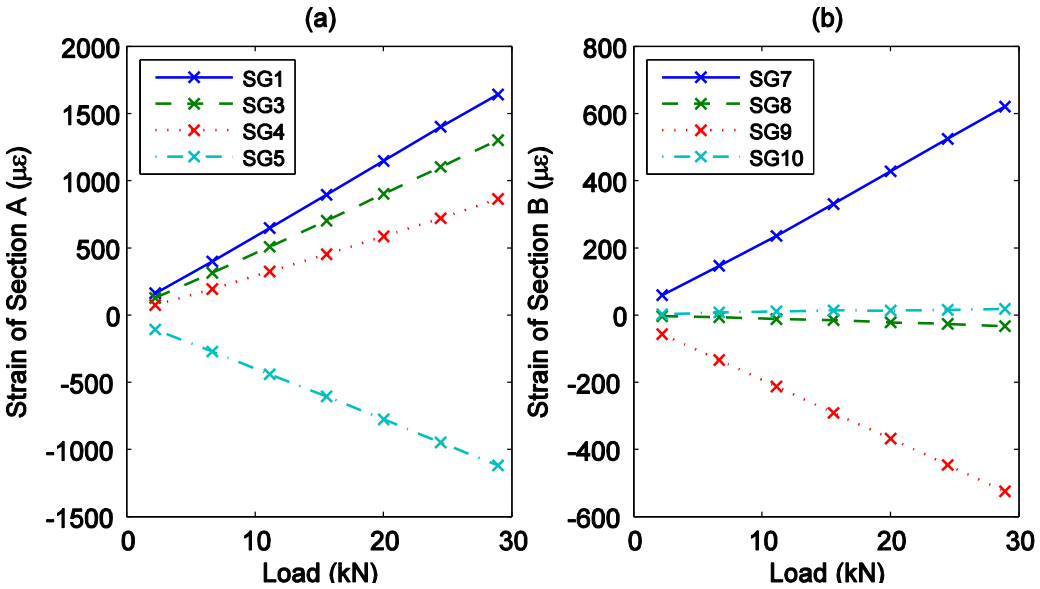

Figure 4.16. Strain distribution over the sections of WTJ4: (a) Section A; (b) Section B

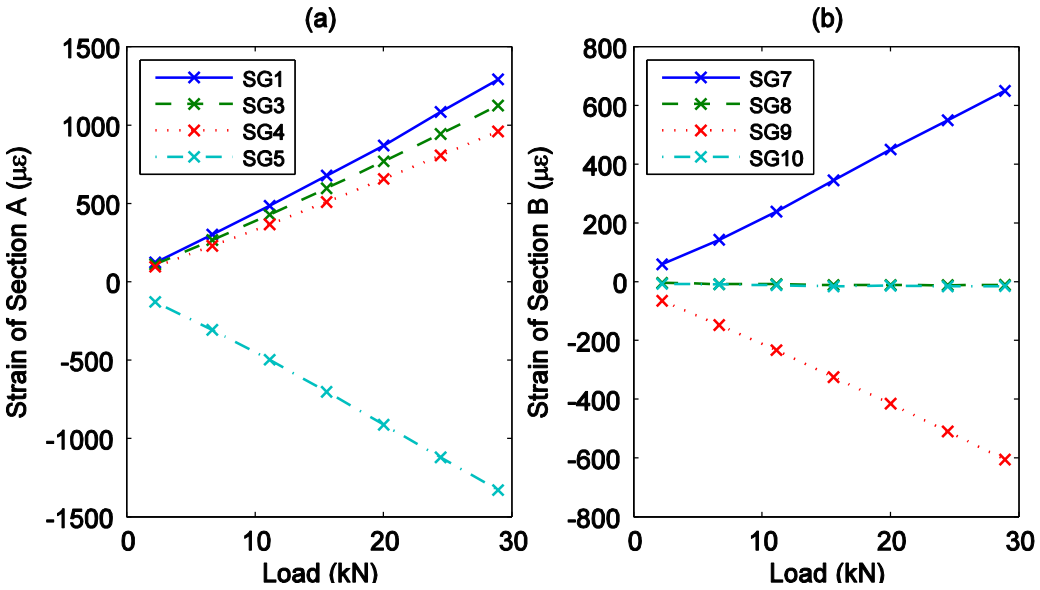

Figure 4.17. Strain distribution over the sections of WTJ5: (a) Section A; (b) Section B

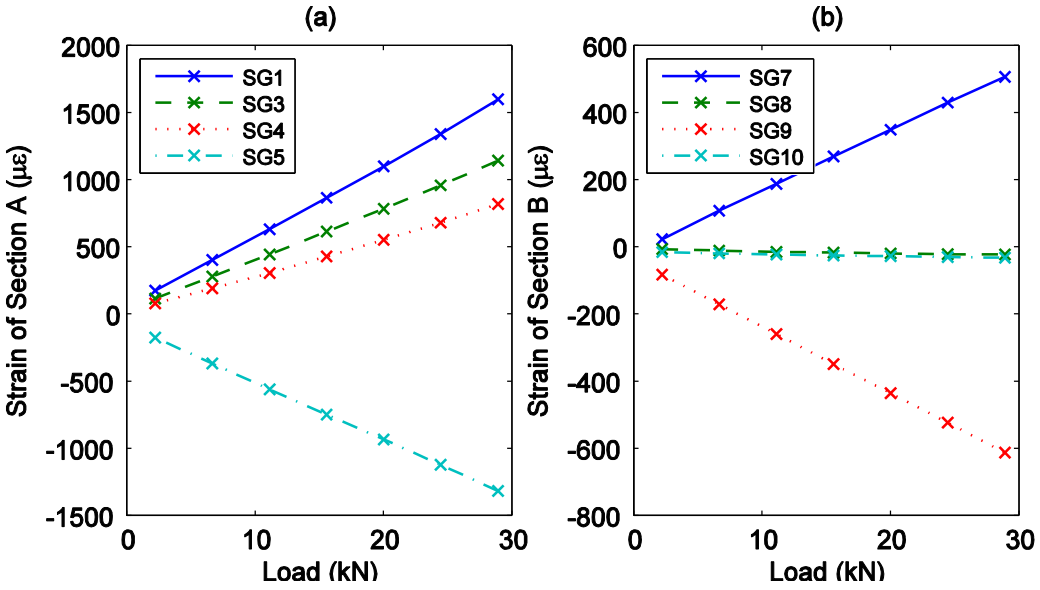

Figure 4.18. Strain distribution over the sections of WTJ6: (a) Section A; (b) Section B

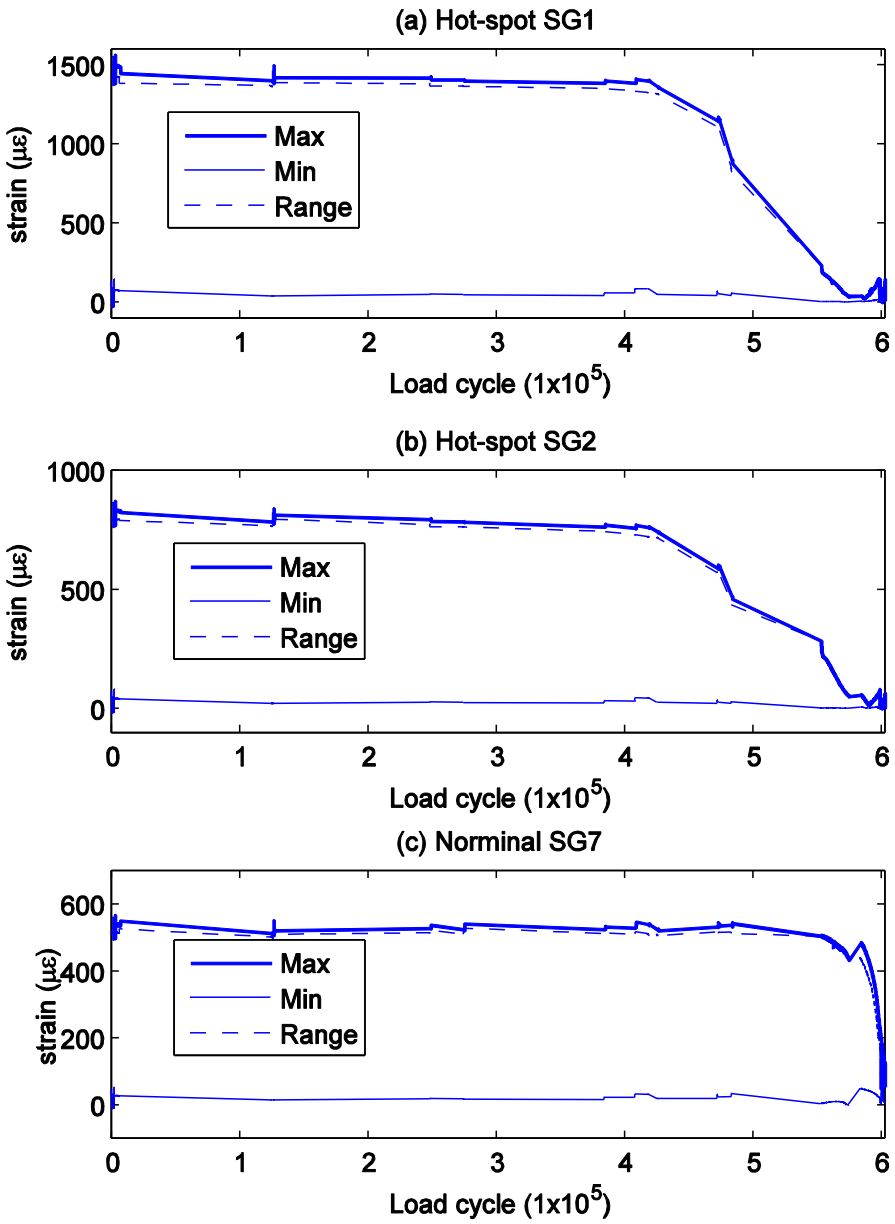

Figure 4.19. Strain history recorded in fatigue test of WTJ4

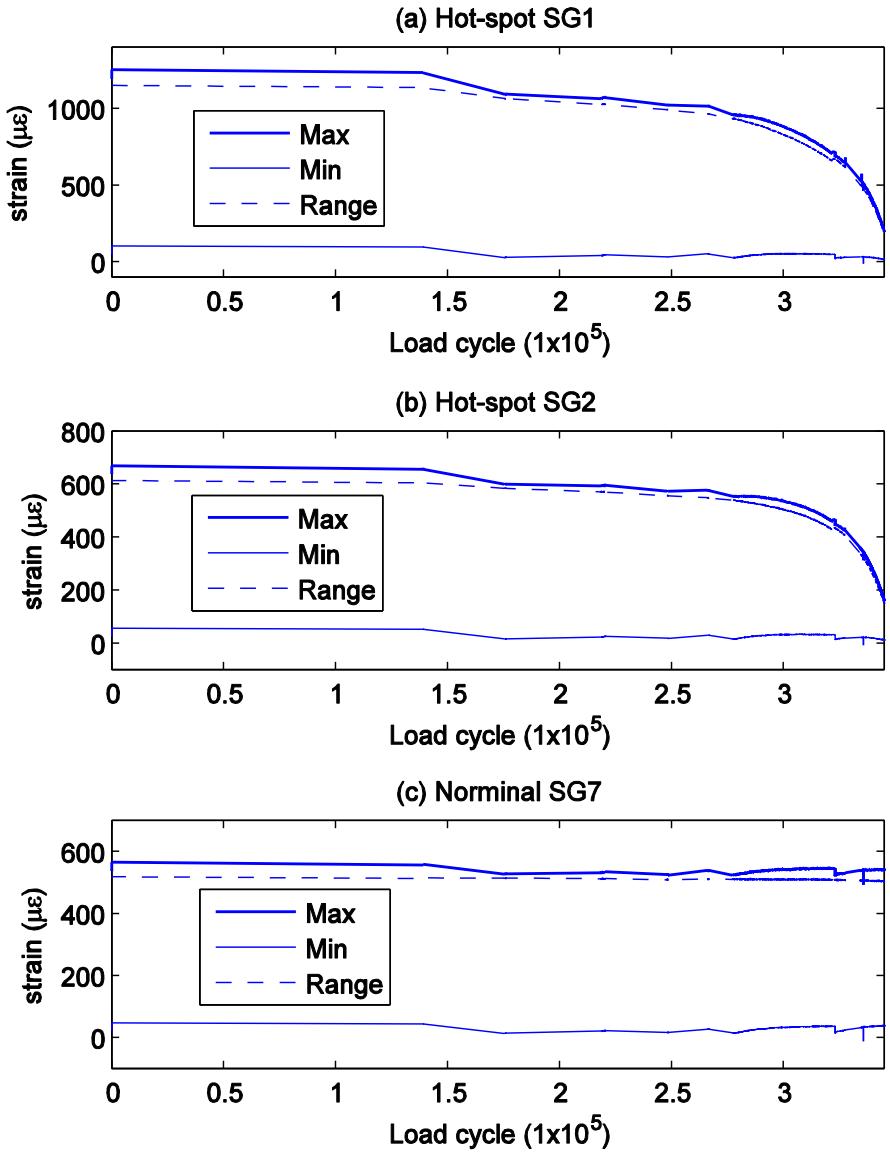

Figure 4.20. Strain history recorded in fatigue test of WTJ5

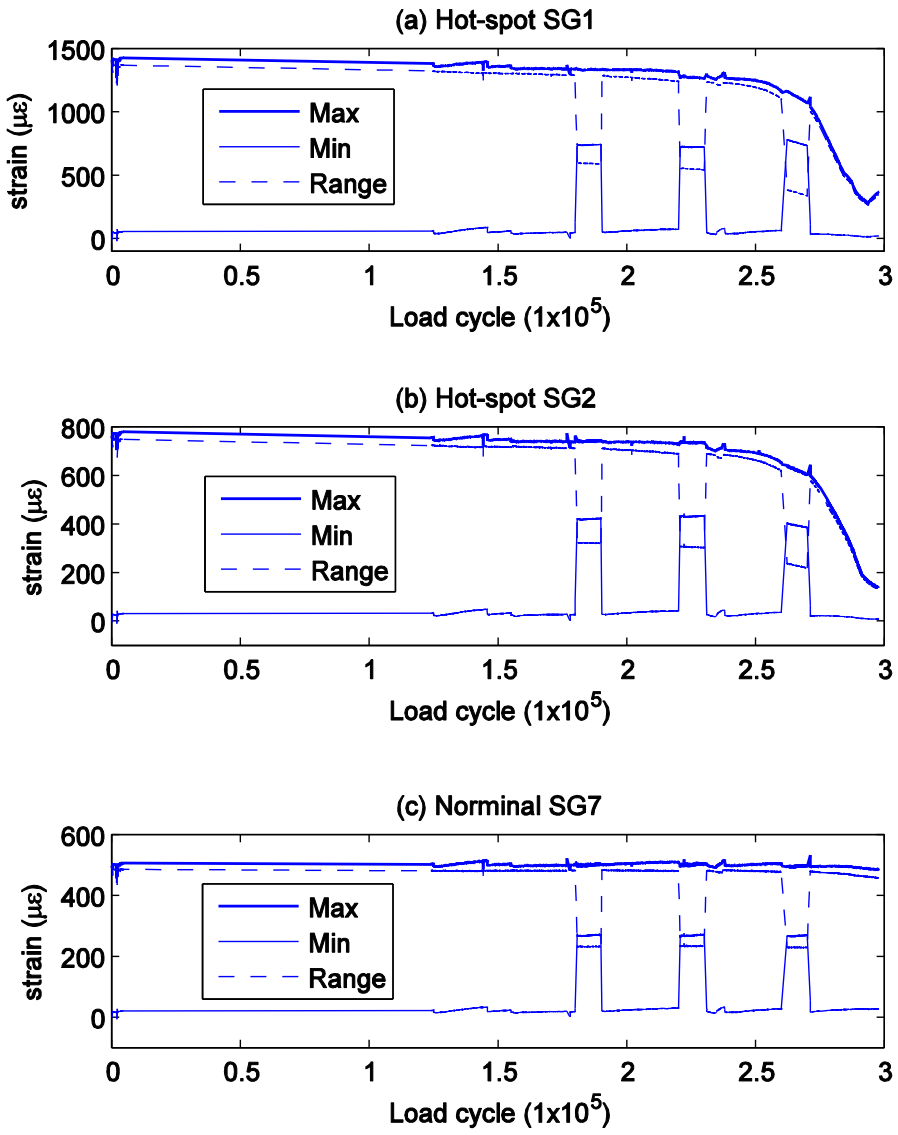

Figure 4.21. Strain history recorded in fatigue test of WTJ6

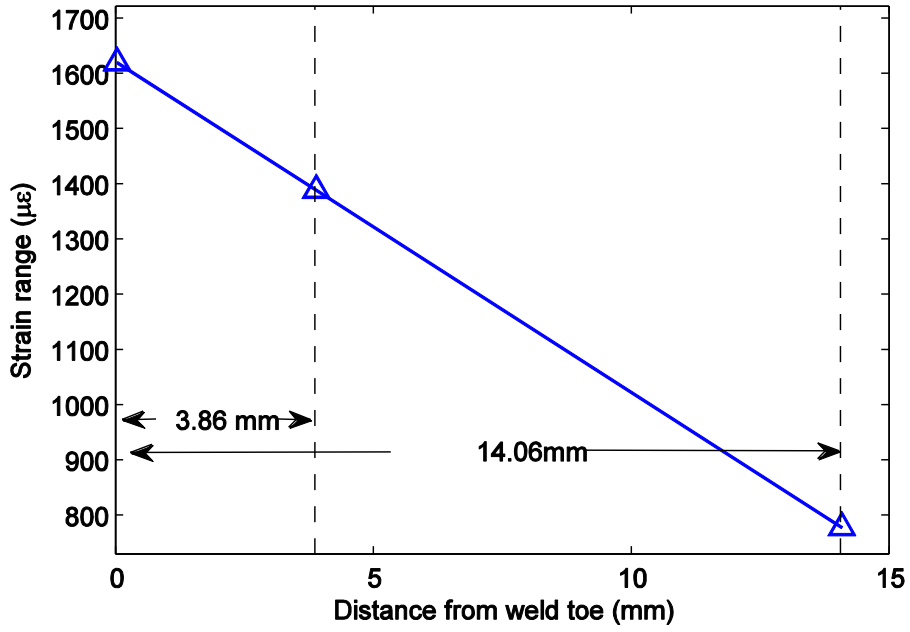

Figure 4.22. Schematics of hot-spot strain extrapolation of WTJ4

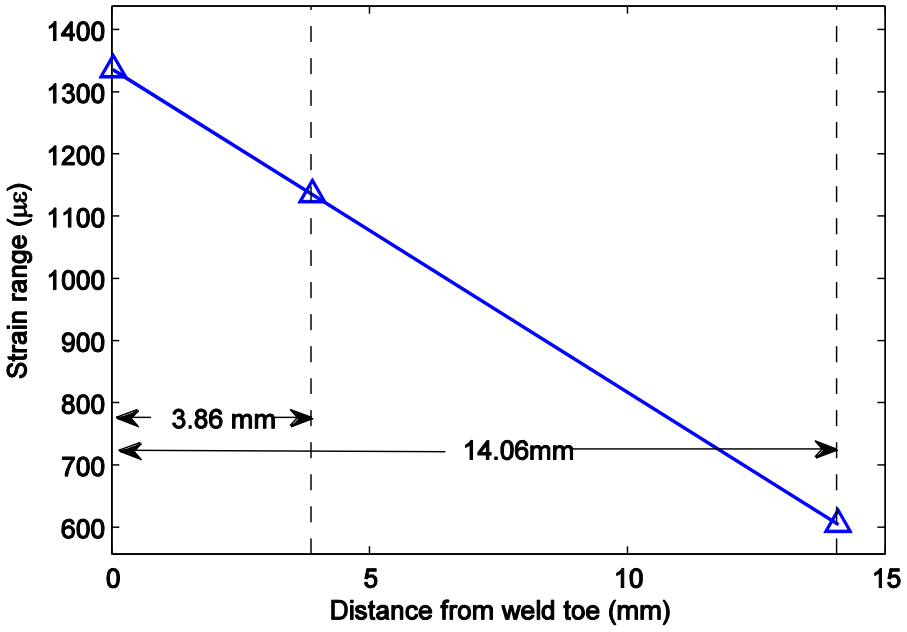

Figure 4.23. Schematics of hot-spot strain extrapolation of WTJ5

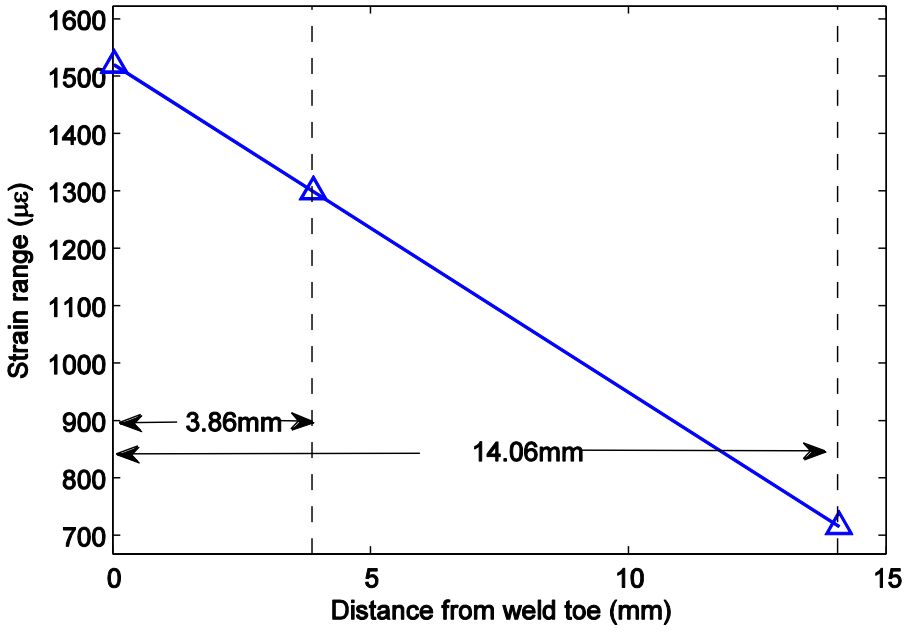

Figure 4.24. Schematics of hot-spot strain extrapolation of WTJ6

(a)

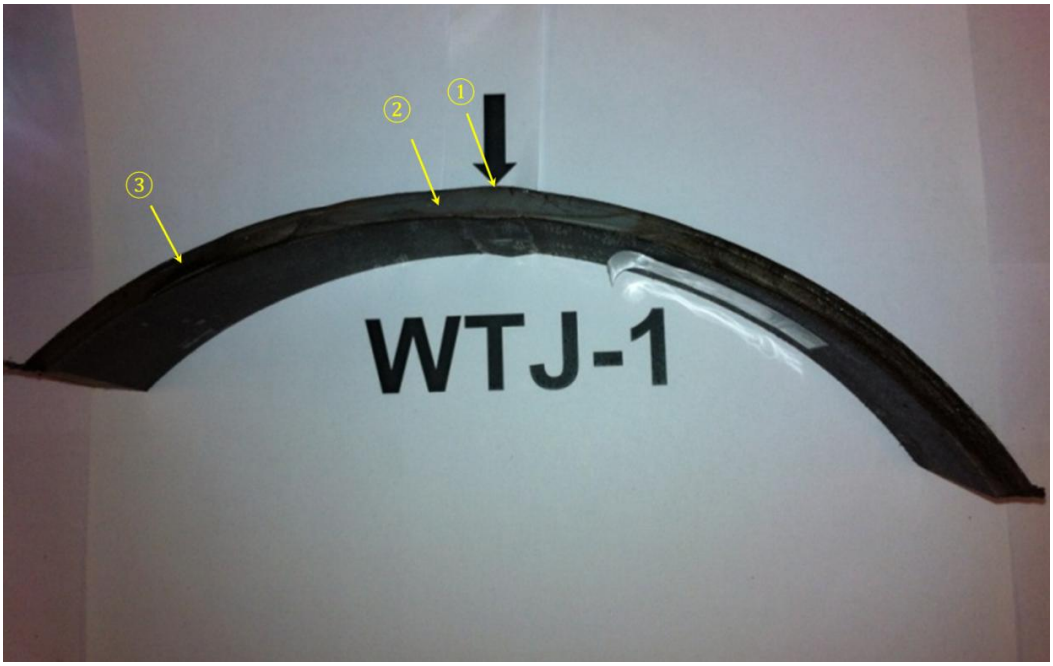

(b) Origin zone

Figure 4.25. Pictures of crack propagation zones on the fracture surface of specimen WTJ1 (magnification factor for microscopic image labeled 1, 2, 3 = 65): (a), (b)

(c) Slow fracture zone

(d) Fast fracture zone

Figure 4.26. Pictures of crack propagation zones on the fracture surface of specimen WTJ1 (magnification factor for microscopic image labeled 1, 2, 3 = 65): (c), (d)

(a)

(b) Origin zone

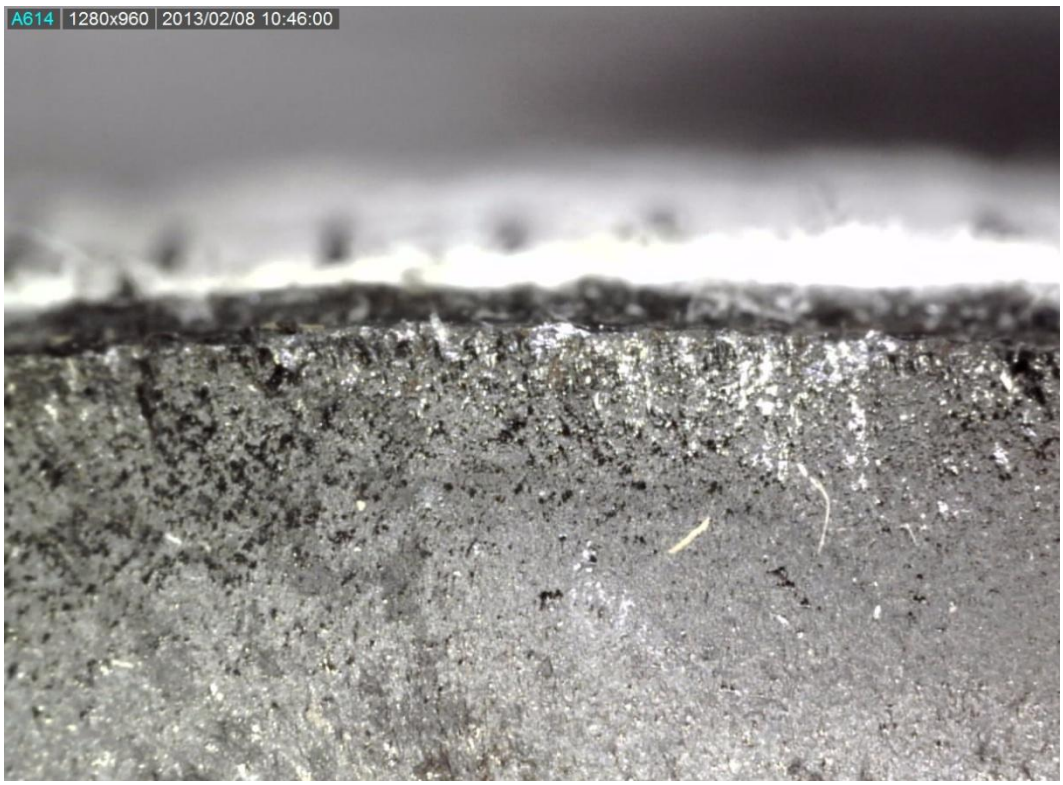

Figure 4.27. Pictures of crack propagation zones on the fracture surface of specimen WTJ4 (magnification factor for microscopic image labeled 1, 2, 3 = 65): (a), (b)

(c) Slow fracture zone

(d) Fast fracture zone

Figure 4.28. Pictures of crack propagation zones on the fracture surface of specimen WTJ4 (magnification factor for microscopic image labeled 1, 2, 3 = 65): (c), (d)

(a)

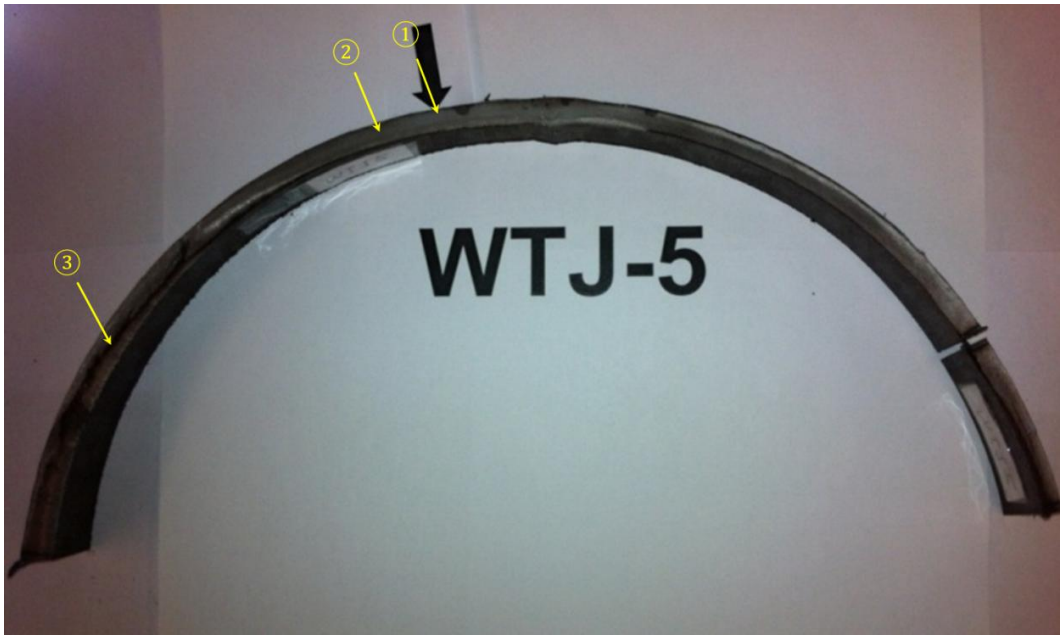

(b) Origin zone

Figure 4.29. Pictures of crack propagation zones on the fracture surface of specimen WTJ5 (magnification factor for microscopic image labeled 1, 2, 3 = 65): (a), (b)

(c) Slow fracture zone

(d) Fast fracture zone

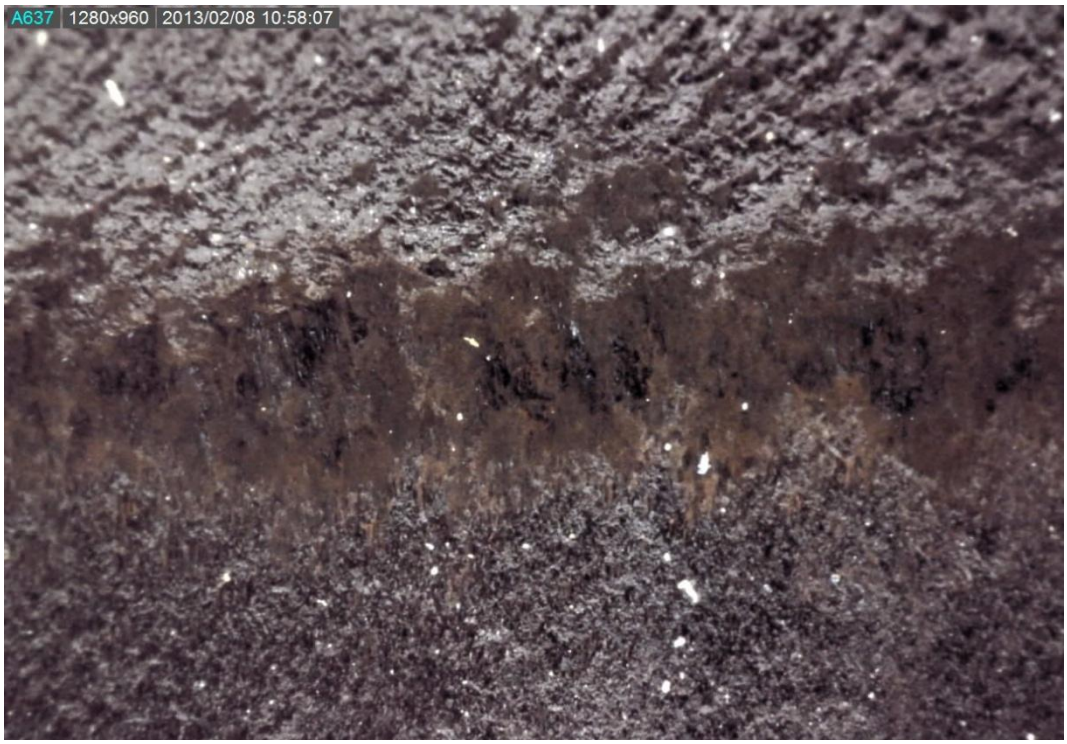

Figure 4.30. Pictures of crack propagation zones on the fracture surface of specimen WTJ5 (magnification factor for microscopic image labeled 1, 2, 3 = 65): (c), (d)

(a)

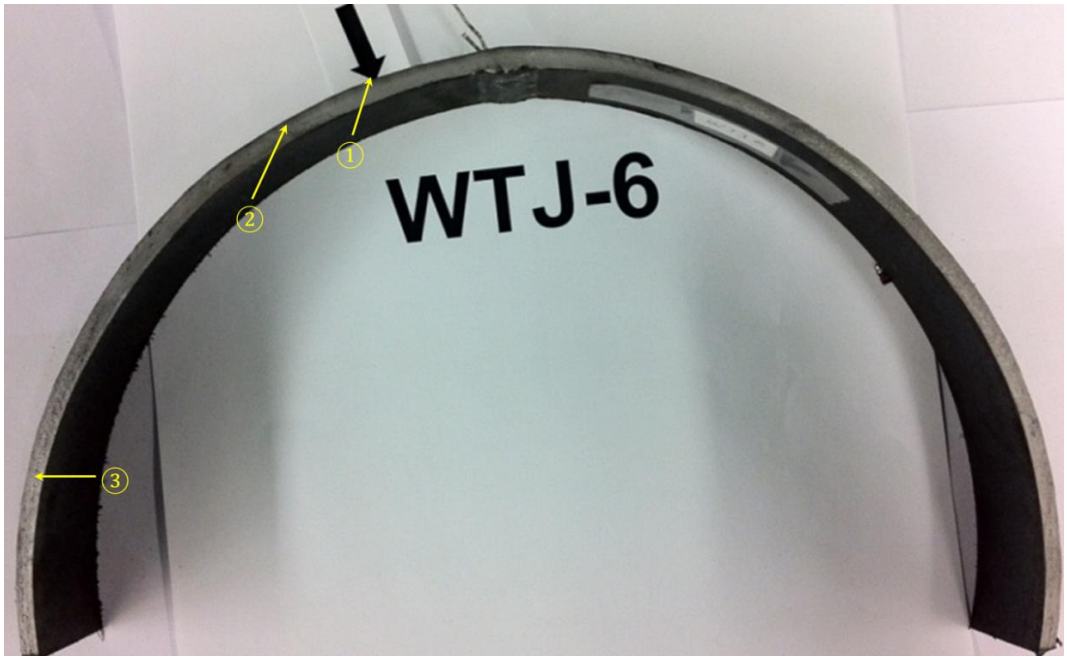

(b) Origin zone

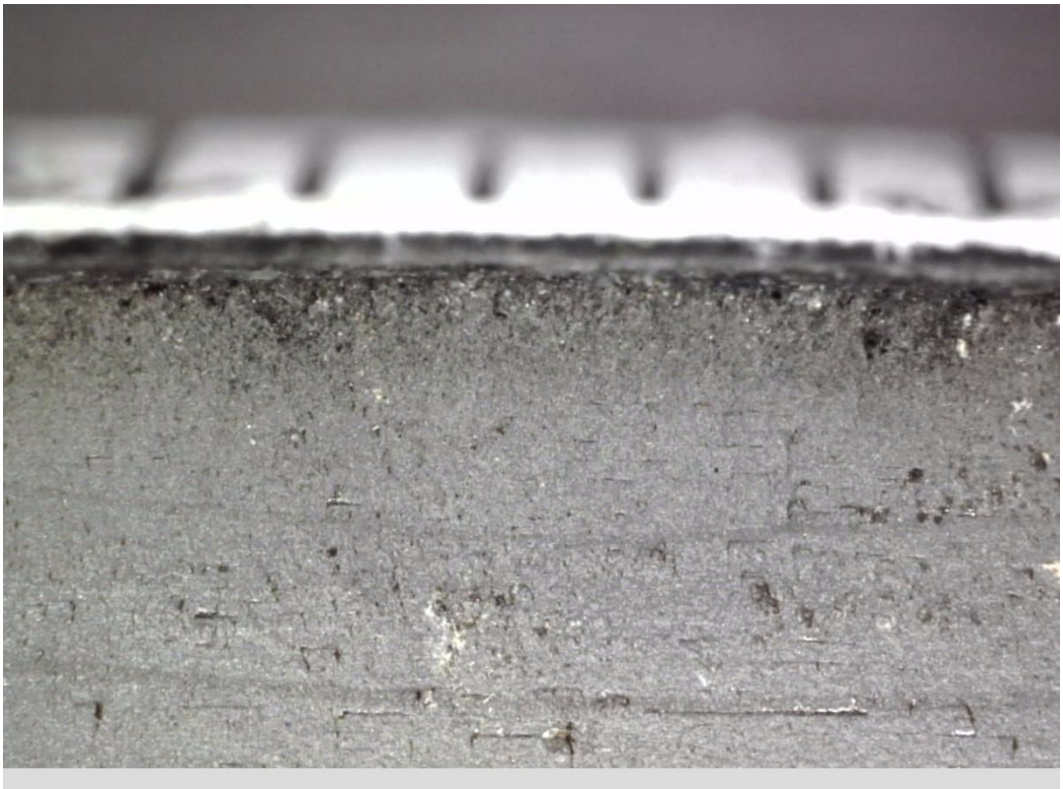

Figure 4.31. Pictures of crack propagation zones on the fracture surface of specimen WTJ6 (magnification factor for microscopic image labeled 1, 2, 3 = 65): (a), (b)

(c) Slow fracture zone

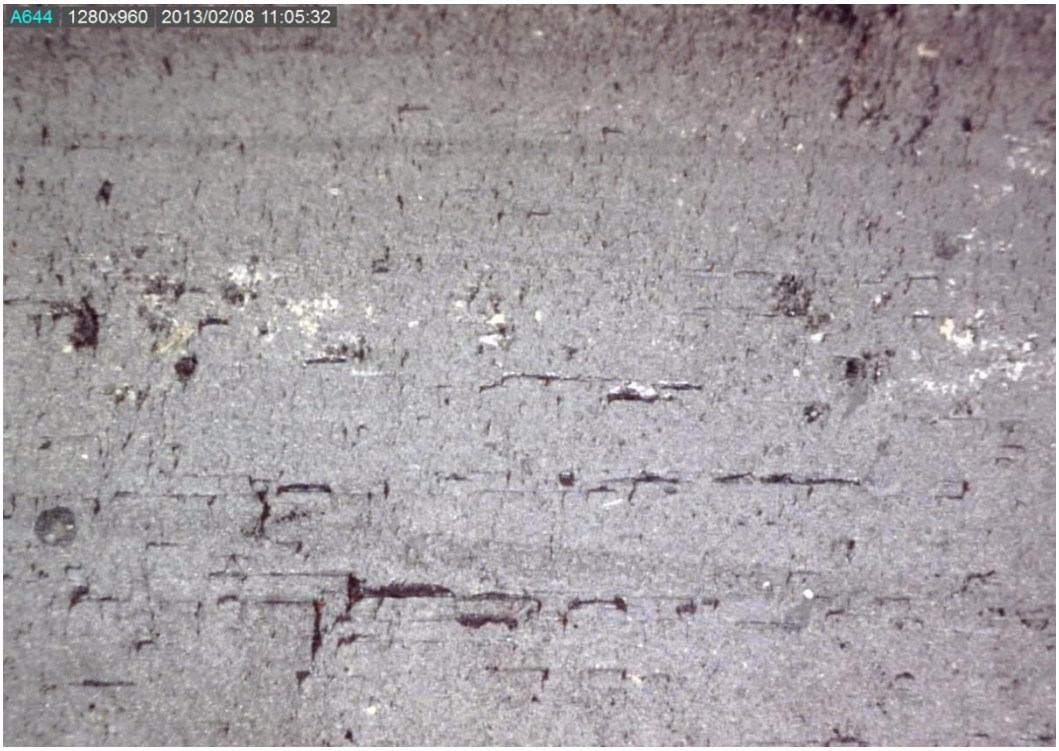

(d) Fast fracture zone

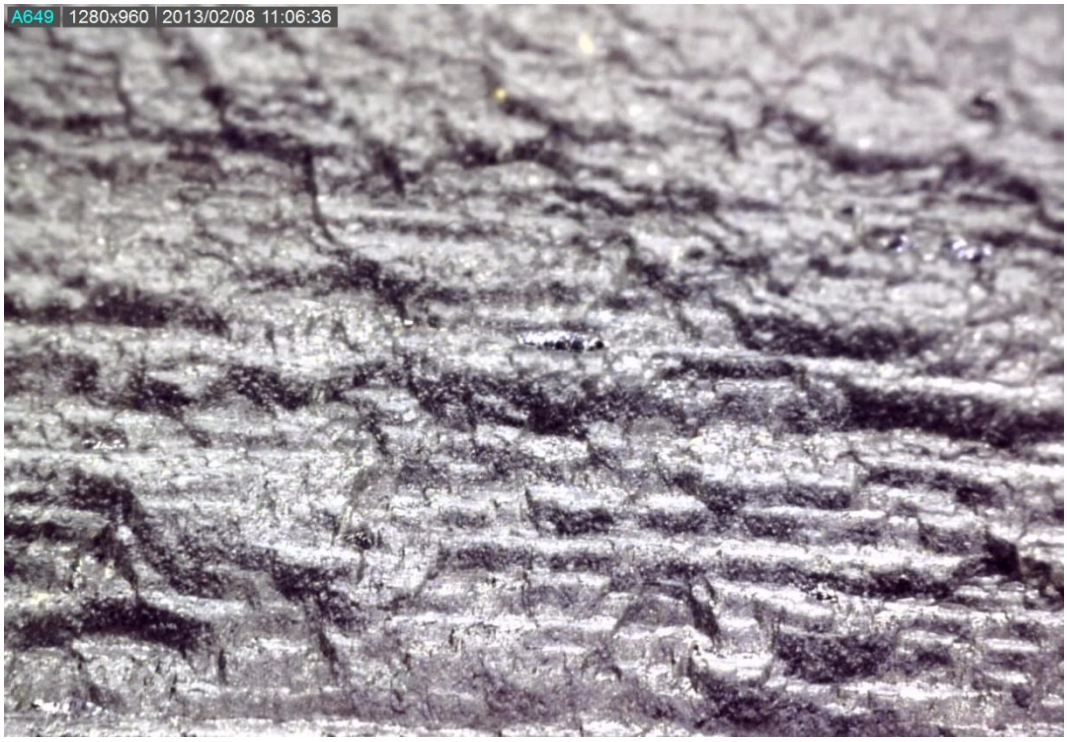

Figure 4.32. Pictures of crack propagation zones on the fracture surface of specimen WTJ6 (magnification factor for microscopic image labeled 1, 2, 3 = 65): (c), (d)

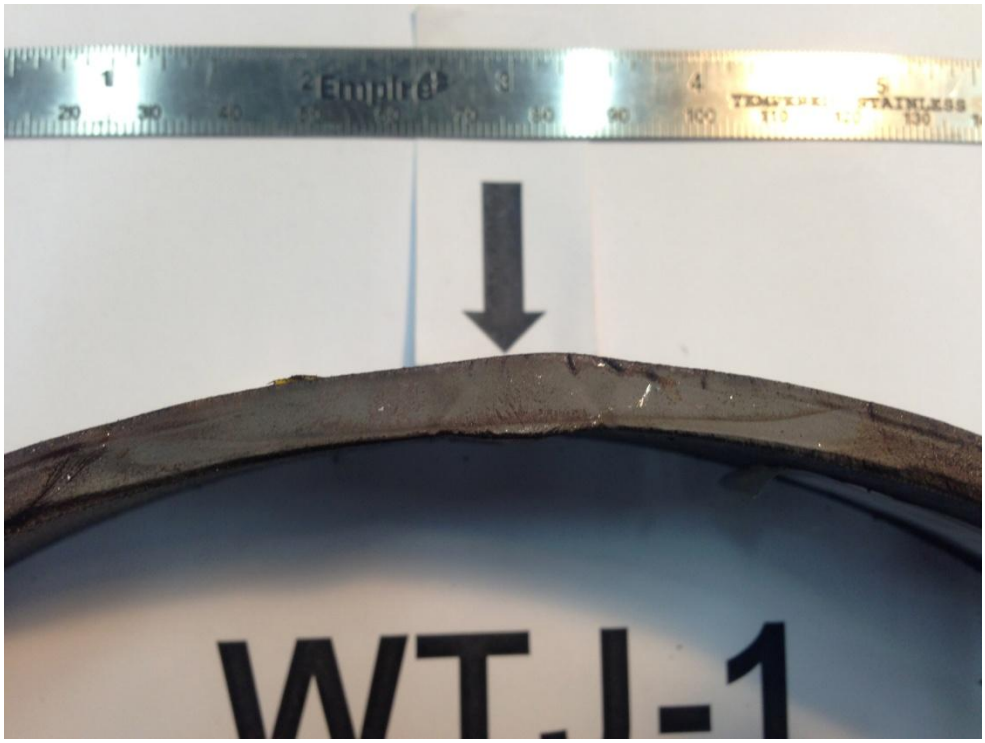

Figure 4.33. Dye penetrant mark on WTJ1

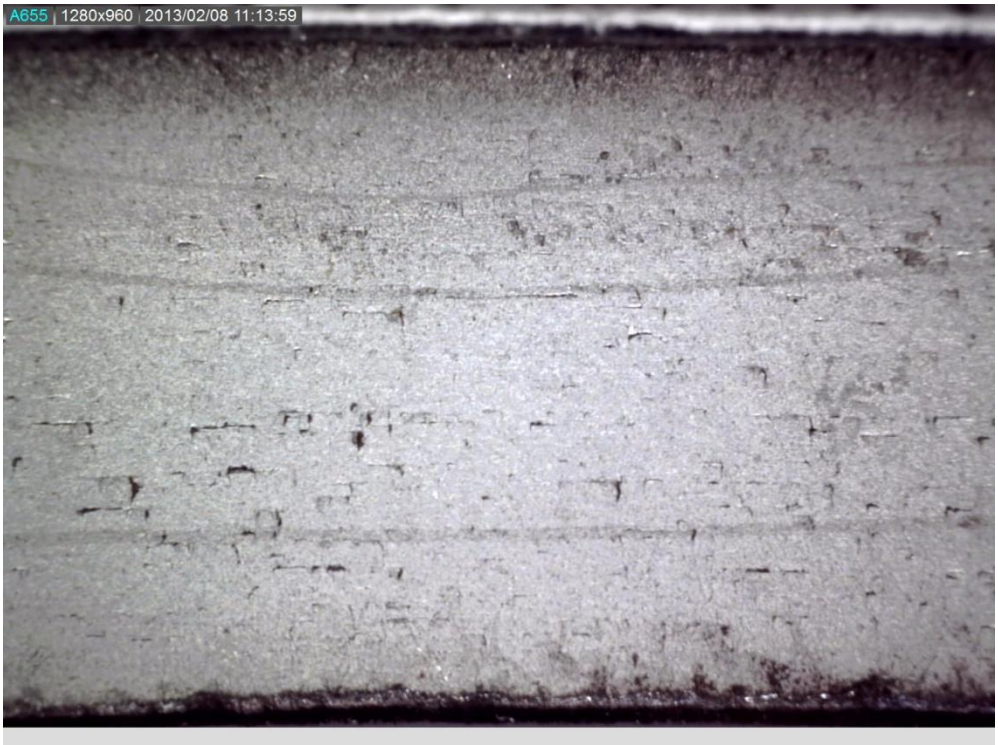

Figure 4.34. Beach marks on WTJ6 (magnification factor = 43)

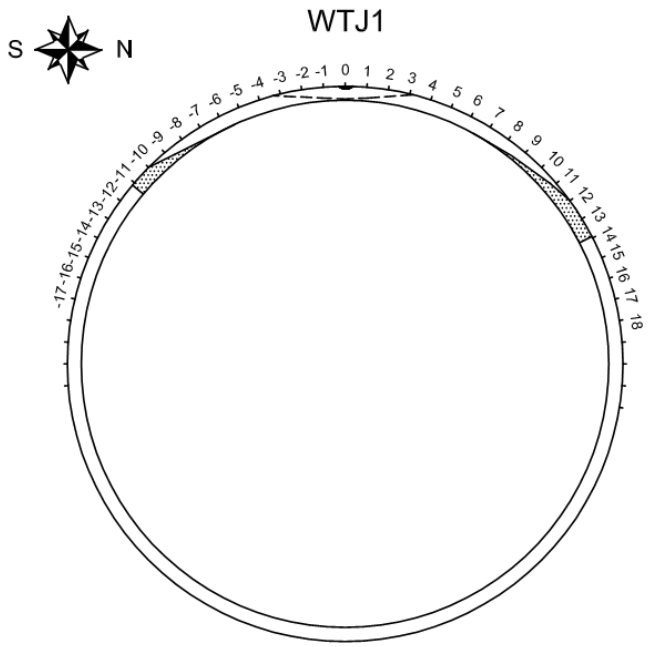

Figure 4.35. Crack propagation along surface for WTJ1

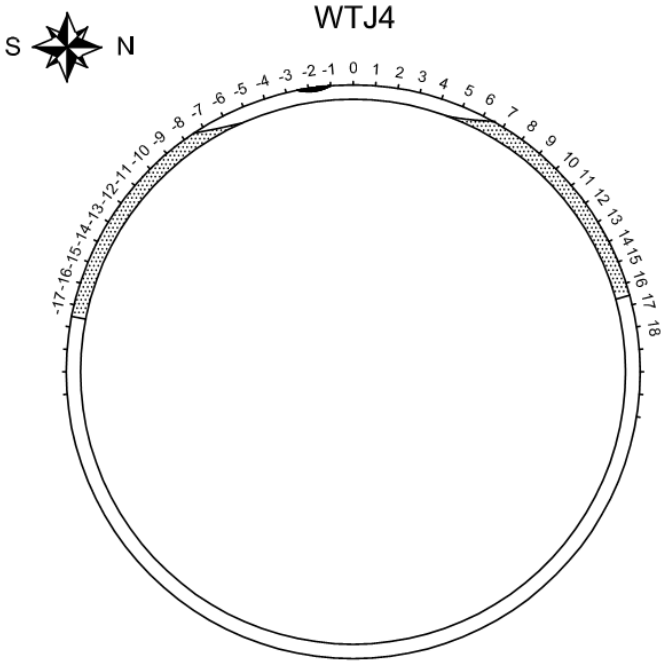

Figure 4.36. Crack propagation along surface for WTJ4

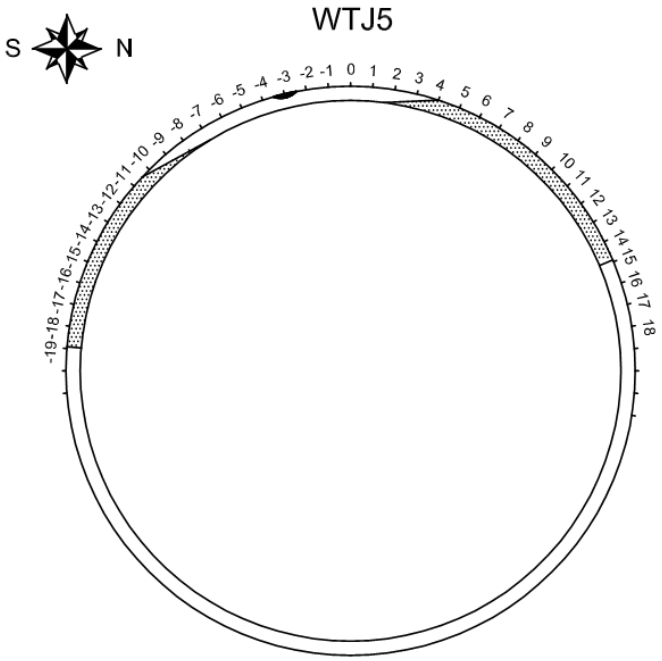

Figure 4.37. Crack propagation along surface for WTJ5

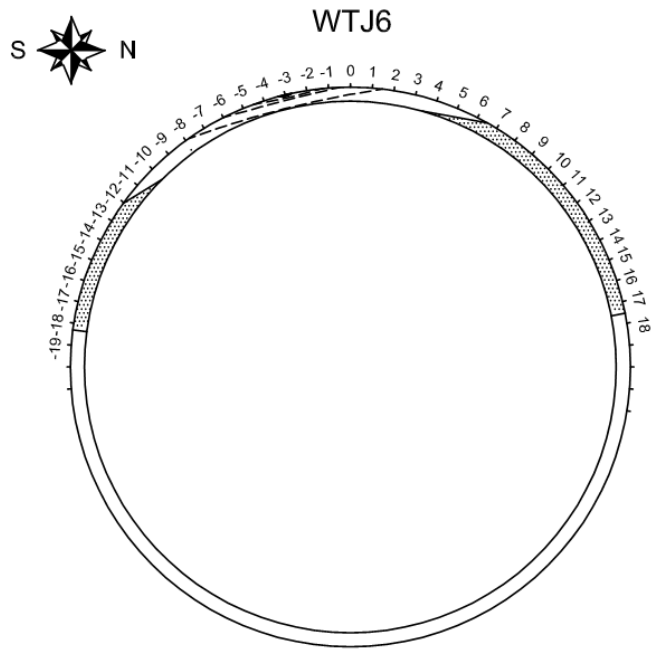

Figure 4.38. Crack propagation along surface for WTJ6

Chapter 5: Structural Health Prognosis Procedure

5.1 Introduction

This chapter presents a general procedure for sensor-driven structural health prognosis and probabilistic maintenance scheduling. The proposed procedure utilizes Bayesian theorem for updating the structural degradation model. Markov Chain Monte Carlo (MCMC) sampling is employed to calculate the posterior distributions of the stochastic parameters in the structural degradation model. Bayesian updating allows the use of dynamic diagnostic information with prior knowledge for improved prognosis such as risk analysis and remaining useful life (RUL) estimation.

In this chapter, the general prognosis procedure is extended to consider two unique features associated with sensor driven prognosis. One feature is the sensor performance degradation in long-term monitoring. In order to account for this feature, the error term in the structural degradation model is divided into two terms: the measurement error term and the model error term. Stochastic process is used to represent these two terms. The other feature is the massive amount of sensor data that could be generated from on-line structural health monitoring (SHM) system. How to effectively extract key prognosis information out of massive amount of sensor data is of interest. An extreme value theory (EVT) based method is proposed which can reduce the computation demand by 80% while still preserving the key information of sensor data.

5.2 General degradation model

In the proposed general sensor-driven probabilistic health prognosis procedure, a

general structural degradation model with random parameters is defined, in which the error term are divided into two types of errors. Bayesian theorem is applied to update the parameter distributions of the structural degradation model with sensor data. MCMC is implemented to sample from posterior distributions of the random parameters. Risk analysis and RUL estimation can be carried out with specific limit state function and risk acceptance level. The proposed sensor-driven structural health prognosis method can perform updating of multiple random parameters with multiple measurement inputs. A flowchart illustrating the general procedure is shown in Figure 1. In this section, the general structural degradation model is firstly introduced.

5.2.1 General form

The proposed sensor-driven structural health prognosis procedure is based on a stochastic structural degradation model which models the variation of an engineering system over time. In nondestructive testing (NDT) data driven degradation model, a single probabilistic error term is commonly incorporated to account for the overall uncertainty associated with the model and measurements. In the proposed sensor-driven health prognosis procedure, however, this general error term is explicitly divided into two separate terms: measurement error and model error. This approach reflects the fact that sensor performance (in terms of measurement error) generally varies (usually deteriorates) with time, and thus needs to be described with a time-evolving stochastic process. The model error term represents the unknown factors in modeling the system. The stochastic structural degradation model can be expressed as,

$$y(t)=F(t,\alpha,\beta)+\varepsilon_{mdl}(t)+\varepsilon_{msm}(t) \tag{5.1}$$

where *y(t)* is the degradation index which can be directly measured or indirectly

identified from sensor data (e.g., features of fused sensor data), and t denotes the time. $F(t,\alpha,\beta)$ is a function describing the evolution of the system. α is the model parameter vector containing quantities related to system properties, i.e., $\alpha=[\alpha_1, \alpha_2 \ldots \alpha_j]$. Due to the uncertainties commonly associated with the model parameters, they can be described as random variables following pre-specified probability distributions. β is the environmental input vector which includes quantities (e.g. strain) resulting from loading such as temperature, or any other excitations to the system. ε_{mdl} and ε_{msm} represents the model error and measurement error respectively.

5.2.2 Error term modeling

5.2.2.1 Measurement error

Modeling the measurement error should be derived from the characteristics of sensors used for continuous online monitoring system for structural health diagnosis and prognosis. Compared with NDT inspection data based approaches, sensor-driven monitoring and prognosis procedure has the following features (also summarized in Table 5.1): sensor data are continuous, abundant, real-time (or nearly real-time) collected; sensor data with multiple modalities are available. Data analysis in such online monitoring system generally requires automated execution due to huge amount of data stream collected every day. Another feature of sensors in long-term monitoring system is that their performance would vary (usually deteriorate) over the time due to the degradation of the sensors themselves. Uncertainty in sensor data (measurement error) thus needs to be explicitly modeled as an evolving stochastic process. Gebraeel *et al* (2005) studied two types of stochastic processes: Gaussian process and Wiener process. He concluded that the model with Brownian motion assumption for the error term fits the data better. A few researchers have adopted the

Wiener process to model error term in prognosis application. (Doksum and Hoyland 1993; Whitmore 1995; Gebraeel *et al* 2005). Here, considering the sensor degradation, the Wiener process is used as an example to demonstrate the updating procedure. Under this assumption, $\varepsilon_{msm}(t_1)$, $[\varepsilon_{msm}(t_2)\text{-}\varepsilon_{msm}(t_1)]$, …., $[\varepsilon_{msm}(t_i)\text{-}\varepsilon_{msm}(t_{i-1})]$ are independent normal random variables with zero mean, i.e.,

$$[\varepsilon_{msm}(t_i) - \varepsilon_{msm}(t_{i-1})] \propto N(0, \sigma^2_{msm}(t_i - t_{i-1})) \tag{5.2}$$

In certain cases, the sensor exhibits little degradation during monitoring mission, under such cases, the measurement error can simply be treated as following Gaussian process. Under this assumption, $\varepsilon_{msm}(t_1)$, $\varepsilon_{msm}(t_2)$, …., $\varepsilon_{msm}(t_i)$ are independent normal random variables with zero mean, i.e.,

$$\varepsilon_{msm}(t_i) \propto N(0, \sigma^2_{msm}) \tag{5.3}$$

5.2.2.2 Model error

The model error term represents the aggregated influence by various factors because the degradation model never holds exactly in practice. In this study, the model error term is assumed to follow the Gaussian process. For any given time *t*, the model error term $\varepsilon_{mdl}(t_1)$, $\varepsilon_{mdl}(t_2)$, …., $\varepsilon_{mdl}(t_i)$ also follow independent normal distribution as shown in Eqn. (5.4):

$$\varepsilon_{mdl}(t_i) \propto N(0, \sigma^2_{mdl}) \tag{5.4}$$

Independence between the measurement error and model error is assumed.

5.3 Bayesian updating and Markov Chain Monte Carlo simulation

5.3.1 Bayesian updating with implicit degradation model

Without updating using monitoring data, uncertainty in the model parameters may

lead to large variance in the predicted value of the degradation index, which subsequently affects the accuracy of risk analysis and maintenance management. With data related to the damage index from monitoring system, initial model parameter distributions can be updated with measured data thus reducing the uncertainty in the prediction. Bayesian theory is used here for updating the model parameters with sensor data.

5.3.1.1 Updating with sensor degradation considered

Let $Y=[y(t_1), y(t_2) \ldots y(t_k)]$ denote the measurement data. t_i is the time of measurement. From the assumptions for model error and measurement error, we come to the conclusion that $y(t_i)$-$y(t_{i-1})$ follows normal distribution.

$$y(t_i) - y(t_{i-1}) \propto N(F(t_i,\alpha) - F(t_{i-1},\alpha), \sigma_{msm}^2 \cdot (t_i - t_{i-1}) + 2\sigma_{mdl}^2) \tag{5.5}$$

It should be noted that for $y(t_1)$, its distribution is slightly different from Eqn. (5.5) and can be expressed as $N(F(t_1,\alpha), \sigma_{msm}^2 \cdot t_1 + \sigma_{mdl}^2)$. Under the assumption of the Wiener process for measurement error and model error, as well as the independence between measurement error and model error, the covariance between any two different measurement increments equals zero. Also, according to Eqn. (5.4), the measurement increments follow normal distribution. Therefore, it can be concluded that for given values of α, measurement increments, $[y(t_1), y(t_2)-y(t_1), \ldots, y(t_k)-y(t_{k-1})]$ are mutually independent. Therefore, given the values for α, the conditional probability density function (PDF) of $f(Y|\alpha)$ can be expressed as:

$$\begin{aligned} f(Y|\alpha) &= f(y(t_1), y(t_2) - y(t_1), \ldots, y(t_k) - y(t_{k-1})|\alpha) \\ &= f(y(t_1)|\alpha) \cdot \prod_{i=2}^{k} f(y(t_i) - y(t_{i-1})|\alpha) \end{aligned} \tag{5.6}$$

In Eqn. (5.6),

$$f(y(t_1)|\alpha)) = \frac{1}{\sqrt{2\pi\left(t_1\sigma_{msm}^2 + \sigma_{mdl}^2\right)}} \exp(-\frac{(y(t_1) - F(t_1,\alpha))^2}{2(t_1\sigma_{msm}^2 + \sigma_{mdl}^2)})$$

$$\prod_{i=2}^{k} f(y(t_i) - y(t_{i-1})|\alpha) = \frac{\exp(-\sum_{i=2}^{k} \frac{((y(t_i) - y(t_{i-1})) - (F(t_i,\alpha) - F(t_{i-1},\alpha)))^2}{2((t_i - t_{i-1})\sigma_{msm}^2 + 2\sigma_{mdl}^2)})}{\prod_{i=2}^{k} \frac{1}{\sqrt{2\pi((t_i - t_{i-1})\sigma_{msm}^2 + 2\sigma_{mdl}^2)}}}$$

(5.7)

Using the Bayesian theorem, their posterior distribution can be computed using Eqn. (5.8),

$$f(\alpha|Y) = \frac{f(Y|\alpha) \times f(\alpha)}{\int f(Y|\alpha) \times f(\alpha) d\alpha} \tag{5.8}$$

Therefore, it is seen that the posterior distribution for α αcan be updated using monitoring data.

5.3.1.2 Updating without sensor degradation considered

$y(t_i)$ is a normal distribution with its mean value of $F(t_i,\alpha)$ and its variance equal to $(\sigma_{msm}^2+\sigma_{mdl}^2)$. Meanwhile, its distribution is truncated to keep $y(t_i)$ non-negative. The truncated conditional probability density function $f(y(t_i)|\alpha)$ is shown below :

$$f(y(t_i)|\alpha) = \begin{cases} \dfrac{\frac{1}{\sqrt{2\pi\sigma^2}} \exp(-\frac{(y(t_i) - F(t_i,\alpha))^2}{2(\sigma_{msm}^2 + \sigma_{mdl}^2)})}{1 - \Phi(-\frac{F(t_i,\alpha)}{\sqrt{\sigma_{msm}^2 + \sigma_{mdl}^2}})} & \text{for } y(t_i) > 0 \\ 0 & \text{otherwise} \end{cases} \tag{5.9}$$

As for $f(Y|\alpha)$, it is calculated using Eqn. (5.10) below,

$$f(Y|\alpha) = f(y(t_1), y(t_2), ..., y(t_k)|\alpha) \tag{5.10}$$

After $f(Y|\alpha)$ is obtained, $f(\alpha|Y)$ can be calculated using Eqn. (5.8).

5.3.2 Markov Chain Monte Carlo simulation

$F(t,\alpha,\beta)$ may have a large number of random system parameters that would make computing $f(\alpha|Y)$ difficult to do because of multi-dimensional integration being involved. For higher dimensions, analytic evaluation of this posterior distribution is infeasible, while numerical evaluation as an alternative approach might be equally difficult and inaccurate in greater dimension (Gilks *et al* 1996). Generally speaking, if the dimension exceeds three, an alternative method would be used instead of numerical integration. Furthermore, occasionally, there is even no explicit form for the degradation model. Under such situation, closed form expression for the posterior distribution would not be available. In order to overcome these two problems, MCMC simulation, which is suitable for simulating high dimension PDF, is selected here as the alternative approach to calculate the posterior distribution.

The MCMC method draws samples from a pre-specified distribution by running a constructed Markov Chain that will converge after certain number of loops. The Metropolis-Hastings algorithm (Metropolis *et al* 1953; Hastings 1970) is employed here for sample drawing from the posterior distribution, which is described below in details (Gilks *et al* 1996). Figure 5.2 illustrates a single loop of the Metropolis-Hastings Algorithm.

1. Initializing the stochastic parameters, i.e., let $\alpha^{0} = [x^{0}]$. Set $t = 0$. At any time step $t = i$, the value of α^{i} is expressed as $[x^{i}]$.

2. Propose a probability density $Q(\alpha', \alpha^{i})$. Using this density function, a new state $\alpha' = [x']$ can be generated out of the current state $\alpha^{i} = [x^{i}]$.

3. Calculate J value with the measurements Y as below,

$$J = \min(1, \frac{f(\alpha'|Y) \cdot Q(\alpha^i|\alpha')}{f(\alpha^i|Y) \cdot Q(\alpha'|\alpha^i)})$$

4. Draw U from a uniform distribution $U[0,1]$. If $U < J$, set $\alpha^{i+1} = \alpha'$; otherwise, let $\alpha^{i+1} = \alpha^i$.

A new sample α^{i+1} is now available based on the previous sample α^i. Repeat Step 1 to Step 4 for a pre-specified number of cycles.

In the above procedure, a random walk sampler is adopted, and the proposal function is thus symmetric, i.e.,

$$Q(\alpha'|\alpha^i) = Q(\alpha^i|\alpha')$$

J can be simplified into Eqn. (5.11),

$$J = \min(1, \frac{f(\alpha'|Y)}{f(\alpha^i|Y)}) \tag{5.11}$$

For the MCMC calculation, the initial samples may not follow the specified distribution. Yet they will gradually converge to the specified distribution. Therefore, the criterion for the convergence of the samples has to be defined before-hand. The samples after convergence are gathered to represent the posterior distributions. An index for judging the convergence as proposed by Gelman and Shirley (2010) is adopted in this study. A total of m parallel sequences each with a length of n samples are first generated using the given algorithm. The j-th sample in the i-th sequence is labeled as Ψ_{ij}. The index can then be expressed as,

$$\sqrt{\hat{R}} = \sqrt{\frac{Var(\hat{\psi})}{W}} \tag{5.12}$$

In Eqn. (5.13),

$$Var\left(\hat{\psi}\right)=\frac{n-1}{n}W+\frac{1}{n}B;W=\frac{1}{m}\sum_{i=1}^{m}S_i^2 \tag{5.13}$$

$$B=\frac{n}{m-1}\sum_{i=1}^{m}\left(\bar{\psi}_i-\bar{\psi}_{..}\right)^2;\bar{\psi}_i=\frac{1}{n}\sum_{i=1}^{m}\psi_{ij};\bar{\psi}_{..}=\frac{1}{m}\sum_{i=1}^{m}\bar{\psi}_i$$

$$S_i^2=\frac{1}{n-1}\sum_{j=1}^{n}\left(\psi_{ij}-\bar{\psi}_i\right)^2$$

If $\sqrt{\hat{R}}$ reaches a value close to one, the chain is considered to converge. Usually, more than 10 chains are needed to calculate the index. In Gelman and Shirley's study (2010), a value of 1.2 is recommended as the threshold for the convergence. In another word, the samples are considered to have converged once the index falls below 1.2.

After the samples representing the posterior distribution are generated, the failure probability as well as RUL of the system can be determined.

A template code of the MCMC sampling is provided in Appendix C.

5.3.3 Risk analysis and remaining useful life updating

After updating the probability distribution of the random parameters in the degradation model, the estimated degradation index can be recalculated from the updated model. With many sensor data being collected at almost the same time, the estimated degradation index at any time instant follows a statistical distribution due to the uncertainty associated with the system and measured data.

In order to estimate the RUL of the concerned system, two terms need to be defined: limit state function and risk acceptance level. Usually, the limit state function is given as Eqn. (5.14), (Shinozuka 1983)

$$g = y_{cr} - F\left(t, \alpha, \beta\right) \leq 0 \tag{5.14}$$

Due to the uncertainty in the degradation model, $F(t,\alpha,\beta)$ follows a distribution at any time instant t, when the updating is done. From Eqn. (5.14), the probability of failure can be calculated as,

$$P_f(t) = P[y_{cr} - F\left(t, \alpha, \beta\right) \leq 0] \tag{5.15}$$

Risk acceptance level is defined as the critical failure probability value below which a system is considered safe and beyond which the system is considered unsafe and thus action needs to be taken for maintaining the system. Suppose a risk-acceptance level of R% is specified to compute the RUL using Eqn. (5.16), RUL is the value of t at which

$$P_f\left(t\right) = R\% \tag{5.16}$$

An illustration of how RUL estimation can be performed is given in Figure 5.3. In this figure, the horizontal axis denotes the in-service time. In-service time is defined as the interval between the time the structure first opened to service and current time when structural health prognosis is performed. Service life is defined as the total life of the concerned structure from its first opening to service till its failure. Given the definition, there is the relationship that service life is the sum of in service time and RUL. Different combination of y_{cr} and R% might yield different RUL estimations such as next inspection time. Values for y_{cr} and R% must be determined from code specifications or empirical data. Maintenance operation can be scheduled based on such RUL information.

5.4 EVT-based structural prognosis method

The above introduced prognosis procedure utilize a single set of sensor data for structural prognosis. In real case of structural monitoring project, hundreds sets of sensor data can be obtained within a short time during which structural condition presumably would not change under normal operating conditions. In such condition, for each set of sensor data, a corresponding RUL value can be determined through the prognosis procedure. Therefore, hundreds of model updating and RUL estimation have to be carried out. Subsequently, distribution fitting can be applied to determine a probabilistic distribution for the RULs from which the quantile values can be computed. However, this approach is computationally very demanding because of the Bayesian updating process and MCMC sampling involved. Since unexpected failure might lead to catastrophic consequence, it is critical to know the small quantiles of the estimated RULs. Considering the fact that decision makers are often more interested in the small quantile or extreme values of the estimated RULs, it is not necessary to obtain the full probabilistic distribution of the RULs as a random variable. Therefore, estimation of the tail parts or extreme values of the RUL distributions based on a selected and thus reduced sensor data set would be of interest to SHM applications.

In this study, the EVT is introduced to reduce computation demand without losing much accuracy. EVT makes statistical inference about the upper tail of a random variable without the need of knowing its true distribution. EVT allows only a small percentage of total available sensor data to be actually used for estimating the tail quantile of the RUL. Estimators from EVT are often used to predict high quantile

values for the distribution of prognosis results. A variety of estimators have been developed for EVT, such as the Hill estimator (Hill 1975), PWM estimator (Hosking and Wallis 1987), and moment estimator (Dekkers *et al* 1989), etc. Moment estimator is selected here for its ability to discern a light tail distribution more efficiently than the Hill estimator (Resnick 1997) since in many applications such as fatigue life prognosis the distribution of the RULs is usually bounded and not heavily tailed.

As for the proposed EVT-based prognosis method using moment estimator in this study, only k out of n measurements (normally $k << n$) are used for model updating and RUL estimation by implementing the moment estimator. The k largest measurements selected from the full sensor data set are used as the input to the structural health prognosis. The k RUL values are computed accordingly using these largest measurements. If it can be proved that these k RUL values represent the smallest values among all RUL values, moment estimator can be applied on the set of k RUL values to estimate the small quantile values of the underlying RUL distribution. Information such as small quantile estimates for the RUL can be obtained accordingly. However, the computational demand for the EVT-based structural health prognosis can be cut substantially to nearly k/n of the original computing time (normally $k << n$). A flowchart for this method is given in Figure 5.4.

5.4.1 Moment estimator method for univariate EVT

Moment estimator method for univariate EVT is used to approximate the high quantiles for sample distributions using only a small portion of the available samples. A high quantile X_p is defined as $P(x>X_p) = p$ where p approaches zero. Assume that $X_n \geq X_{n-1} \geq \ldots \geq X_{n-(k-1)} \geq X_{(n-k)} \ldots \geq X_1$ are the order statistics of the total n data samples

available. Moment estimator method uses the largest m samples (i.e., X_n , $X_{n-1,}$ …, X_{n-m+1}) to approximate X_p ($n>>m$). According to Moment estimator method, the quantile estimator $\hat{X}_p(k)$ is defined in Eqn. (5.17) below,

$$\hat{X}_p(k) = X_{n-k} + \hat{a}(k) \cdot [\frac{(\frac{k}{np})^{\hat{\gamma}(k)} - 1}{\hat{\gamma}_e}] \tag{5.17}$$

Where $k = 1, 2, \ldots, m$. X_{n-k} is the *(n-k)th* order statistic of n samples. $\hat{a}(k)$ is the moment estimator for scale function which can be calculated as Eqn. (5.18). $\hat{\gamma}(k)$ is the moment estimator for extreme value index γ, which can be estimated using Eqn. (5.19). $\hat{\gamma}_e$ is the estimated value for γ derived from estimator $\hat{\gamma}(k)$.

$$\hat{a}(k) = \frac{1}{2} X_{n-k} \cdot M_1(k) \cdot [1 - \frac{(M_1(k))^2}{M_2(k)}]^{-1} \tag{5.18}$$

$$\hat{\gamma}(k) = M_1(k) + 1 - \frac{1}{2}[1 - \frac{(M_1(k))^2}{M_2(k)}]^{-1} \tag{5.19}$$

In Eqns. (5.17) and (5.19), $M_j(k)$ is calculated as Eqn. (5.20),

$$M_j(k) = \frac{1}{k} \sum_{i=0}^{k-1} [\log(X_{n-i}) - \log(X_{n-k})]^j \tag{5.20}$$

In which X_{n-i} is the *(n-i)th* order statistic of n samples, and j = 1, 2.

To determine $\hat{\gamma}_e$, a common approach is to calculate $\hat{\gamma}(k)$ for $k = 1, 2, \ldots m$. Then, plot $\hat{\gamma}(k)$ against k, and the average of $\hat{\gamma}(k)$ within a certain range (usually for sufficiently large k values) is $\hat{\gamma}_e$. The value of $\hat{\gamma}_e$ can be used to assess whether the sample data is heavy tailed or not. For example, the distribution of the sample data is heavy tailed if $\hat{\gamma}_e$ is positive, and vice versa. Hill estimator is preferred in estimating

the high quantile value.

After $\hat{\gamma}_e$ is obtained, a similar process can be applied to determine X_p by first plotting $\hat{X}_p(k)$ against k, and then calculating the average of $\hat{X}_p(k)$ within a certain range that shows less fluctuation in $\hat{X}_p(k)$ (usually when k is sufficiently large).

The above moment estimator method uses a relatively small portion ($m << n$) of the sample data that has larger values. To estimate low quantiles that may be of interest in certain applications, only slight adjustment can be made to the above process. For instance, in the RUL quantile estimation, low quantile values are desired. The above procedure can be applied to the reciprocal of the RULs.

Danielson (2001) suggested that the optimal value for the sample size m is $O(n^{\frac{-2\rho_{sd}}{-2\rho_{sd}+1}})$ in applying the above moment estimator. ρ_{sd} is the second order index for the EVT theorem and n is the original total sample size. For example, for a total sample size of n = 500,100 samples (i.e. m = 100) may be adequate to estimate the high quantile value, thus using only 20% samples.

5.4.2 First-order stochastic dominance for posterior distribution

The EVT method is applied to the calculation of RULs. Therefore, the lower portion of RUL needs to be calculated from damage index values using the Bayesian updating, which is the most demanding part computation-wise in the EVT based prognosis process. If monotonicity condition between damage index and prognosis results such as RUL values is satisfied (monotonically increasing or decreasing), only m out of n damage index values would be used to calculate the smallest RUL values; thus it lowers the computation load by 100*(n-m)/n percentage.

To show the monotonicity condition, the first-order stochastic dominance of the posterior distribution $f(\alpha|Y)$ after Bayesian updating (see Eqn. (5.8)) is first examined. First-order stochastic dominance is defined as follows (Cox, 2002): for two random variables X and Y, X first order stochastic dominance Y if and only if $F_X(a) \leq F_Y(a)$ for all a. ($F(a)$ is the cumulative probability density function for a). Milgrom (1981) proved that the strict monotone likelihood ratio property (MLRP) of the likelihood function $f(Y|\alpha)$ is both a necessary and sufficient condition for the first-order stochastic dominance of the posterior distributions in Bayesian updating. Therefore, in Eqn. (5.8), if the likelihood function $f(Y|\alpha)$ satisfies the strict MLRP (as shown below), the first-order stochastic dominance for the posterior distribution $f(\alpha|Y)$ can be assured.

According to Milgrom (1981), the density function $f(\bullet|\theta)$ has the strict MLRP if Eqn. (5.21) below holds for every $x > z$ and $\tilde{\theta} > \hat{\theta}$,

$$f\left(x \mid \tilde{\theta}\right) f\left(z \mid \hat{\theta}\right) - f\left(x \mid \hat{\theta}\right) f\left(z \mid \tilde{\theta}\right) > 0 \qquad (5.21)$$

Assume a total of n_{ms} measurement segments are carried out and each measurement segment contains n_{sg} data samples. For the EVT-based prognosis method, the measured data within each measurement segments are ranked and regroup the measured data into n_{sg} new sets by rank statistics (e.g., all largest data values will be regrouped into one set, etc.). Two such sets y_1 and y_2 are chosen: $y_1 = [y_{11}, y_{12}, \ldots, y_{1n\_ms}]$ and $y_2 = [y_{21}, y_{22}, \ldots y_{2n\_ms}]$, where $y_{1i} > y_{2i}$. The general error term $\varepsilon(N) = \varepsilon_{mdl}(N) + \varepsilon_{msm}(N)$ is assumed to follow the Gaussian process and always follow the same normal distribution of $N \sim (0, \sigma^2)$. Two values α_1 and α_2 (assuming $\alpha_1 > \alpha_2$) are randomly sampled from the stochastic parameter α. The joint conditional probability

$f(y_j|\alpha_i)$ (j = 1, 2; and i = 1, 2) of y_1 and y_2 follows normal distribution of N ~ ($F(\alpha_i)$, σ^2) from Eqn. (5.1), which can be expressed as,

$$f\left(y_j \mid \alpha_i\right) = \frac{1}{\sqrt{2\pi}\sigma} \exp\{-\sum_{k=1}^{n_{ms}} \frac{[y_{jk} - F(\alpha_i)]^2}{2\sigma^2}\} \tag{5.22}$$

where i = 1, 2 and j = 1, 2; $k = 1 \ldots n_{ms}$. Eqn. (5.23) is derived from Eqn. (5.22) as,

$$\frac{f\left(y_j \mid \alpha_1\right)}{f\left(y_j \mid \alpha_2\right)} = \exp\{\frac{\sum_{k=1}^{n_{ms}} [F(\alpha_1) - F(\alpha_2)] \cdot [2y_{jk} - F(\alpha_1) - F(\alpha_2)]}{2\sigma^2}\} \tag{5.23}$$

where j = 1, 2 and k = 1, 2, …, n_{ms}. It can be observed that Eqn. (5.23) is monotonically increasing with y_j as long as $F(\alpha_1) > F(\alpha_2)$. Strict MLRP is thus demonstrated for the likelihood function of $f(y_j|\alpha_i)$ and the first-order stochastic dominance of the posterior distribution $f(\alpha|Y)$ in Eqn. (5.8) is verified.

Because of the first-order stochastic dominance of the posterior distribution if $F(t,\alpha,\beta)$ is also monotonic with α, it can be concluded that monotonicity between measurements y and estimated RUL holds given the same limit state condition and acceptance level. For a variety of degradation processes, the monotonicity between the measured damage index data y and model parameter α exists. For example, the fatigue crack length in the Paris Law-based fatigue degradation model (Paris et al. 1961) monotonically increases with the two parameters C and m. For steel rebar corrosion problem, the depth for the hemispherical pit also monotonically increases with the pitting current (Harlow and Wei 2001). For application in these fields, EVT-based prognosis method is applicable.

In summary, three prerequisite conditions have to be satisfied in order to use the proposed EVT-based prognosis method: (1) A stochastic degradation model with a

measurable damage index as the independent variable is established; (2) A limit state function is defined in terms of the damage index; (3) A monotonicity condition between the damage index value and RUL exists. Once these three conditions are satisfied, the proposed EVT based prognosis method can be used for other limit states than those described in the two case studies next. A real structure is a system comprised of many components and its failure might be caused by one of the system's components. Therefore, the system's failure probability and RUL can be easily determined using systems theory once the failure probability and RUL of each individual component's limit state is known. Two important examples on fatigue cracking and rebar pitting corrosion are given in this paper to illustrate the implementation of this method. The RUL in this paper refers to the component rather than the system.

5.5 Case study

5.5.1 Fatigue prognosis of Yellow Mill Pond bridge-general procedure

The Yellow Mill Pond Bridge is located on the Connecticut Turn pike I- 95 in the City of Bridgeport, Connecticut. The bridge was first opened to traffic in January 1958. This bridge consists of 28 simple-span cover-plated steel I-girders crossing the Yellow Mill Pond Channel. The dimensions for the beam are given as follows: Flange Width = 0.4191 m; Flange Thickness = 0.0320 m; Cover Plate Thickness = 0.0318 m; Web Thickness = 0.0190 m; Weld Leg = 0.0160 m.

Fatigue cracking was first observed at the Yellow Mill Pond Bridge in 1970 (Fisher *et al* 1981). Fatigue crack growth resulted in complete fracture of a tension flange in one of the girders. Several inspections were made between 1970 and 1979. In 1976, 1977,

1979, cover plates on the Yellow Mill Pond Bridge were inspected for fatigue cracks. Using ultrasonic NDE method, Fatigue cracks were found in the vicinity of the cover plate welds. A sketch of the cover plate and the crack location is presented in Figure 5.5.

The stress range due to the traffic was recorded in 1971, 1973 and 1976. Maximum stress ranges as high as 72.4 MPa (10.5 ksi) were measured at the end weld of the cover plates (Fisher *et al* 1981). Since this bridge is well studied by many researchers (Fisher *et al* 1981; Yazdani and Albrecht 1987; Zhao and Haldar 1994) and as such verified fatigue data are readily available, the fatigue data from this bridge is used in this research as an example to illustrate the application of the structural health prognosis procedure. A specified procedure of sensor driven fatigue prognosis for the Yellow Mill Pond bridge cover plate is shown in Figure 5.6.

Initial crack length

In his paper, Fisher (1984) stated that for most welding details of steel bridges, initial cracks usually would exist at the very beginning. Therefore, they made an assumption that the initial crack starts to propagate from the first loading cycle. In this research, it is also assumed that initial crack exists before loading starts.

For thick cover plate, Yazdani and Albrecht (1987) used a lognormal distribution with a mean value of 0.0508 cm and coefficient of variation (COV) equal to 0.5 for initial crack length. These values are also adopted here for the health prognosis of the cover plate fatigue details on the Yellow Mill Pond Bridge.

Critical crack length

The critical crack size is defined as the crack size above which the fatigue limit state

(i.e., failure) is assumed to occur. In practical applications, it can be determined by either fracture mechanics or a serviceability criterion (Zhao and Haldar 1996).

To avoid unexpected failure, people usually take the relatively conservative value which is from serviceability criterion as the critical crack size. Zhao and Haldar (1996) suggested that the width or the thickness of a fatigue detail can be used as the critical crack size.

In this study, the serviceability criterion is adopted to determine the critical crack size. The flange thickness is taken as the critical crack size, i.e., a_{cr} = flange thickness = 3.20 cm.

Correction factor

For cover plate fatigue, the correction factors are calculated as (Fisher *et al* 1979),

$$G_e = \frac{1}{E(k)}$$

$$G_s = 1.211 - 0.186\sqrt{a/b}$$

$G_w = 1$ (for AASHTO fatigue categories E and E')

$$G_g = \frac{\text{SCF}}{1+6.789\left(\frac{a}{T_F}\right)^{0.4348}} \tag{5.24}$$

$$\text{SCF} = -3.539 \cdot \ln\left(\frac{Z}{T_F}\right) + 1.981 \cdot \left(\frac{T_{cp}}{T_F}\right) + 5.3798 \tag{5.25}$$

where a is the crack length along miner axis (i.e., in the direction of crack depth), b is the crack length along major axis (usually crack's surface length). T_{cp} is the cover-plate thickness, T_F is the flange thickness. Z is the weld leg size. $E(k)$ is the complete elliptical integral of the second kind with k defined as $k^2 = (c^2-a^2)/c^2$.

Material Constants

Usually, among the two materials constants, parameter *C* is assumed to follow a lognormal distribution, while crack growth exponent constant *m* is treated as deterministic. The crack growth exponent *m* = 3 is proposed out of basic crack growth rate data from structural steels as well as test data on welded members (Yazdani and Albrecht 1987). Parameter *C* is found to be with a mean value of 3.92×10^{-12} and COV of 0.63 (*m* for crack size and $MPa\sqrt{m}$ for K).

Crack measurements

For fatigue cracks associated with the cover plate detail, the crack is assumed to be semi-elliptical surface crack. In November 1973, the east ends of Beams 2 and 3 of the eastbound roadway of Span 10 were inspected; fatigue cracks were discovered (Fisher *et al* 1981). In Beam 2, a crack with a depth of 0.95 cm was identified. In November 1976, during a brief inspection of Span 13, four large cracks were observed. These cracks are about 1.27 cm deep. Crack lengths measurements are summarized in Table 5.2. For illustration purpose, it is assumed here that these measurements are from the same crack measuring instrument so that the dependence of the instrument degradation can be retained. Using these crack information, the RUL of this specific cover-plate detail can be estimated.

Here, standard deviation for the model error is assumed to be 1.5×10^{-4} at the first measurement moment similar to the number used by Robinson (2000). Ultrasonic inspection along with other NDT techniques was used to detect the crack size on Yellow Mill Pond Bridge (Fisher *et al* 1981). At present days, one commonly used crack size measurement technique is the ultrasonic phased array sensors. For example,

measured crack length within a 0.2 mm error, which is on the order of $1x10^{-4}$, can be achieved using ultrasonic phased array sensor probes (Satyanarayan *et al* 2007). Therefore, we assume that σ_{msm} is also $1x10^{-4}$. It is anticipated that as ultrasonic sensing technique advances, in-situ ultrasonic phased array sensor can achieve this level of accuracy in the future.

Total fatigue load cycle

The average daily truck traffic (ADTT) determines the load history of a bridge. It was reported by Fisher *et al* (1981) that the ADTT on Span 10 has increased from 3,000 to 6,700 for the years 1958-1975. The ADTT estimated from weigh-in-motion data collected by Connecticut Department of Transportation is 20,692 in 2009. To simplify, the following traffic flow model is adopted,

$$ADTT(i+1) = ADTT(i) \times (1+r) \tag{5.26}$$

The annual traffic growth rate is set to be 3.38%. Eqn. (5.26) yields the traffic loading volume as: In 1973, total number of passed trucks is $2.65x10^{7}$; In 1977, total number of passed trucks is $3.35x10^{7}$. One loading cycle for each truck passage is adopted here.

Stress range history

In the July 1971 study, electrical-resistance strain gages were installed on the bridges (Fisher *et al* 1981). They were placed at two locations on the interior beams: One at the mid-span, the other at a location about 102 mm away from the end of the primary cover plate. All of them were under the web on either the flange or primary cover plate. Also, other measurements have been done to obtain the strain history in 1973 to 1974, and in June 1976. The measurements for the highest stressed girder yielded a Miner stress range of 13.1 MPa (Fisher, 1984). In this study, since $m = 3$ is adopted,

the equivalent constant amplitude stress range is equal to the Miner stress range. According to fatigue theory, the earliest cracks usually occur at locations with the most severe condition. They usually first initiate at the details where have the largest effective stress range applies. The equivalent constant amplitude stress range is set to be 13.1 MPa in this study to estimate the fatigue life.

Model updating

Bayesian updating was carried out given the two measurements in 1973 and 1976. The MCMC method was applied to sample from joint posterior distributions of random parameters C and a_0. 100,000 samples were generated for each updating. The samples drawn for a_0 and C are shown in Figure 5.7. The posterior distribution for these two parameters has changed from the prior distribution. Comparison between prior and posterior distribution for a_0 and C can be seen in Figure 5.8. For the posterior distribution, the mean values for both a_0 and C have increased. This means the initial mean values for the parameters are smaller than the true values in this case. Meanwhile, the coefficients of variance for both have decreased. This is attributed to the new information flown in which reduces the uncertainty in the model parameters. Parameter comparison is provided in Table 5.3. With the samples of the random parameters, the fatigue crack growth curve is calculated and shown in Figure 5.9a. Also, the fatigue crack growth curve with initial parameters distributions is plotted as Figure 5.9b. It is seen that the updated crack growth curve fits the measurements much better than the initial crack growth curve. Meanwhile, the distribution for the estimated crack length after updating becomes narrower than the one without updating, as shown in Figure 5.9.

Risk analysis and fatigue life estimation

In the AASHTO *S-N* approach, the allowable *S-N* curve is set two standard deviations from the mean. For normal distribution, the cumulative density function of (μ-2σ) equals 2.3%. In this study 2.3% is adopted as the risk acceptance level for the bridge detail of cover plate following the research by Yazdani and Albrecht (1987). It is expected that inspections are required at the considered fatigue detail location whenever the failure probability reaches 2.3%. Maintenance action is also planned at that time based on the inspection results. After generating the samples by MCMC simulation, failure probability curve can be calculated. Next inspection time estimated from the failure probability curve is given in Table 5.4.

Given the risk acceptance level at 2.3%, the estimated service life before next inspection is 26.5 years from the updated model while the estimated service life without updating is 22.1 years. This means the initial degradation model without updating yields a conservative prediction. As an example, Figure 5.10 plots the distribution of fatigue crack length estimated after 30 million load cycles. Results from both the initial model and updated models are given in the figure. It is seen in this figure that the estimated crack length distribution from the initial model has a quite heavy tail on the right side. But for the updated crack length distribution, it is not heavy tailed. Since the risk acceptance is as small as 2.3%, given the critical crack length, the resulting RUL estimation is determined primarily based on the right-side tail of the crack length distribution. This explains why the estimated RUL from the initial model would be smaller than that from the updated model even though the mean value of crack length distribution from the initial model is smaller than that

from updated model.

In real application, for a specific component, the true parameter values might be in the tail of the prior distribution. If prediction is still made based on the initial distribution, this might lead to unexpected failure, or more frequent inspection because of false alarm. Here in this example, it leads to a more frequent inspection schedule than the result with updated model, and thus requires additional resources. Therefore, updating of the model with new information from sensing system plays an important role in better prediction of the degradation.

During long term structural monitoring, sensor itself might degrade in performance. For example, certain types of sensors such as piezoelectric material based ultrasonic guided wave sensors and strain gages exhibit data quality degradation as sensors age and deteriorate in performance. In the proposed sensor-driven prognosis procedure, the example used to illustrate the concept deals with fatigue crack length measurement, which are often done using ultrasonic guided wave sensors. This is also verified in others' research, e.g., Cobb et al (2009) mentioned that sensor degradation is one among the factors causing the variance in sensor data. Therefore, in the proposed procedure, sensor degradation is modeled with sensor data quality deterioration in terms of measurement error variance. Besides the initial assumption of $\sigma_{msm} = 1x10^{-4}$, another measurement variance value: $\sigma_{msm} = 2x10^{-4}$ is considered for the stochastic process of measurement error.

The results from the two σ_{msm} values are compared in Figure 5.10 and Figure 5.11. In Figure 5.10, given different σ_{msm} values, the PDFs for estimated crack length at Load Cycle $N = 3x10^{7}$ are plotted. In Figure 5.11, failure probability curves from different

setup are plotted. It is seen in Figure 5.10 that the updated crack length distributions have different kurtosis. The smaller the σ_{msm} is, the more concentrated the updated PDF becomes. This is because σ_{msm} represents the uncertainty in measurements. σ_{msm} of smaller value means that less uncertainty exists in measurements, thus less uncertainty would transfer into the updated RULs from measurements. In Figure 5.11, we can see that $\sigma_{msm} = 2x10^{-4}$ leads to a more conservative estimated RUL than $\sigma_{msm} = 1x10^{-4}$. The updated service life for $\sigma_{msm} = 1x10^{4}$ is 27.4 Years while the updated service life for $\sigma_{msm} = 2x10^{-4}$ is 26.5 Years, as shown in Figure 5.11. The results show the effect of sensor performance degradation and the importance of its proper modeling.

5.5.2 Fatigue prognosis of Yellow Mill Pond bridge- EVT method

The cover plate fatigue problem is still taken as the example to illustrate the EVT method in this section. Due to lack of continuous sensor data (largely because technology was not available then) for fatigue crack length and availability of only limited number of data, the crack depth data are numerically simulated using inspection data as reference. For the sake of EVT based prognosis, it is assumed that during the first measurement segment in 1973, the true crack depth is 9.7 mm. The measurement error is assumed to follow stationary Gaussian process with zero mean and standard deviation of 2. 500 sensor data of the crack depth were simulated from normal distribution of N(9.7, 4). Also, the histogram of the crack depth data is plotted in Figure 5.12. The model error term is assumed to be zero here for simplicity.

Bayesian updating of the fatigue degradation model and prognosis are to be carried out based on the 500 sensor data. For EVT based method, the largest 100 sensor data

are used for updating the degradation model which yields 100 RULs correspondingly. Updating is implemented for each measured data. For each updating, 100,000 samples are generated for MCMC simulation. RUL values are then estimated from the updated degradation model. According to the monotonicity, these 100 RUL values are the smallest among total 500 RUL values. Next, the small quantile estimation (e.g., 1%) can be calculated using the 100 smallest RUL values. By doing so, the total computation time can be reduced by 80%. The crack depth data and its corresponding estimated RULs is plot in Figure 5.13.

$1/RUL_i$ is used to implement the EVT estimators following Eqns. (5.17) to (5.20). First, the extreme value index γ is estimated, as shown in Figure 5.14. $\hat{\gamma}_e$ (the estimated value of γ) is calculated to be -0.3234 as shown in Figure 5.14a. The negative value here implies that the distribution for the reciprocals of RULs is not heavy tailed. It is bounded on the right side. The selection of quantile in real application needs to be justified based on either structural failure criteria or serviceability limit states. Here, several quantile values estimated from moment estimators are presented along with those from distribution fitting. For example, by substituting the 100 RULs into Eqn. (5.17) and letting $p = 0.005$, this quantile $X_{0.005}$ is estimated to be 2.57×10^{-8}, as shown in Figure 5.14b. The corresponding RUL value is thus equal to 3.88×10^{7}. Also, several other small quantiles are calculated using the moment estimator, as listed in Table 5.5.

For comparison purpose, distribution fitting method is also implemented. All the 500 RULs are calculated using the given 500 sensor data. Then, distribution fitting was performed using the 500 RUL values. Statistical regression analysis shows that as

distribution with left boundary, log-logistic distribution provides a good fit to the RUL data. The PDF of the log-logistic distribution is given as Eqn. (5.27). Parameters for the fitted log-logistic distribution have the following values: s = 5.8241, l = 1.8884×10^{7}, $\eta = 3.1321\times10^{7}$.

$$f(x)=\frac{s}{l}\left(\frac{x-\eta}{l}\right)^{s-1}\left(1+\left(\frac{x-\eta}{l}\right)^{s}\right)^{-2} \tag{5.27}$$

Quantile estimations from the two different approaches are given in Table 5.5. All estimations for the same quantile values have small difference (less than 3% for this case study). The cumulative distribution curve for the fitted log-logistic distribution as well as estimated quantile values from moment estimator are plot in Figure 5.15. It is observed that all the quantile values are very close to each other. Therefore, it can be concluded that the proposed EVT-based prognosis method provides a good estimation while reducing the computation demand by 80%.

5.6 Conclusions

This chapter presents a sensor-driven structural health prognosis procedure in which sensor performance variation is explicitly modeled in the structural degradation model. By modeling sensor performance using stochastic process, uncertainty associated with sensor performance variation over time can be characterized and thus better decision making can be made in the prognosis procedure. The prognosis procedure is capable of using sensor data of multiple modalities to update multiple random parameters in the stochastic structural degradation model. Application of this procedure to fatigue damage found in the Yellow Mill Pond Bridge is used to illustrate the procedure.

Because of their different characteristics (especially over the time), the error term in the stochastic degradation model is divided into two stochastic error terms: sensor measurement error and model error. Proper modeling of the sensor measurement error is crucial to characterize the impact of sensor performance variation (usually deterioration) over time. From the parametric study, it is observed that sensor degradation rate does have an impact on the prognosis result. In the fatigue application example, different values of the stochastic model parameters for the sensor measurement error process alter the estimated crack length distribution as well as the predicted RUL of the fatigue detail. Long-term experimental data to support the sensor performance degradation model is thus needed.

The proposed sensor-driven structural health prognosis procedure has the potential for automated execution when implemented in modern continuous monitoring system. Such system generates huge amount of sensor data that have not been well utilized. However, these large amounts of sensor data can be used in the proposed procedure to provide additional dimension information about the effect of sensor performance variation for decision making.

The EVT-based structural health prognosis method is also presented with the aim of reducing sensor data transmission and computing demand from prognosis. In order to do this, moment estimator from EVT is used to estimate the quantile values for the RUL of the monitored structures.

One advantage of the EVT-based prognosis method is that only a small fraction (usually < 20%) of the full sensor data set are actually used in Bayesian updating and RUL calculation. This is very appealing because the Bayesian updating is

computationally demanding and thus time consuming. For example, in the example of fatigue prognosis, fatigue crack growth model usually takes an implicit form which leads to iterative computation for crack depth. Therefore, the EVT-based prognosis method could save the computation time and make the prognosis more efficient without sacrificing much accuracy.

The EVT-based prognosis method requires the condition of monotonicity between the damage index and RUL. In this study, error term is assumed as Gaussian process. For likelihood functions following normal distribution, the monotonicity condition is proven for the fatigue crack growth model.

Table 5.1. Comparison of sensor-driven and NDT data-driven structural health prognosis

	Sensor-driven	NDT data driven
Data collection	Continuous, or on-demand (e.g., after natural hazard)	Periodic
Dataset for updating	Huge amount of sensor data that are continuously collected	Very limited
Decision variable	Uncertainty factors are better characterized. (e.g., error is derived from field measured data, and modeled as stochastic process); More uncertainty factors can be incorporated (e.g., temperature, sensor performance, etc.), which offer additional dimension in decision making,	Deterministic (error in measurement and interpretation is based on lab calibration test, not based on real field measurement)
Major factor affecting its accuracy	Limitation of sensor specification (this is fixable as technology evolves)	Technician's skill and experience (too costly to fix human error (through more training and practice) and may never be possible)
Location with difficult access	Yes	No
Autonomous Execution	Yes	No

Table 5.2. Fatigue crack data from NDT at Yellow Mill Pond Bridge

Years	Crack depth measured (cm)
November, 1973	0.95
November, 1976	1.27

Table 5.3. Parameter comparison between prior and posterior distribution of a_0 and C

	a_0 (cm)		C ((m/cycle)·(N/m$^{-3/2}$)^3)	
	Mean	COV	Mean	COV
Prior	0.0508	0.5000	3.92×10^{-12}	0.6300
Posterior	0.1403	0.1953	6.43×10^{-12}	0.0518

Table 5.4. RUL predicted for the Yellow Mill Pond Bridge based on cover plate fatigue detail in 1976

2.3% failure	Initial (1958)	Updated (1976)
Total Service Life (Years)	22.1	26.5
RUL (Years) after 1976	4.1	8.5

Table 5.5. Comparison of estimated fatigue RUL values from moment estimator and distribution fitting

Quantile	0.002	0.005	0.01	0.02	0.05
RUL from Moment Estimator (load cycles 1×10^7)	3.880	3.944	4.010	4.094	4.248
RUL from distribution fitting (load cycles1×10^7)	3.770	3.880	3.980	4.093	4.263
Difference Ratio	2.8%	1.6%	0.7%	0.0%	-0.4%

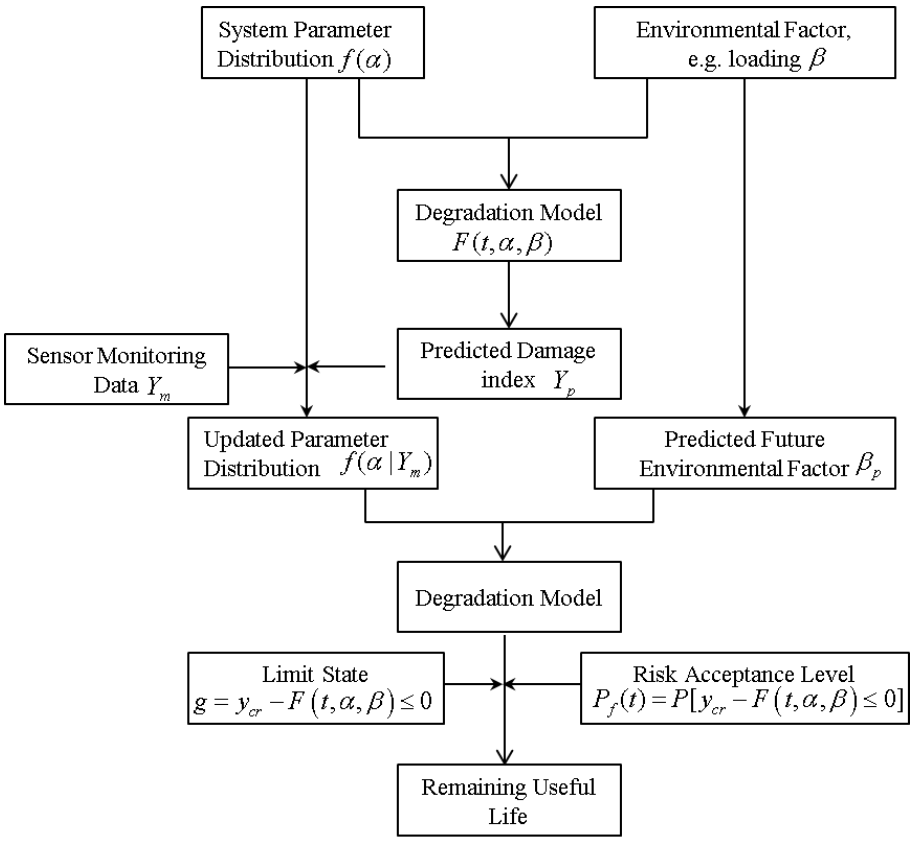

Figure 5.1. Sensor driven structural prognosis procedure

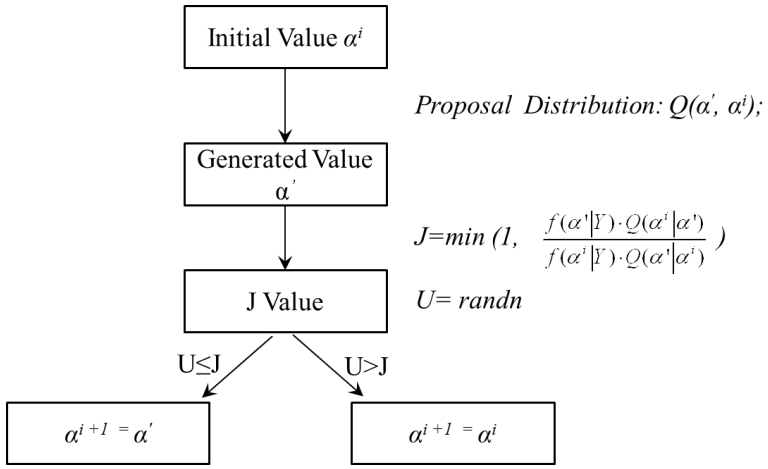

Figure 5.2. Single loop of MCMC sampling

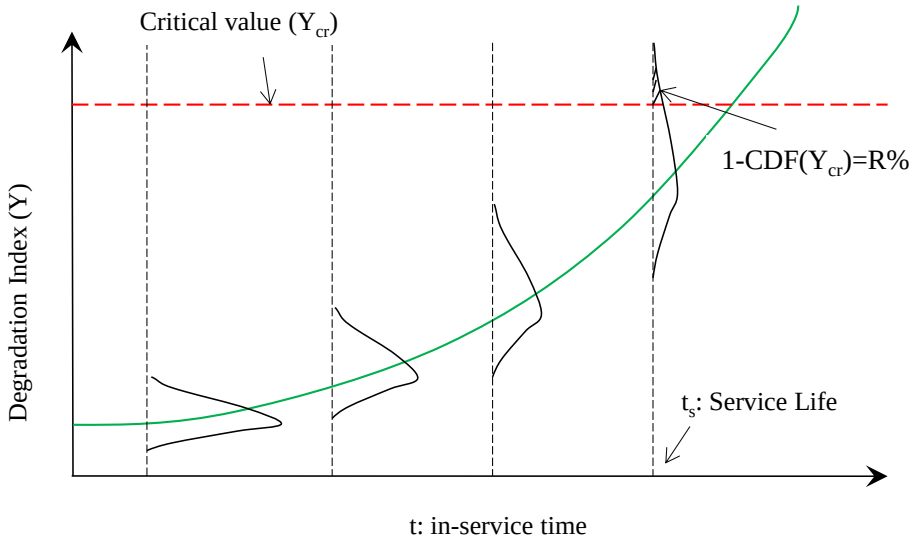

Figure 5.3. Schematics of RUL estimation using a stochastic degradation model

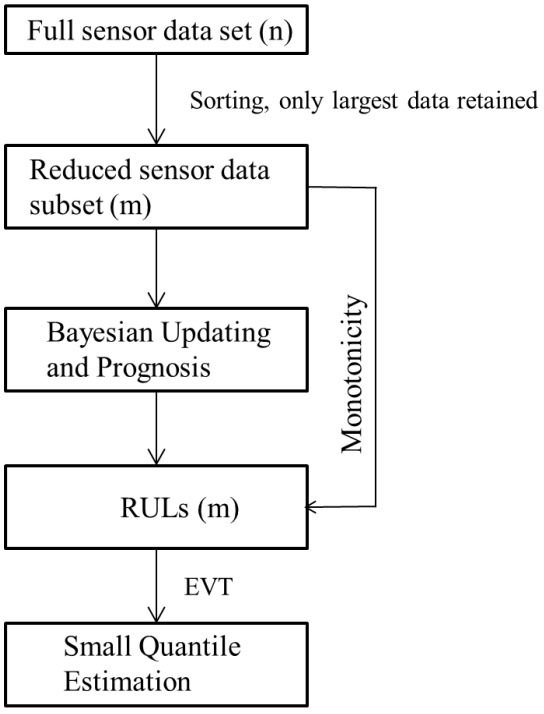

Figure 5.4. EVT-based structural health prognosis procedure

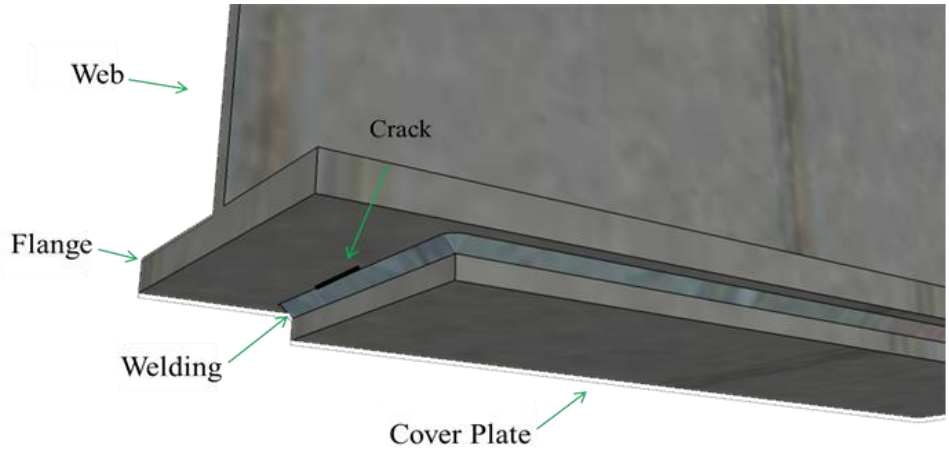

Figure 5.5. Schematics of fatigue details of bridge cover plate

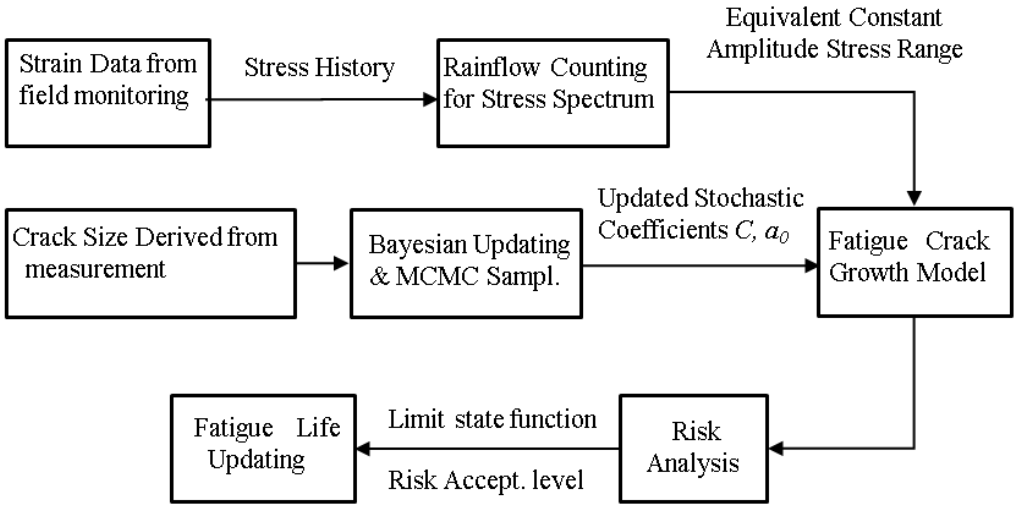

Figure 5.6. Fatigue prognosis for cover plate

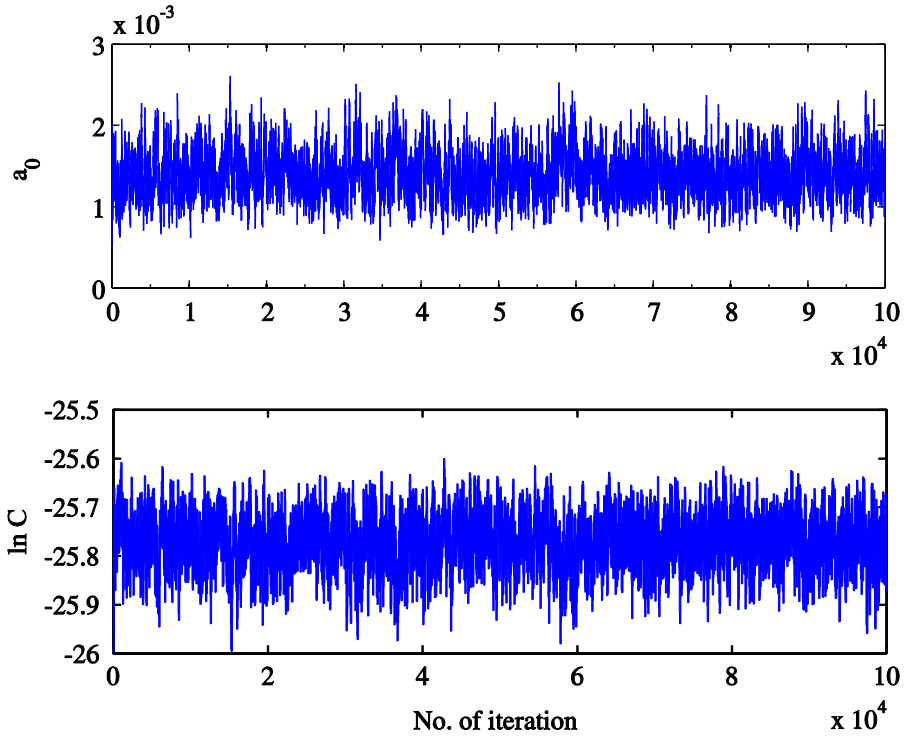

Figure 5.7. Samples of a_0 and ln$C$ from updated distribution using MCMC

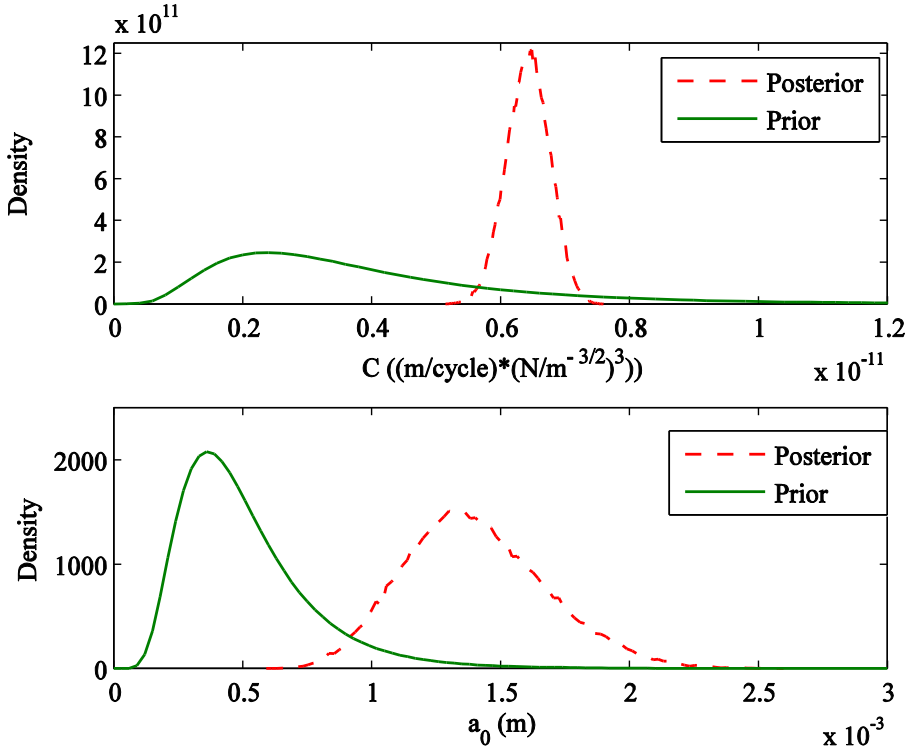

Figure 5.8. Probability distribution of model parameters, a_0 and C, before and after updating

(a)

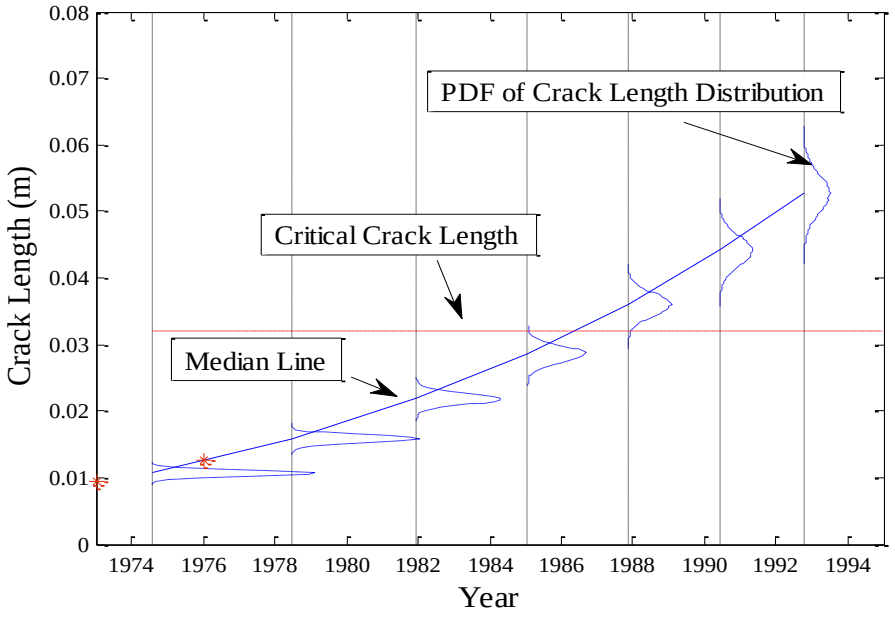

(b)

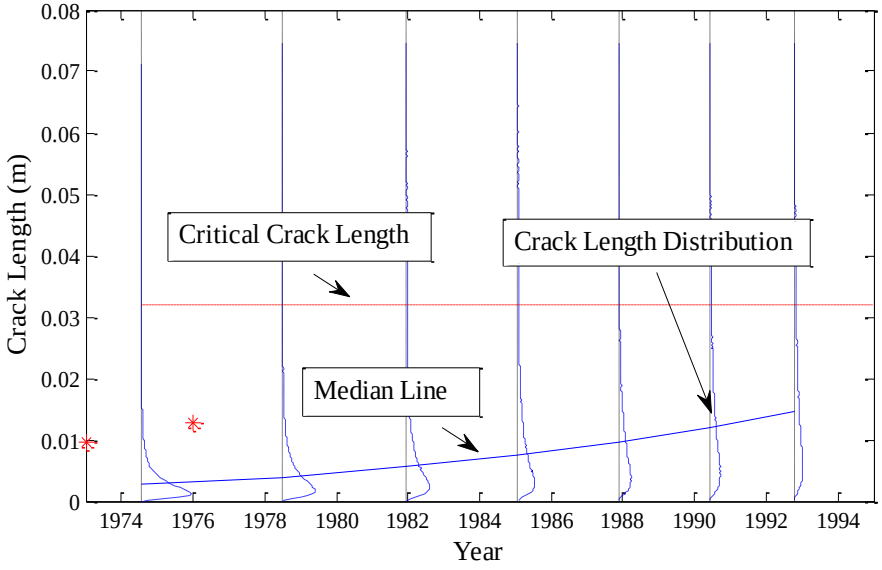

Figure 5.9. Variation of estimated degradation index (i.e., fatigue crack): (a) with updating; (b) without updating

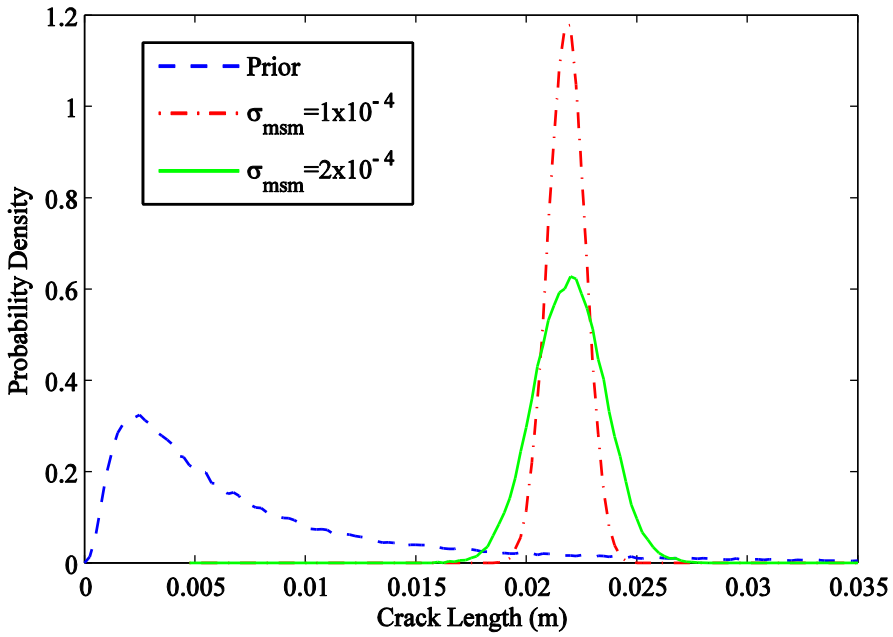

Figure 5.10. Distribution of fatigue crack length (estimated after 30 million load cycles)

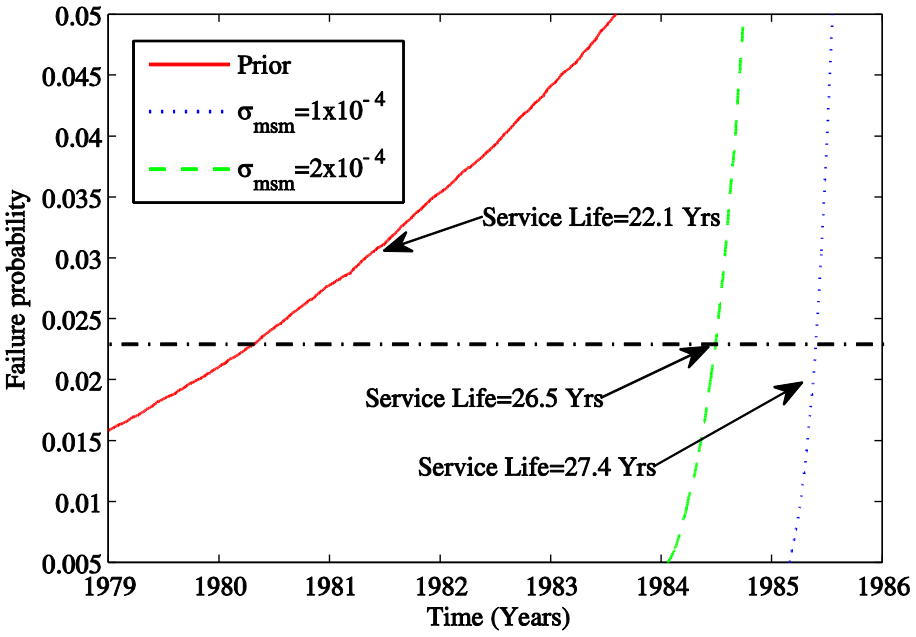

Figure 5.11. Failure probability of the cover plate fatigue detail on the Yellow Mill Pond Bridge predicted from structural health prognosis procedure

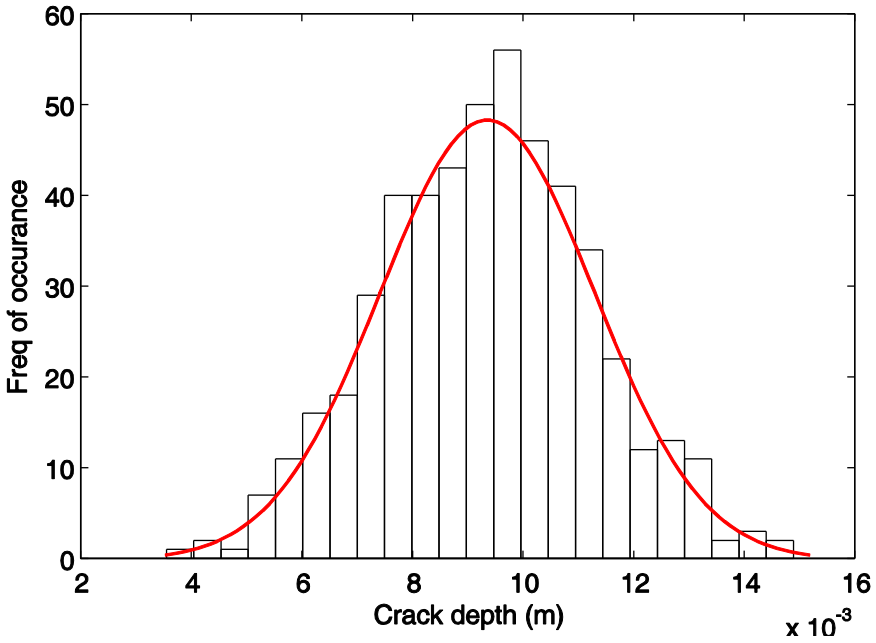

Figure 5.12. Histogram of simulated fatigue crack depth data

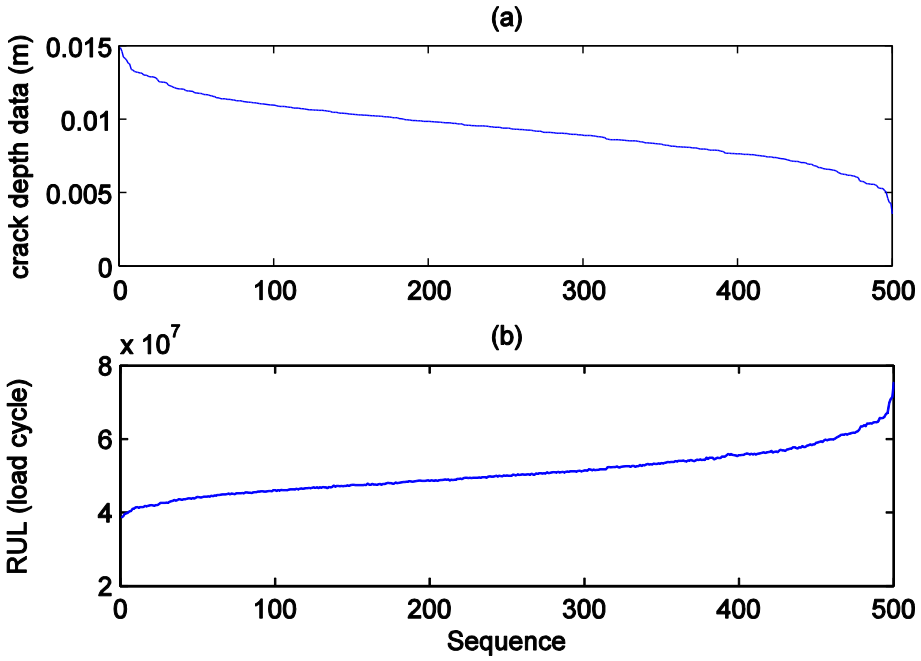

Figure 5.13. Crack depth data and corresponding estimated RULs

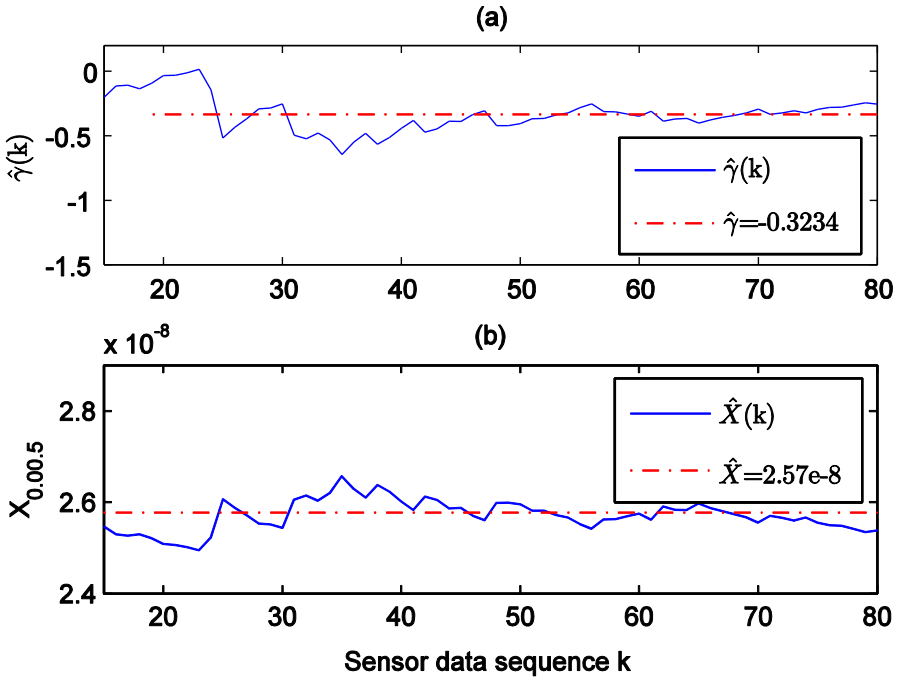

Figure 5.14. Extreme value index and quantile estimation

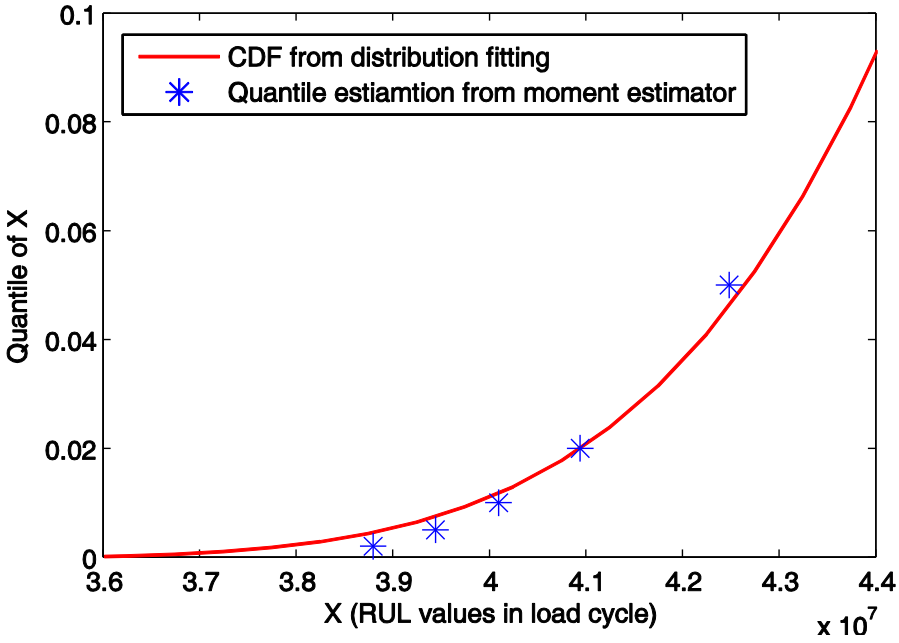

Figure 5.15. Cumulative distribution of fatigue RUL

Chapter 6: Prognosis Study of Fatigue Test Specimens

6.1 Introduction

In this chapter, fatigue prognosis of three fatigue test specimens is carried out using the proposed prognosis procedure. Prognosis with the linear elastic fracture mechanics (LEFM) model and empirical failure model are both studied. Prognosis using the fatigue test data is first performed with the LEFM model. Crack length data from earlier stage with smaller values are used as input to update the LEFM model and predict fatigue crack growth. Results are compared with that from traditional linear regression method. Then, prognosis with the empirical failure model is carried out using all measured crack length data available till the termination of the test. Limitations of the empirical failure model in fatigue data fitting are discussed and a data selection method based on coefficient of determination values is proposed to improve the goodness of fit.

6.2 Prognosis using the LEFM model

Specimens WTJ1 and WTJ2 were used for crack measurement technique training and adjustment purpose. Therefore, crack length propagation data was not kept. WTJ3 failed prematurely at 2.18×10^5 load cycle which was totally unexpected and thus no crack measurement was performed. Therefore, only crack length data for three specimens WTJ4 to WTJ6 are available for prognosis study. In this chapter, all prognoses are done using the crack length data obtained from specimens WTJ4 to WTJ6.

6.2.1 Model updating and crack depth propagation prediction

6.2.1.1 Crack length data and aspect ratio

The values of both deterministic and stochastic parameters for the adopted LEFM model are listed in Table 6.1 and Table 6.2. The LEFM model uses the crack depth a as the input data. Since the crack depth is much more difficult to measure especially at early stage, surface crack length was measured instead and crack depth is derived from the measured crack length value using a pre-specified relationship named aspect ratio. Aspect ratio is defined as the ratio of crack depth to half crack length (a/c). According to the equations for aspect ratio, aspect ratio keeps decreasing from initial value to 0.2 when the crack depth reaches 25 percent of the tube wall thickness. After that, the aspect ratio is considered as a constant value of 0.2 until the failure. As for signal support structures tested in this study, it has a relatively thin wall with a wall thickness T of 6.4 mm. The LEFM model is only valid for crack with a depth less than $0.9T$, which is 5.76 mm in this study. The corresponding crack length $2c$ = 57.6 mm. After the maximum crack length is exceeded, the structure is considered to have reached its fatigue life corresponding to a critical crack length of $0.9T$. Only crack length data smaller than 57.6 mm is thus used for the prognosis in the present study of the LEFM model.

Crack depth data used for prognosis are plotted in Figures 6.1 to 6.3 for specimens WTJ4 to WTJ6 respectively. The crack length data were firstly measured using a digital microscope. Then, crack depths were derived from the crack length data based on aspect ratio equations. Since the smallest marking on the paper tape measure placed along the weld toe is 1 mm for reading under microscope, the measurement error for crack size is within 1 mm if no cognitive bias is incurred. By assuming the

general error term is on the same order of magnitude as the measurement error, it is assumed to have the standard deviation of 1 for use in this fatigue life prognosis study.

6.2.1.2 Model parameter distribution updating

With the crack length measurements, the distributions for the three stochastic coefficients C, a_0, and $(a/c)_0$ of the fatigue growth model are updated using the proposed prognosis procedure for specimens WTJ4 to WTJ6. The updated mean values for these stochastic parameters are listed in Table 6.2. The mean value of parameter C deviates from the prior value of 2.0×10^{-13} to updated value of 1.84×10^{-14} for specimen WTJ4 while the mean values for a_0 and $(a/c)_0$ change a little (all within 15% difference). This is in agreement with the findings reported by Walbridge (2005). Their sensitivity study shows the LEFM model is mostly sensitive to parameter C. For parameter C, many factors could impact its value such as material properties and it would deviate from experiment to experiment. Experiments on full-scale specimens are thus important to determining reliable C values for specific applications. Also, for the updated mean value of C, the results from WTJ5 and WTJ6 (5.37×10^{-14} and 6.03×10^{-14}) are close to each other while the C value for WTJ4 (1.84×10^{-14}) is much smaller. As for the LEFM model, the larger value C has, the faster the crack growth rate becomes and the smaller the fatigue life is. Therefore, this is consistent with the situation that WTJ4 has a fatigue life much larger than the fatigue lives of WTJ5 and WTJ6.

6.2.1.3 Crack depth growth prediction

Figures 6.1 to 6.3 also provide the crack depth growth curve estimated with the updated fatigue growth model for specimens WTJ4 to WTJ6 respectively. It is seen from Figure 6.2 that the fatigue growth model with updated parameters is in good

agreement with the measured crack size data for WTJ5. Also, Figure 6.1 gives a good fit for WTJ4 although the first two data points are deviating a little from the predicted curve. This might be due to the measurement error since the readings of the first two data are small with tiny crack opening. For WTJ6, the updated curve does not capture the crack growth trend reflected by the measured data as shown in Figure 6.3. This might be caused by multiple crack initiation. As mentioned in the discussion of crack surface features in Chapter 4, there are several dark initiation spots and ratchet marks observed on the fracture surface of WTJ6. This also causes the beach marks not to be semi-elliptical. Also, the aspect ratios for these marks are comparatively small (0.046, 0.046, 0.053) due to the multiple crack initiation. Therefore, the assumed aspect ratio equation for WTJ6 does not hold true for the actual crack shape. The crack did not penetrate the tube wall thickness before load cycle reached 270,000 based on beach marks. However, using the assumed aspect ratio relationship for updating the LEFM based fatigue crack growth model, fatigue crack would have fully penetrated the tube wall thickness before load cycle number N = 180,000. This caused the predicted crack growth curve not match well with the measured data.

It is noted in Figure 6.2 that for the early stage (before 190,000 load cycle) of the predicted crack growth curve, there are no measured data available due to the limitation of the crack measurement technique. The updated model gives a prediction of how crack propagation would likely be in the early stage. An updated value of initial crack depth a_0 is also obtained from model updating. Crack growth curves corresponding to the 5%, 50% (median), and 95% quantiles are plotted in Figure 6.2.

Another thing worth noting is that the LEFM based fatigue growth model is only

valid before the crack reaches ninety percent of the tube wall thickness when the structure is considered to fail. However, the crack would further propagate after this before it becomes completely unstable and load capacity drops substantially. Therefore, the calculated fatigue life from this model is more conservative in comparison with the total number of load cycle at test termination.

6.2.2 Discussions

6.2.2.1 Linear regression

The fatigue prognosis procedure applies the Bayesian theorem and MCMC when updating the fatigue growth model to obtain posterior distributions for the fatigue model parameters. Another commonly used approach for determining the parameter values in a deterministic fatigue growth model (e.g., Paris Law) is the linear regression method. It uses the log-log linear form of the Paris law as Eqn. (6.1).

$$\log(da/dN) = m \cdot \log(\Delta K) + \log(C) \tag{6.1}$$

The data of da/dN and ΔK is used to curve fit the value of m as the slope and the value of $\log(C)$ as the intercept (Yazdani and Albrecht 1987). Since m is usually considered constant in updating based on Bayesian theorem, it is also assumed to be constant (i.e., m = 3.0) here for the linear regression. Only the value of C is to be regressed using the linear regression. For the initial crack depth a_0, it takes the mean value of prior distribution from LEFM model assumptions.

The linear regression results for specimens WTJ4 to WTJ6 and corresponding prognosis curve are presented in Figures 6.4 to 6.6 respectively. For example, in Figure 6.5a, C is obtained from linear regression. The coefficient of determination is 0.8446 and the mean square error is 0.1815. Using this regressed C value for the

fatigue growth model, the crack growth curve is plotted in Figure 6.5b. Clearly, the fatigue growth curve using regressed values deviates considerably from the measured data. Similar situations can also be observed in Figure 6.4 and Figure 6.6. Possible reason for the large deviation is that small regression residual error in the log-log linear form of the Paris law equation could lead to large error in its non-linear form.

6.2.2.2 Comparisons

A comparison of Figure 6.2 and Figure 6.5b suggests that the result from the Bayesian method fits the measured crack data better than that of the regression method. Similar results can also be seen in WTJ4 and WTJ6 as shown in Figures 6.1 to 6.6. A summary of the regression results are listed in Table. 6.3. Also, comparison of the results between the two different methods can be made by looking at Table 6.4. Conclusion can be drawn that when the regressed values for C and m are used for the LEFM based fatigue growth model, the obtained crack growth curve does not fit the measured data well, evidenced by the large deviation between these two. Also, another disadvantage of the linear regression method comparing with the Bayesian updating procedure is that it can only update the parameters of C and m. On the other hand, the Bayesian procedure can update any combination of stochastic parameters.

6.3 Prognosis using empirical failure model

In this dissertation study, discussion of the empirical failure model is restricted to fatigue cases with constant amplitude loading only. Therefore, it is necessary to convert the recorded crack length data from the fatigue test into those with constant amplitude loading first. Miner's rule is employed here to do this.

6.3.1 Corrected load cycle number

According to the Miner's rule (Miner 1945), the damage induced by a single loop is considered to be the multiplication of load cycle and the stress range. In this fatigue test, load is applied at the end point of the cantilevered specimen. The stress range is proportional to the range of the applied moment. Miner's rule can be applied to the loading record and transfer it into constant amplitude loading. The equivalent loading cycle number can be calculated using Eqn. 6.2.

$$N_e = \frac{\sum_{i=1}^{i=k} N_i M_i}{M_e} \tag{6.2}$$

In Eqn. (6.2), M_i is the bending moment acting at the end section of the test specimen. N_i is the number of loading cycle at the load level M_i. N_e is the equivalent load cycle number at the load level M_e.

WTJ1:

The cyclic load range was kept constant at the early stage of the test. However, the length of the arm from load point to the weld toe was adjusted from 1.83 m (6') to 1.52 m (5') at load cycle no. N = 560,678 during the test. The moment at the weld toe before the loading setup adjustment is taken as M_e. N_e is calculated to be 6.09×10^5 which is smaller than the recorded value of 6.19×10^5.

WTJ2:

The target cyclic load range was increased from 22.06 kN to 25.08 kN at load cycle number N = 941,700 to accelerate the test till the termination of the test at $N = 12.46 \times 10^5$. M_e is chosen to be the bending moment value before the load increase. N_e is calculated as 13.38×10^5 which is larger than the recorded total load cycle of 12.46

$x10^5$.

WTJ4:

Displacement control mode is used throughout the test. The target displacement of the actuator kept constant. At the final stage of the crack propagation, the bending stiffness of the tube decreased due to large crack. Hence, the applied moment dropped at the final stage of loading although displacement parameters are kept the same. The corrected total load cycle number N_e is $5.78x10^5$ while the recorded total load cycle is $5.82x10^5$. The difference is less than 1% of the fatigue life of WTJ4.

WTJ5:

The target loading was kept constant throughout the test. N_e equals the recorded value.

WTJ6:

Beach marking method is used, two load ranges are applied. Using the bending moment value for the larger load range as M_e, the calculated equivalent total load cycle number N_e is equal to $3.40x10^5$ which is smaller than the total load cycle of $3.55x10^5$.

One notable thing is that after transforming the crack length record for all specimens into equivalent constant loading condition, the resulting fatigue life N_e still varies a lot from specimen to specimen even though similar moment is applied. The equivalent load cycle is also named corrected load cycle here. Table 6.5 lists the corrected fatigue life for all six specimens.

For comparison purpose, both the uncorrected crack growth curve from direct measurement and the corrected crack growth curve are shown in Figure 6.7. It is seen that for WTJ4, the two curves overlap each other except for the final stage when the

load range started dropping due to cracking. For WTJ5, they are identical since the load range is kept constant all the time. For WTJ6, the two curves started to deviate from each other when beach-marking loading started.

6.3.2 Data segment selection method

One feature of the empirical failure model is that the growth rate of the modeled degradation process should be monotonically increasing. However, in reality, the crack growth rate might slow down occasionally due to various reasons, for example, reduced fatigue load range. In such cases, multiple acceleration stages could happen during the fatigue crack propagation process. Under such condition, it is preferred that the data set is divided into several segments and the empirical failure model is updated for the stages with monotonically increasing rate only. In order to automate this in prognosis practice, a data selection method based on the coefficient of determination (R^2) is proposed in this study.

For data set with monotonically increasing rate, generally increasing number of data points would improve the goodness of fit for the updated model. Therefore, the R^2 value would get closer to 1 when more data points become available. Small fluctuation might exist in R^2 values due to the uncertainty and noise in the measured data and the degradation process. Yet no significant drop of R^2 value should happen. However, if deceleration in the measured data is observed, the goodness of fit of the empirical model to the data set would also deteriorate which will be reflected as the sudden drop of R^2 value. In this study, a data selection procedure based on this observation is proposed. A flow chart illustrating this procedure is shown in Figure 6.8. With each data point taken in and the Bayesian updating executed, the R^2 value is

examined to see if a new acceleration stage starts. If a relatively large drop of R^2 value occurs, it is concluded that a new acceleration stage begins and all previous data points are discarded. The selection of a small constant value δ in the criterion is to avoid misinterpretation of data fluctuation (e.g. caused by noise) into new acceleration stage.

6.3.3 Prognosis result without data selection

In order to perform prognosis using the empirical failure model, initial estimated parameter values for the model have to be provided as the prior distribution. One thing to mention here is that the load cycle number t_i applied to the empirical failure model is the load cycle since the first measurement. It represents the time interval of the crack propagation at final stage. And a relation exits between failure time t_f and total fatigue life T_f as given in Eqn. (6.3)

$$T_f = t_f + t_1. \tag{6.3}$$

In Eqn. (6.3), t_1 denotes the load cycle at the first measurement.

In this study, linear regression is applied on the crack length data of specimens WTJ4 to WTJ6 to determine the initial parameter values for γ_1, γ_2 and t_f. In practice, initial values can be derived from similar applications with recorded data. The results are listed in Table 6.6. The mean values and standard deviation are calculated using linear regression results for the three specimens.

The distribution of γ_1, γ_2 and t_f are updated using crack measurements for each specimen using the empirical failure model based prognosis procedure. The error term in the general degradation model is still assumed to follow normal distribution with zero mean and standard deviation of 1, which is the same as those of the LEFM

model. Each time a new data point is obtained, updating is performed using all available data within the current data segment and a new set of updated parameter values are calculated. The fatigue life T_f with updated t_f values for specimens WTJ4 to WTJ6 are given in Figures 6.9, 6.11 and 6.13 respectively. Also, the corresponding coefficients of determination (R^2) for all three specimens are plotted in Figures 6.10, 6.12, and 6.14 respectively.

Figure 6.9 shows that for WTJ4, the estimated T_f converges near load cycle number N = 5.35x10^5 with an estimated T_f equal to 5.78x10^5 cycles. This is very close to the corrected load cycle at test termination which is 5.76x10^5. In this case, the empirical failure model based prognosis method is able to give some early-warning before the complete structural failure. For WTJ6, T_f also converges as early as around 2.5x10^5 cycles as shown in Figure 6.13 while the load cycle at test termination is 3.4x10^5, leaving a remaining fatigue life of 9x10^4 cycles before complete failure. For WTJ5, however, T_f fluctuates to some extent in the updating process, as shown in Figure 6.11. By looking at the R^2 plot for WTJ5 in Figure 6.12, it is seen that a sudden decrease in the R^2 value occurs in between N = 2.8x10^5 and N = 3x10^5. Meanwhile, the R^2 value at later stage of the prognosis for WTJ5 is around 0.95 which is smaller than the R^2 value for WTJ4 and WTJ6. This indicates that the empirical failure model does not fit the whole data set of WTJ5 well. By looking at the crack growth curve for WTJ5 in Figure 6.7, it can be seen that there exists a deceleration stage for crack propagation around N = 3x10^5. This coincides with the sudden drop of the R^2 value. In order to make the empirical failure model applicable to WTJ5, the data selection method based on R^2 needs to be applied.

6.3.4 Prognosis result with data selection

The prognosis for WTJ5 is performed again, but augmented with the R^2 data selection method. The constant value of δ is set to be 0.03 based on some tests. For different application, this value might vary. At $N = 3.0169 \times 10^5$, there is a sudden drop for R^2 value. Therefore, according to the procedure presented in the flowchart shown in Figure 6.8, all data before $N = 3.0169 \times 10^5$ are discarded. Updating is implemented using refreshed data points collected after that point. The variation of R^2 in the updating process is shown in Figure 6.15a. It is seen that the R^2 value gradually increases and approaches 1. The T_f result is shown in Figure 6.15b. Comparing the results in Figure 6.15b with Figure 6.11, it can be observed that T_f converges in Figure 6.15b. A comparison of the curve fitting result between the updating with and without data selection is shown in Figure 6.16a and b. It can be clearly seen that with the data selection, the prognosis method gives a better fitting.

6.3.5 Discussion

Prognosis using the empirical failure model is able to provide a good estimation for the failure time t_f. As an explicit parameter, the failure time t_f is directly obtained from updating of the empirical failure model using measured data. No definition of the limit state is necessary in comparison with the prognosis based on LEFM model.

One limitation of the empirical failure model is that it can only fit the deterioration process which has monotonically increasing growth rate. In real application, the growth rate might not be monotonic. In order to make the empirical failure model applicable to such cases, a data selection method is proposed which can determine the part of the collected data suitable for model updating and prognosis use. The data set

of WTJ5 from the tubular fatigue test is used as an example to demonstrate the data selection method. With the data selection method, the empirical failure model based prognosis method is demonstrated to be able to yield a good estimate of the fatigue failure time t_f for welded tubular joints fatigue applications.

6.4 Fatigue life comparisons

AASHTO gives the fatigue life equation as Eqn. 6.3. According to AASHTO, the test specimens fall into fatigue category E' with $A = 1.28\text{x}10^{11}$. m is usually assumed to be equal to 3.

$$N = A \cdot \Delta\sigma^{-m} \tag{6.4}$$

The calculated fatigue lives for WTJ1 to WTJ6 are listed in Table 6.7. The corresponding stress ranges are equivalent stress ranges extrapolated from the time history of the measured nominal strain. Also listed in Table 6.7 are the load cycles at test termination. Since all tests are terminated at the time when surface crack length along the welding toe is at least 20 cm. It is considered that the load cycle at test termination should be close to the true failure load cycle. Table 6.7 shows that for all six specimens, the estimated fatigue lives using Eqn. (6.4) are much smaller than the load cycle at test termination. Figure 6.17 presents the load cycle at test termination for the six specimens in S-N chart together with test results for similar tubular joints by others (Archer and Gurney, 1970). In the figure, it is clearly seen that the test results fall between fatigue category C and category E, which are in good agreement with the experimental results on similar specimens by Archer and Gurney. (1970).

Another thing worth noting is that the fatigue lives for the six specimens are widely scattered. The large dispersion observed in the fatigue crack development makes

fatigue monitoring an important tool for predicting structural failure caused by fatigue cracking.

Table 6.8 lists the estimated fatigue life from both LEFM model based prognosis and empirical failure model based prognosis. It can be observed that the estimated fatigue life using empirical failure model is quite close to the load cycle at test termination (difference less than 1%). However, the estimated fatigue life based on LEFM model is always smaller than the load cycle at test termination (50% to 80%). This is explained by the limit state function defined for the LEFM based prognosis method. In this study, penetration of 90% of the wall thickness is defined as the limit state and the corresponding crack length is about 5.8 cm. However, in fatigue test, the crack could keep propagating along the weld toe well over 20cm without collapse. One thing to note is that although the empirical failure model based prognosis is able to obtain an accurate estimation of the failure time, it can only converge to the accurate estimation at later stage when less than 10% of the fatigue life remains. Still, it has the potential of complementing the current fatigue life prognosis method and can provide early-warning to avoid catastrophic structural failure like collapse.

6.5 Conclusions

Crack length data from fatigue test of welded tubular joint specimens are used for demonstrating the application of two prognosis procedures based on distinct fatigue growth models, the LEFM model and the empirical failure model. The proposed prognosis procedure has certain advantages over traditional linear regression method. First of all, it is capable of multi-parameter updating. Also, the updated model fits the data better than that from the linear regression. By applying the prognosis procedure

based on LEFM model, an updated fatigue model is made available for predicting its fatigue life.

Using the stochastic LEFM model, it is found that the crack growth curve from the updated model agrees reasonably well with the measured data. Updated distributions of the stochastic parameters such as the parameter C, initial crack depth a_0 and initial crack aspect ratio $(a/c)_0$ are obtained for three specimens and they are compared with the deterministic values of C regressed using traditional approach from the da/dN vs. ΔK dataset. This adds to the knowledge on the fatigue behavior of welded tubular joints in signal support structures. Using the updated stochastic fatigue growth model, a continuous crack growth curve can be established. This can be used for understanding how fatigue crack propagates in its early development stage, when the crack is still too small (e.g., crack length < 1mm) to measure with current instrumentation technique.

Prognosis based on LEFM model leads to conservative results (50% to 80% of the load cycle at test termination) due to the selected limit state definition. However, for the empirical failure model based prognosis, its estimated fatigue life is quite close to the load cycle at test termination (less than 1% difference). The limitation for prognosis based on this model is that it is mostly applicable to the final stage of fatigue crack growth and thus has less margin for safety and possible preventive action. However, its main application is to provide early-warning signal before catastrophic structural failure.

Table 6.1. Deterministic parameters of fatigue growth model

Tube wall thickness T (mm)	Weld toe angle θ (°)	Weld footprint length L_w (mm)	half plate width b (mm)	m	DOB (degree of bending)
6.4	45	6.4	200	3.0	1

Table 6.2. Stochastic parameters of fatigue growth model

	C ((mm/cycle)·(N/mm$^{-3/2}$)^m	Initial crack depth a_0 (mm)	Initial crack aspect ratio $(a/c)_0$
Prior mean value before updating	2.00x10^{-13}	0.2	0.5
Updated mean value, specimen WTJ4	1.84x10^{-14}	0.1662	0.4899
Updated mean value, specimen WTJ5	5.37x10^{-14}	0.1860	0.4879
Updated mean value, specimen WTJ6	6.03x10^{-14}	0.1867	0.4901

Table 6.3. Linear regression result

	C ((mm/cycle)·(N/mm$^{-3/2}$)^m	s (mean square error)	R^2
WTJ4	2.45x10^{-14}	0.1633	0.8695
WTJ5	4.09x10^{-15}	0.1385	0.8446
WTJ6	2.04x10^{-14}	0.2496	-0.2160

Table 6.4. Comparison of the regressed result with model updating result

		C ((mm/cycle)·(N/mm$^{-3/2}$)^m	m
Prior		2.00x10^{-13}	3
WTJ4	Regression	2.45x10^{-14}	3
	Updated mean	1.84x10^{-14}	3
WTJ5	Regression	4.09x10^{-15}	3
	Updated mean	5.37x10^{-14}	3
WTJ6	Regression	2.04x10^{-14}	3
	Updated mean	6.03x10^{-14}	3

Table 6.5. Corrected load cycle number using Miner's rule

Specimen	Recorded total load cycle (x10^5)	Corrected load cycle N_e (x10^5)	Correspondent loading moment range M_e (kN-m)
WTJ1	6.19	6.09	39.53
WTJ2	12.46	13.38	33.06
WTJ3	2.18	2.13	39.20
WTJ4	5.82	5.76	39.74
WTJ5	3.90	3.90	39.68
WTJ6	3.55	3.40	39.55

Table 6.6. Updated stochastic parameters for the empirical failure model

Parameter	WTJ4	WTJ5	WTJ6	mean	std	COV	Distribution Type
γ_1	7.66	8.10	5.12	6.96	1.61	0.23	Lognormal
γ_2	96.56	100.87	67.95	88.46	17.89	0.20	Lognormal
t_f	137,281	198,847	232,551	189,559	48,309	0.26	Normal

Table 6.7. Fatigue life data of test specimens

Specimen	Nominal stress range at weld toe (MPa)	Estimated fatigue life from AASHTO (x10^5 cycles)	Load cycle at test termination (x10^5 cycles)
WTJ1	111.04	0.93	6.19
WTJ2	111.10	0.93	12.46
WTJ3	125.00	0.66	2.18
WTJ4	127.70	0.61	5.82
WTJ5	125.70	0.64	3.90
WTJ6	116.94	0.93	3.55

Table 6.8. Fatigue life estimations for specimens WTJ4, WTJ5 and WTJ6

Specimen	Corrected load cycle at test termination ($x10^5$ cycles)	Mean value of estimated fatigue life (LEFM model, $x10^5$ cycles)	Mean value of estimated fatigue life (Empirical failure model, $x10^5$ cycles)
WTJ4	5.78	4.74	5.78
WTJ5	3.90	2.77	3.90
WTJ6	3.40	1.68	3.52

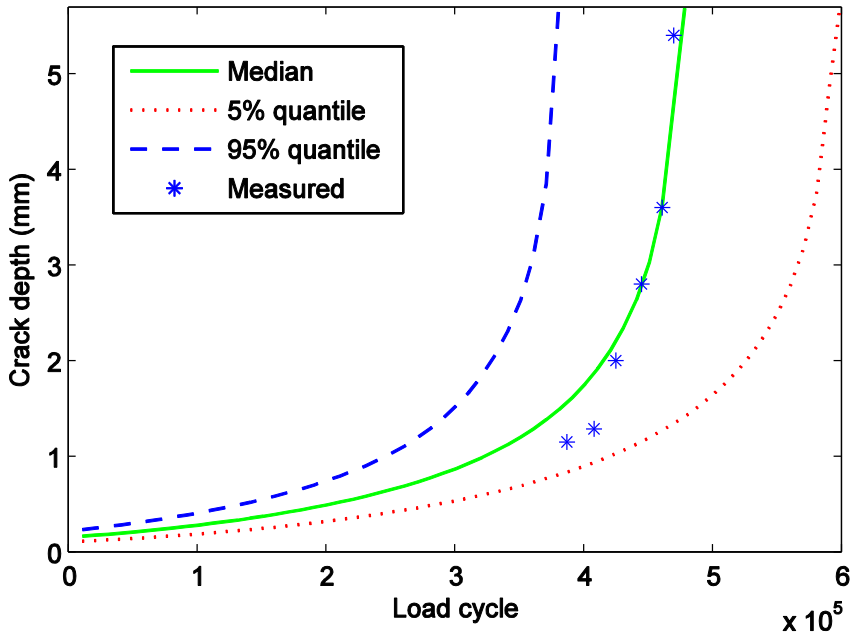

Figure 6.1. Predicted crack growth curve for WTJ4

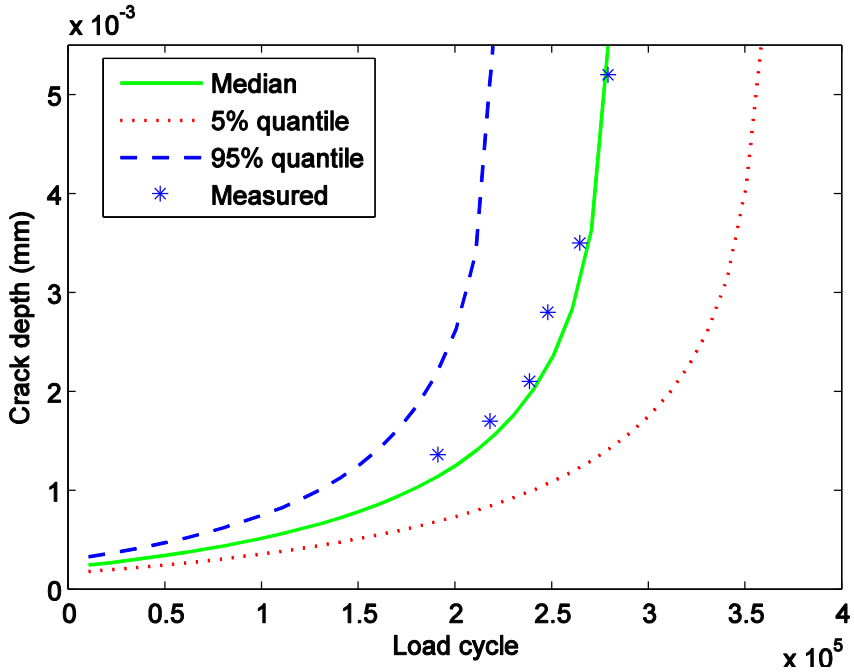

Figure 6.2. Predicted crack growth curve for WTJ5

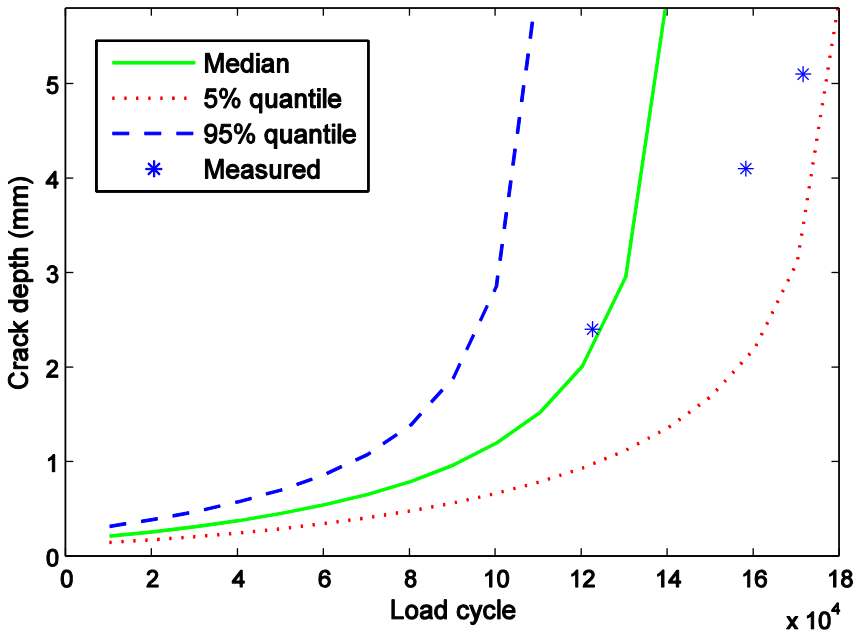

Figure 6.3. Predicted crack growth curve for WTJ6

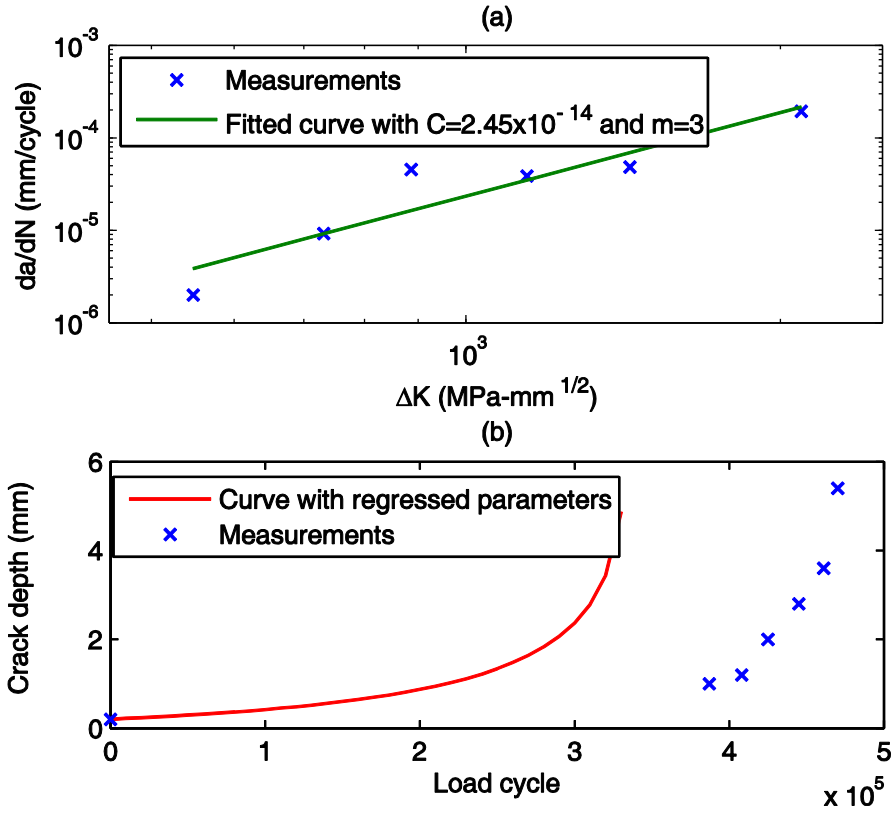

Figure 6.4. (a) Linear regression of fatigue growth model parameters; (b) Predicted fatigue crack growth prognosis using linear regression data from WTJ4

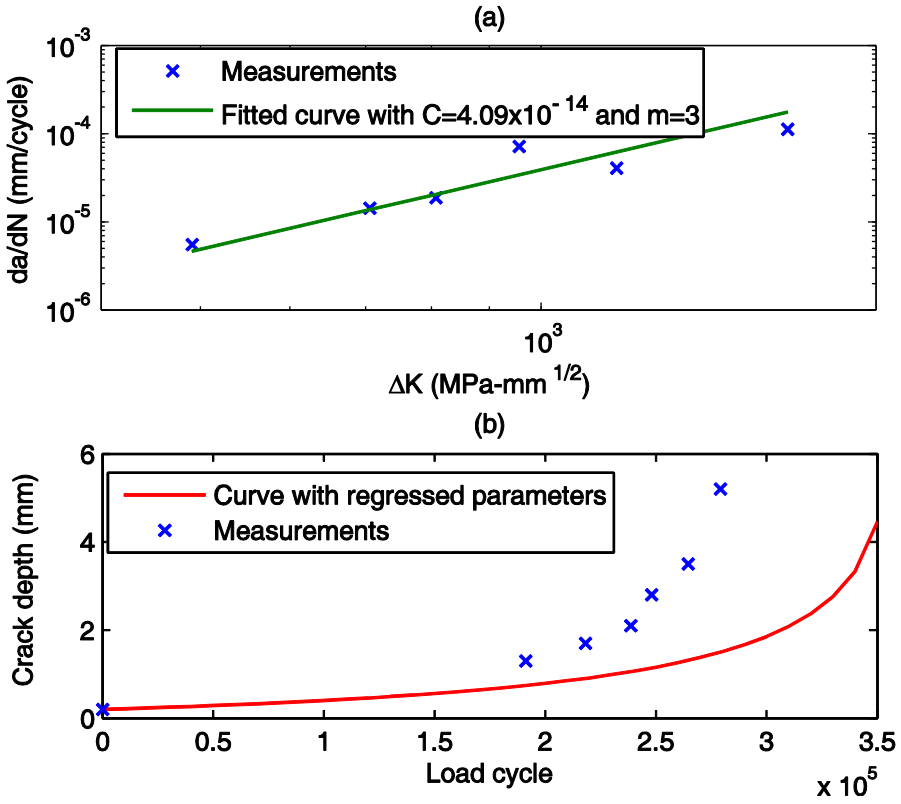

Figure 6.5. (a) Linear regression of fatigue growth model parameters; (b) Predicted fatigue crack growth prognosis using linear regression data from WTJ5

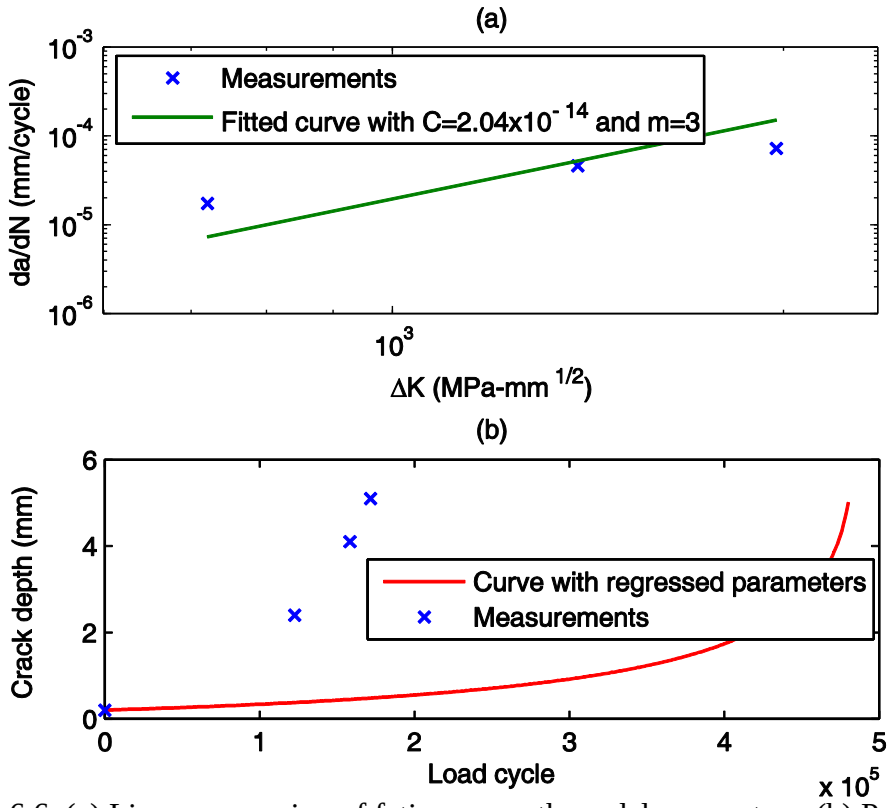

Figure 6.6. (a) Linear regression of fatigue growth model parameters; (b) Predicted fatigue crack growth using linear regression data from WTJ6

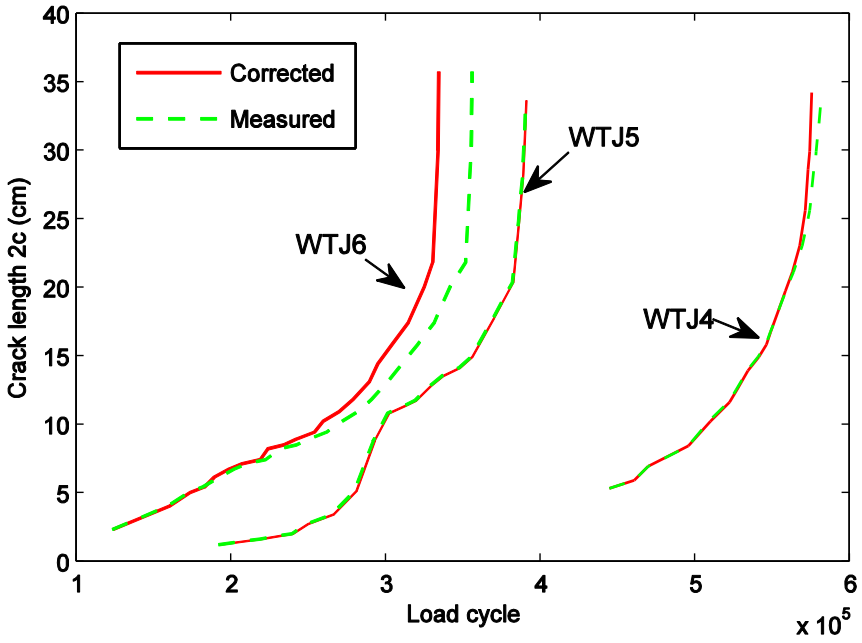

Figure 6.7. Comparison between corrected crack growth curve and original measured crack growth curve

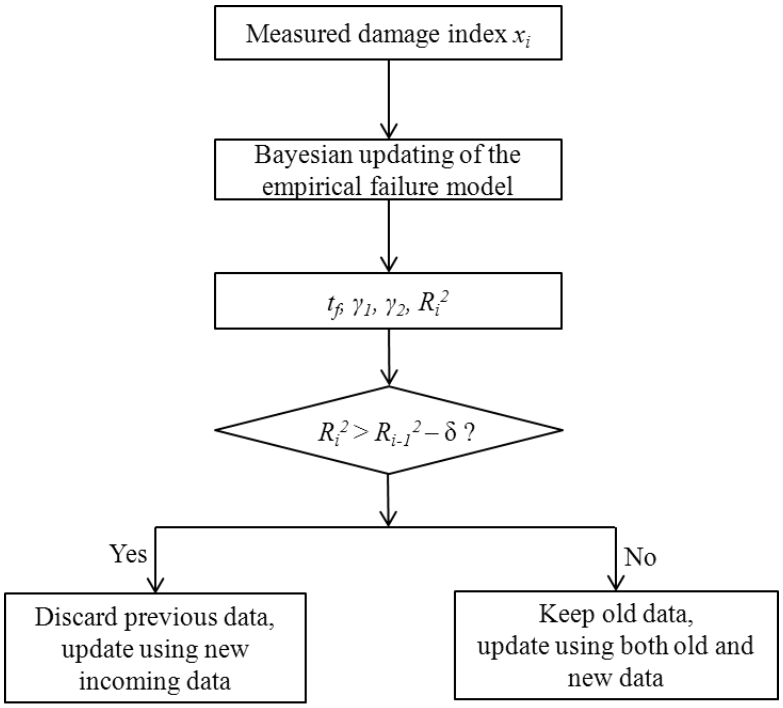

Figure 6.8. Flowchart of R^2 based data selection method

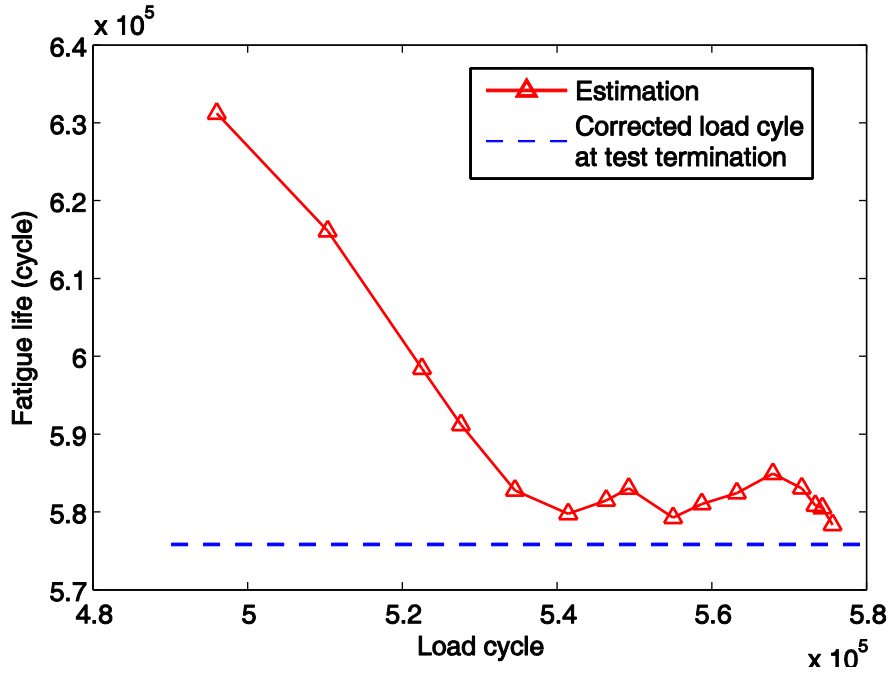

Figure 6.9. Updated fatigue life for test specimen WTJ4

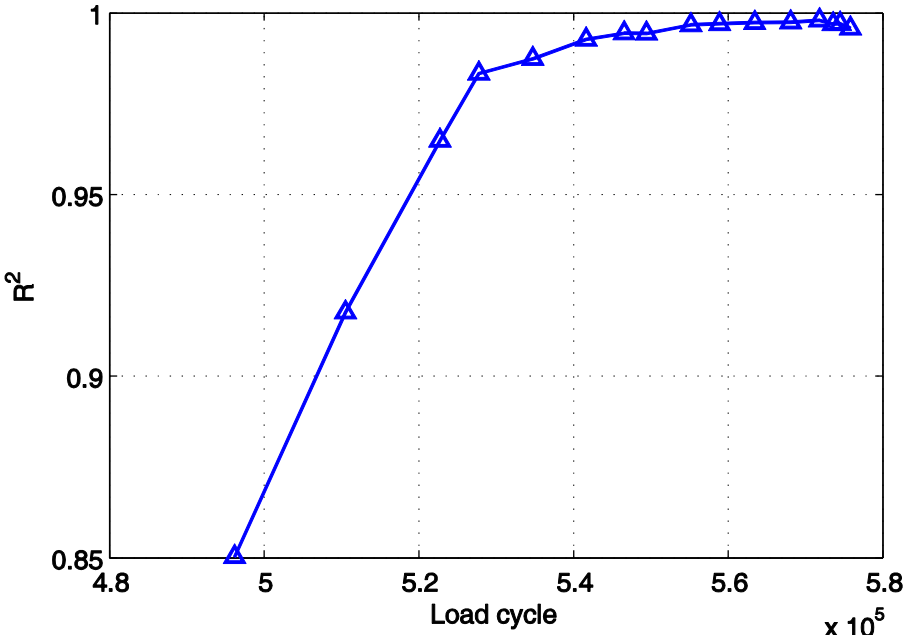

Figure 6.10. R^2 variation in model updating for test specimen WTJ4

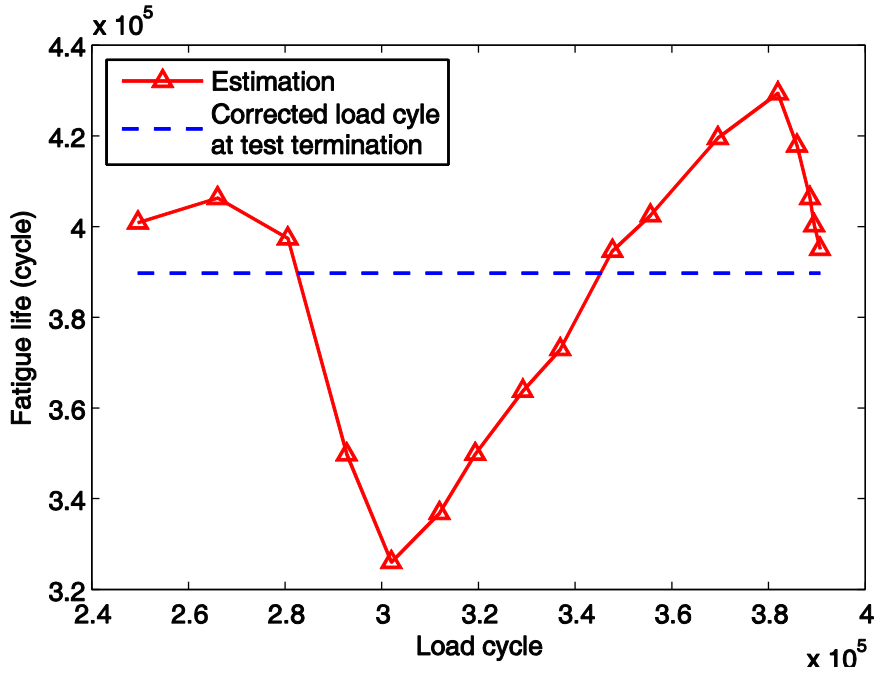

Figure 6.11. Updated fatigue life for test specimen WTJ5

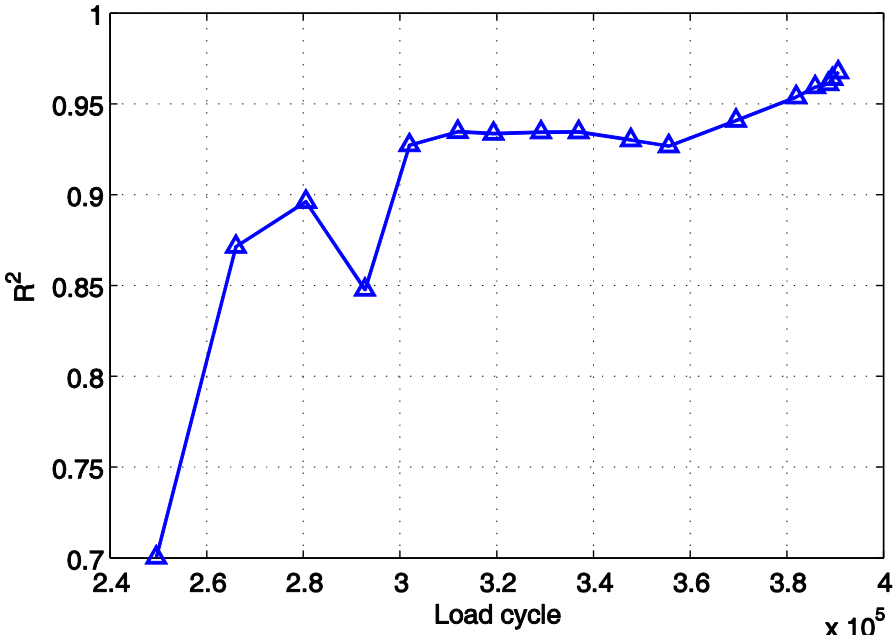

Figure 6.12. R^2 variation in model updating for test specimen WTJ5

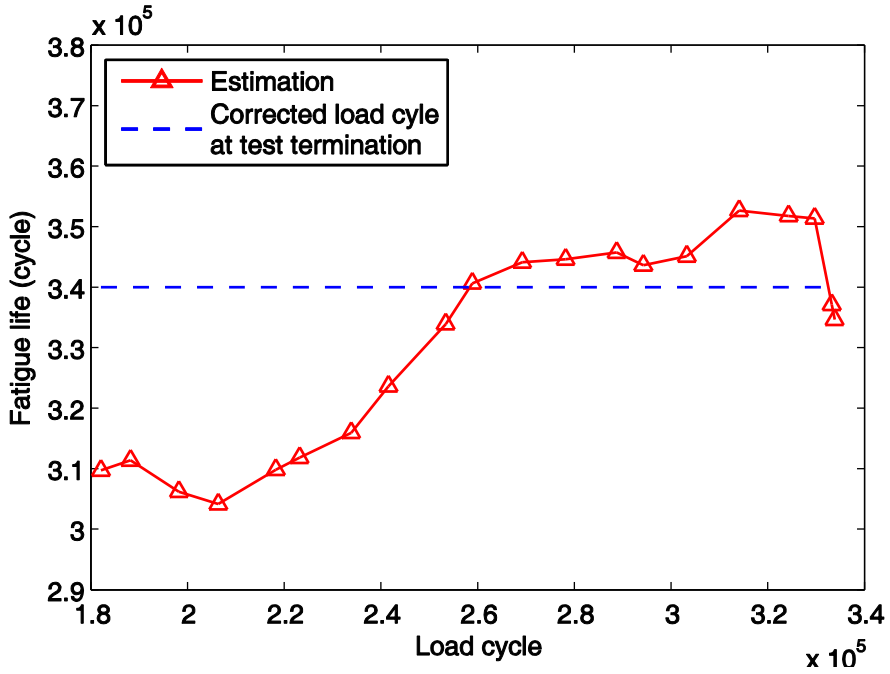

Figure 6.13. Updated fatigue life for test specimen WTJ6

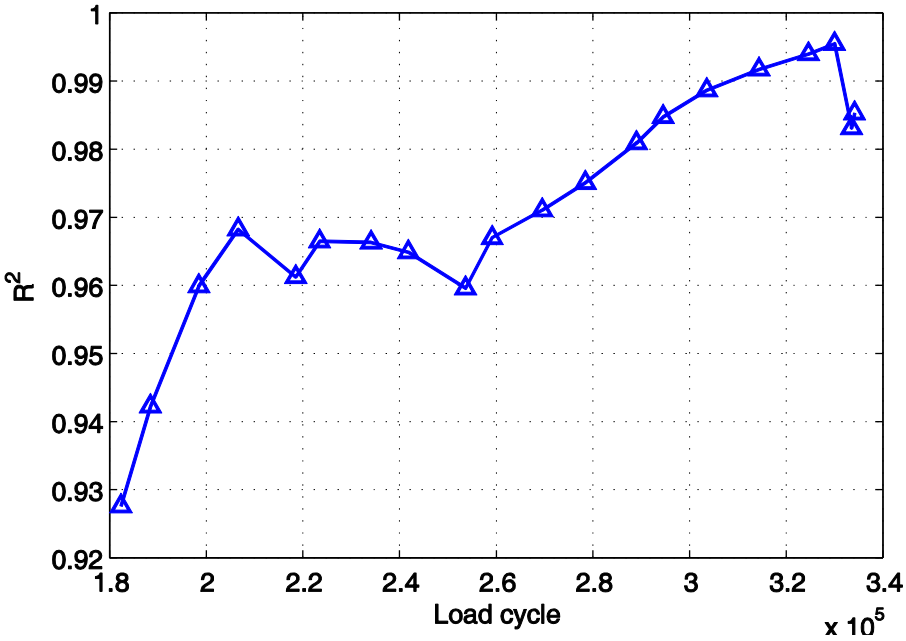

Figure 6.14. R^2 variation in model updating for test specimen WTJ6

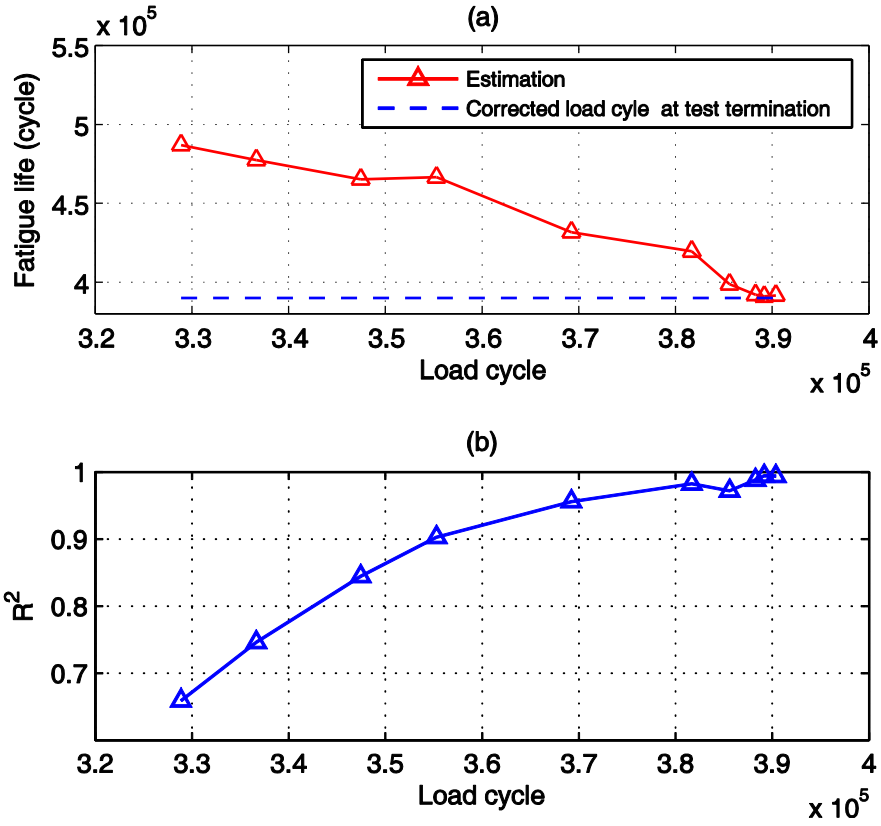

Figure 6.15. Results of WTJ5 with data selection

(a) Curve fitting without data selection

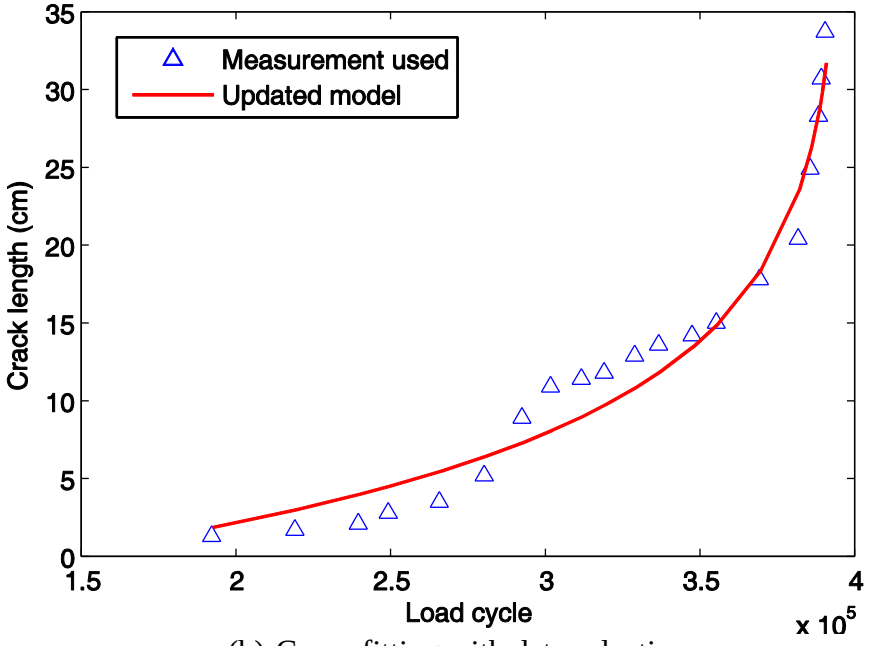

(b) Curve fitting with data selection

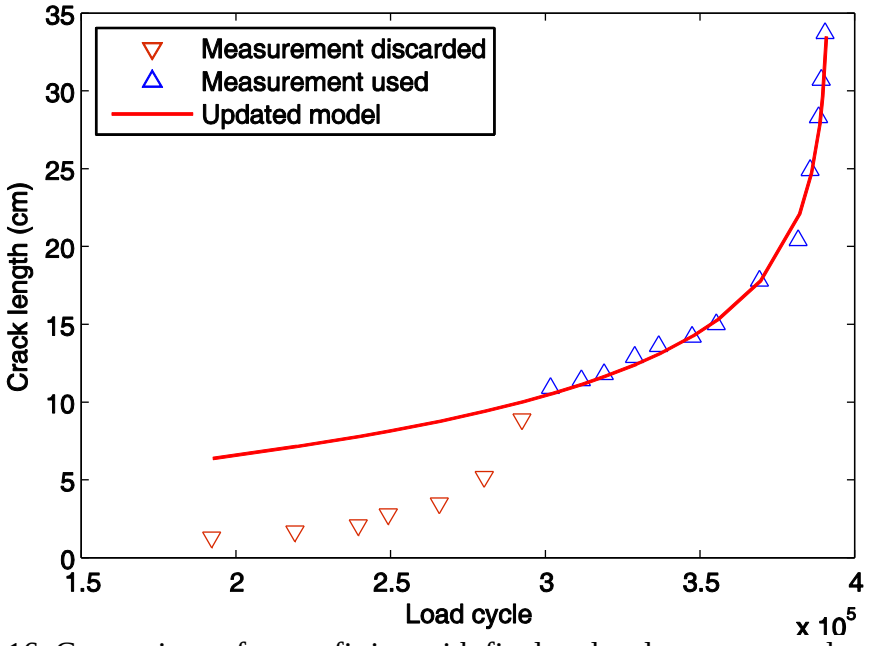

Figure 6.16. Comparison of curve fitting with final updated parameter values without and with R^2 based data selection.

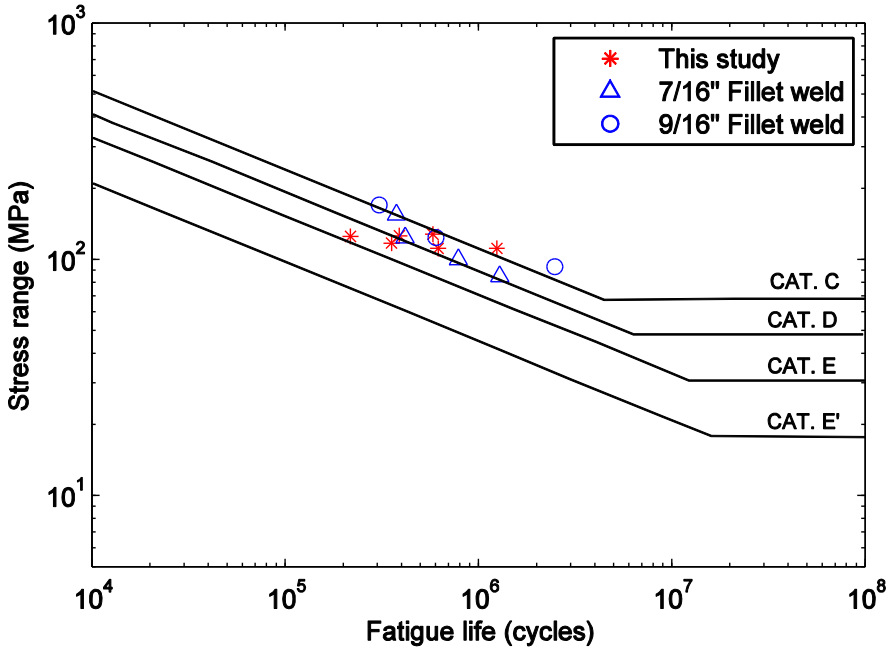

Figure 6.17. S-N curves of the welded tubular joint specimens in comparison with other test data (Archer and Gurney 1970)

Chapter 7: Conclusions and Future Work

7.1 Conclusions

The presented work intends to advance the knowledge of fatigue crack growth behaviour and its prognosis of welded tubular joints in traffic signal support structures. Specifically, the following findings are made in this research:

- *Two types of fatigue crack growth models proposed for different fatigue development regimes in the welded tubular joints of traffic signal support structures.*

  The linear elastic fracture mechanics (LEFM) model describes the fatigue crack growth behaviour of the welded tubular joints during the slow crack growth regime (stage II). As a complement to the LEFM model, the empirical failure model (EFM) is proposed for fatigue crack growth modeling in the fast crack growth regime (stage III). This empirical failure model incorporates the failure time as an explicit parameter, and thus can directly update the failure time through model updating. Knowing the failure time in advance is crucial to preventing complete structural failure caused by fatigue cracking.

- *Full-scale fatigue test conducted on six full-scale welded tubular joint specimens from traffic signal support structures to investigate their fatigue crack growth behaviour.*

  The fatigue life of the six fatigue test specimens in this study falls between AASHTO fatigue categories C and E. The experimentally derived fatigue life is thus better than the AASHTO fatigue category E' designated for this fatigue detail.

From the test results, it is found that the fatigue lives of the six test specimens are widely scattered. It is noted that fatigue life prediction using the stress-life approach does not reflect the large deviation in the test results.

For all specimens, high stress concentration at the weld toe is confirmed by measured strain data. The ratios of strain readings from two neighbouring strain gauges at hot-spot are between 1.78 and 1.87. This coincides well with the fact that all cracks initiate at the weld toe on the top ridge of the tube specimens, and propagate along the weld toe in both directions.

The semi-elliptical crack shape assumed in this study for surface fatigue crack is confirmed in at least one specimen by the water mark from dried dye penetrant on the fracture surface with an aspect ratio of 0.2. By examining the fracture surface in four test specimens, three zones of crack propagation are identified according to the surface features of the fracture surface: the origin zone with darker color, the slow fracture zone with relatively smooth surface and lighter color and the fast fracture zone with rough surface and in some cases with friction rubbing marks.

- *A sensor-driven structural health prognosis procedure incorporating long-term sensor performance degradation effect proposed*

  The prognosis procedure is capable of using sensor data of multiple modalities to update multiple random parameters in the stochastic structural degradation model. The general error term in the stochastic structural degradation model is divided into two stochastic error terms: measurement error and model error because of their different characteristics (especially over the time). Stochastic process is

applied to model the sensor measurement error to consider the sensor degradation effect. From the parametric study results, it is observed that sensor degradation rate does have an impact on the prognosis result. Proper modelling of sensor measurement error is crucial to characterizing the impact of sensor performance variation (usually deterioration) over time.

- *An extreme value theory (EVT) based structural health prognosis method proposed to reduce sensor data transmission and computing demand in prognosis*

  The EVT-based prognosis method uses moment estimator to estimate quantile values for the remaining useful life (RUL) of monitored structures. The advantage of the EVT-based prognosis method is that only a small fraction (usually < 20%) of the full sensor data set is actually used in model updating and RUL calculation. This is very appealing because model updating is computationally demanding due to the massive amount of data available from online structural health monitoring system. The EVT-based prognosis method could save the computation time, and make the prognosis more efficient without sacrificing much accuracy.

- *Prognosis with the two fatigue crack growth models tested using fatigue test data.*

  It is found that the crack growth curve given by the updated LEFM model agrees reasonably well with measured data. Updated distributions of the stochastic parameters are obtained for the welded tubular joints in signal support structures such as the parameter C, initial crack length a_0 and initial crack aspect ratio $(a/c)_0$. This adds to the knowledge on the fatigue behavior of welded tubular joints in

signal support structures. Using the updated LEFM fatigue growth model, continuous crack growth curves can be derived. This can be used for understanding how fatigue crack growth in its early initiation stage when the crack is still too small (e.g., crack length < 1 mm) to measure with current instrumentation technique.

The empirical failure model exhibits good performance in fitting with the crack length data at later stage of fatigue crack development. Estimation of the fatigue life from prognosis using the empirical failure model is quite close to the load cycle number at test termination (less than 1% difference). Although the estimate converges at a later stage of the fatigue cracking process (less than 10% of the total fatigue life), the empirical failure model based prognosis method is still able to give some early-warning before complete structural failure.

7.2 Future work

Future research work along the line of the research presented in this dissertation is recommended as follows:

- Application of the empirical failure model is illustrated using crack length data in this study since crack growth is a direct damage index correlated with the severity of fatigue damage. However, alternative damage indices such as strain or displacement can potentially be used for the empirical failure model. Future work is suggested to extend the potential application of the empirical failure model into other types of measured data.
- In order to apply the sensor-driven structural health prognosis method, a degradation model together with measurable damage index from structural health

monitoring system is required. However, such kinds of models are not always available for complicated situations such as the multiple crack initiations observed in this study. . Further study is recommended for experimental test and modelling of the fatigue behaviour of welded tubular joints with multiple crack initiations.

- For sensor degradation over long-term monitoring, stochastic models ideally should be supported by experimental data and physical explanation. However, there is a lack of such data. It is recommended that long-term field test or acceleration tests should be carried out on commonly used sensor types to continually improve the sensor performance degradation model.
- Fatigue crack length is measured using digital microscope in this study which is very labour intensive during the long fatigue test period. Sensor based measurement technique without human intervention has yet to be improved in enhancing accuracy and lowering cost. Candidates include acoustic emission sensor, eddy current sensor, while their performance varies with type of structures to be monitored. Future work is recommended to use damage index damage from continuously operated sensors.

Appendices

Appendix A: Equations for Calculating Magnification Factors in the LEFM Model

Equations for calculating Mk_b *and* Mk_m at the deepest point of the semi-elliptical surface crack are presented below. For nomenclature, please refer to Figure 3.4. These equations are adapted from the reference by Bowness and Lee (1999)

1. *Mk* for an as-welded joint: Deepest point under Bending loading (Mk_b).

For $0.005 \le a/T \le 0.5$,

$$Mk_b = f_1\left(\frac{a}{T}, \frac{a}{c}\right) + f_2\left(\frac{a}{T}, \theta\right) + f_3\left(\frac{a}{T}, \theta, \frac{L}{T}\right)$$

Where

$$f_1\left(\frac{a}{T}, \frac{a}{c}\right) = 0.065916\left(\frac{a}{T}\right)^{\left[A_1 + \left(A_2\left(\frac{a}{T}\right)\right)^{A_3}\right]} + 0.52086\exp\left[\left(\frac{a}{T}\right)^{-0.10364}\right] + A_4$$

$$A_1 = -0.014992\left(a/c\right)^2 - 0.021401\left(a/c\right) - 0.23851$$

$$A_2 = 0.61775(a/c)^{-1.0278}$$

$$A_3 = 0.00013242\left(a/c\right) - 1.4744$$

$$A_4 = -0.28783\left(a/c\right)^3 + 0.58706\left(a/c\right)^2 - 0.37198\left(a/c\right) - 0.89887$$

$$f_2\left(\frac{a}{T}, \theta\right) = A_5\left[1 - \frac{a}{T}\right]^{A_6} + A_7\left(\frac{a}{T}\right)^{A_8}$$

$$A_5 = 0.11052\theta^2 - 0.19007\theta + 0.059156$$

$$A_6 = -15.124\theta^2 + 15.459\theta - 0.0036148$$

$$A_7 = -0.047620\theta^2 + 0.16780\theta - 0.081012$$

$$A_8 = -17.195(a/T)^2 + 12.468(a/T) - 0.51662$$

$$f_3(\frac{a}{T},\theta,\frac{L}{T}) = A_9\left(\frac{a}{T}\right)^{(A_{10}\theta^2+A_{11}\theta+A_{12})} + A_{13}\left(\frac{a}{T}\right)^{A_{14}} + \left[A_{15}\left(\frac{a}{T}\right)^2 + A_{16}\left(\frac{a}{T}\right) + A_{17}\right]$$

$$A_9 = 0.75722\theta^2 - 1.8264\theta + 1.2008$$

$$A_{10} = -0.013885(L/T)^3 - 0.014872(L/T)^2 + 0.55052(L/T) - 0.072404$$

$$A_{11} = -0.065232(L/T)^3 + 0.54052(L/T)^2 - 1.8188(L/T) - 0.0022170$$

$$A_{12} = -0.034436(L/T)^2 + 0.28669(L/T) + 0.36546$$

$$A_{13} = -0.61998\theta^2 + 1.4489\theta - 0.90380$$

$$A_{14} = 0.43912\theta^2 - 1.3345\theta + 0.57647$$

$$A_{15} = -0.35848(L/T)^2 + 1.3975(L/T) - 1.7535$$

$$A_{16} = 0.31288(L/T)^2 - 1.3599(L/T) + 1.6611$$

$$A_{17} = -0.0014701(L/T)^2 - 0.0025074(L/T) - 0.0089846$$

For $0.5 < a/T < 1.0$,

$$Mk_b = 1.0$$

2. *Mk* for an as-welded joint: Deepest point under Membrane loading (Mk_m).

$$Mk_m = f_1\left(\frac{a}{T},\frac{a}{c}\right)+ f_2\left(\frac{a}{T},\theta\right)+ f_3\left(\frac{a}{T},\theta,\frac{L}{T}\right)$$

Where

$$f_1(\frac{a}{T},\frac{a}{c}) = 0.43358\left(\frac{a}{T}\right)^{\left[A_1+\left(A_2\left(\frac{a}{T}\right)\right)^{A_3}\right]} + 0.93163\exp\left[\left(\frac{a}{T}\right)^{-0.050966}\right] + A_4$$

$$A_1 = -1.0343\left(a/c\right)^2 - 0.15657\left(a/c\right)+1.3409$$

$$A_2 = 1.3218(a/c)^{-0.61153}$$

$$A_3 = -0.87238\left(a/c\right)+1.2788$$

$$A_4 = -0.46190\left(a/c\right)^3 + 0.67090\left(a/c\right)^2 - 0.37571\left(a/c\right)+4.6511$$

$$f_2(\frac{a}{T},\theta) = A_5\left[1-\frac{a}{T}\right]^{A_6} + A_7\left(\frac{a}{T}\right)^{-0.10740(\frac{a}{T})}$$

$$A_5 = -0.00038737\theta^2 + 0.64771\theta - 0.72368$$

$$A_6 = 0.24183\theta^2 + 176.23$$

$$A_7 = -0.00027743\theta^2 + 2.8143$$

$$f_1(\frac{a}{T},\theta,\frac{L}{T}) = A_8\left(\frac{a}{T}\right)^{(A_9\theta^2+A_{10}\theta+A_{11})} + A_{12}\left(\frac{a}{T}\right)^{A_{13}} + \left[A_{14}\left(\frac{a}{T}\right)^2 + A_{15}\left(\frac{a}{T}\right)+A_{16}\right]$$

$$A_8 = -0.082502\theta^2 + 0.0084862\theta + 0.38417$$

$$A_9 = 0.010766\left(L/T\right)^3 - 0.060159\left(L/T\right)^2 + 0.13667\left(L/T\right) - 0.023400$$

$$A_{10} = -0.028378\left(L/T\right)^3 + 0.16489\left(L/T\right)^2 - 0.35584\left(L/T\right) - 0.00024554$$

$$A_{11} = -0.0015061\left(L/T\right)^2 + 0.023369\left(L/T\right) - 0.23124$$

$$A_{12} = 0.051554\theta^2 + 0.025447\theta + 1.8975$$

$$A_{13} = -0.12914\theta^2 + 0.21863\theta + 0.13798$$

$$A_{14} = -0.20136\left(L/T\right)^2 + 0.93311\left(L/T\right) - 0.41496$$

$$A_{15} = 0.20188\left(L/T\right)^2 - 0.97857\left(L/T\right) + 0.068225$$

$$A_{16} = -0.027338\left(L/T\right)^2 + 0.12551\left(L/T\right) - 11.218$$

Appendix B: Equations for Calculating Correction Factors in the LEFM Model

Equations for calculating Y_b *and* Y_m at the deepest point of the semi-elliptical surface crack are presented below. For nomenclature, please refer to Figure 3.5. Y_m=FH, Y_b=F. These equations are adapted from the reference by Newman and Raju (1981)

$$F = \left[M_1 + M_2 \left(\frac{a}{T} \right)^2 + M_3 \left(\frac{a}{T} \right)^4 \right] f_\phi g f_w$$

Where

$$M_1 = 1.13 - 0.09 \left(\frac{a}{c} \right)$$

$$M_2 = -0.54 + \frac{0.89}{0.2 + (a/c)}$$

$$M_3 = 0.5 - \frac{1.0}{0.65 + (a/c)} + 14 \left(1.0 - \frac{a}{c} \right)^{24}$$

$$g = 1 + \left[0.1 + 0.35 \left(\frac{a}{T} \right)^2 \right] (1 - \sin\phi)^2$$

In Eqn. (1),

f_ϕ is an angular function from the embedded elliptical-crack solution, it is calculated as:

$$f_\phi = \left[\left(\frac{a}{c} \right)^2 \cos^2\phi + \sin^2\phi \right]^{1/4}$$

The function f_w, a finite-width correction is expressed as:

$$f_w = \left[\sec\left(\frac{\pi c}{2b} \sqrt{\frac{a}{T}} \right) \right]^{1/2}$$

The function H is assumed to have the form of Eqn. (2):

$$H = H_1 + (H_2 - H_1)\sin^p \phi$$

Where

$$p = 0.2 + \frac{a}{c} + 0.6\frac{a}{T}$$

$$H_1 = 1 - 0.34\frac{a}{T} - 0.11\frac{a}{c}(\frac{a}{T})$$

$$H_2 = 1 + G_1(\frac{a}{T}) + G_2(\frac{a}{T})^2$$

In the above equation for H_2

$$G_1 = -1.22 - 0.12\frac{a}{c}$$

$$G_2 = 0.55 - 1.05\left(\frac{a}{c}\right)^{0.75} + 0.47\left(\frac{a}{c}\right)^{1.5}$$

Appendix C: MATLAB code of MCMC sampling for the example on fatigue life prognosis of the Yellow Mill Pond Bridge, Connecticut, USA

This section presents the MATLAB codes used for MCMC sampling for fatigue life prognosis of the Yellow Mill Pond Bridge in this dissertation (MATLAB R2011b). A total of five MATLAB files are listed below, which are labeled as C.1-C.5 respectively. C.1 *Maincode.m* is the main code which calls functions from C.2-C.5 to draw samples from the posterior distribution of stochastic parameters using the Metropolis- Hastings algorithm.

C.1 Maincode

This MATLAB code: *Maincode.m*, implements the Bayesian updating and MCMC sampling for stochastic parameters in the degradation model (Metropolis et al 1953; Hastings 1970).

```
% Main code for Bayesian Updating of Fatigue Crack length growth model using MCMC
% unit: m, MPa, second
% last revised: April 7, 2013

clear all;
close all;
clc;
tic

%% Parameters Values Assignments
% C_old, C_new: old and new-proposed values in MCMC for the material related constant C
%   in Paris Law
% a0: initial crack length
% m: material related constant m factor in the Paris Law
% Sa: equivalent stress range (e.g., calculated using rainflow counting)
% miu_C, sigma_C: parameters for initial lognormal distribution of C factor
% miu_a0, sigma_a0: parameters for initial lognormal distribution of a0
% A_crck: crack length measurements;
% N_ldcycl: load cycle at crack length measurements;
% Y_ldcycl: year in service at crack length measurements
% VarMsm: variance of Brownian motion (Wiener Process) for measurement
%   error
```

```
% VarMdl: variance of Gaussian process for model error
% N_sample: total number of samples to be generated by MCMC method

m = 3;    %(Yazdani and Albrecht 1987)
Sa = 13.1;      %(Fisher, 1984)
A_crck = [0.9525*1e-2,1.27e-2];   %(Fisher et al 1981)
N_ldcycl = [2.65e7,3.35e7];
Y_ldcycl = trafficmodel(N_ldcycl);  %(Fisher et al 1981)
N_msample = numel(A_crck)-1;
VarMsm = (1e-4)^2;    % Wiener process for measurement error (Gebraeel et al 2005)
VarMdl = (1.5e-4)^2;  % Gussian process for model error
VAR_VEC = [VarMsm,VarMdl];

a0 = 0.0508e-2; % starting value of initial crack length for MCMC sampling
Cm = 3.92e-12; % starting value of material related constant C for MCMC sampling

[miu_a0,sigma_a0] = lognormal(0.0508e-2,(0.0508e-2*0.5)^2);  % Yazdani and Albrecht
(1987)
% Calculate mu and sigma of lognormal distribution parameters from mean and variance of
a0

[miu_C,sigma_C] = lognormal(3.92e-12,(3.92e-12*0.63)^2); % Yazdani and Albrecht (1987)
% Calculate mu and sigma of lognormal distribution parameters from mean
%   and variance of C

N_sample = 100000;

C_vec = zeros(N_sample,1);   % initialize space allocation for statistical sample generation of
C factor
a0_vec = zeros(N_sample,1); % initialize space allocation for statistical sample generation of
a0 factor

L1 = Cm; % distance coefficient for C factor in the Metropolis algorithm
L2 = a0; % distance coefficient for a0 factor in the Metropolis algorithm
reject = 0; % reject: number of rejected moves


%% Metropolis Algorithm for generating samples for a0 and C from posterior distribution
% Please refer to "Figure 5.2 Single loop of MCMC" in dissertation for details of the
algorithm

for simun = 1:N_sample

   %%%%% Metropolis algorithm (Start) (Metropolis et al 1953; Hastings 1970)

   % propose a move
   C_old = Cm;
   a0_old = a0;
   rndnum = 2*rand(1,2)-1;   % random # (1x2 matrix) generation, uniform distribution [-1, 1]

   C_new = Cm+0.05*rndnum(1,1)*L1; % C_new is the new value for C, 0.05 chosen from a
```

```
trial and error process
   a0_new = a0_old+0.3*rndnum(1,2)*L2; % a0_new is the new value for a0, 0.3 chosen
from a trial and error process
   %--------------------------------accept or reject the move
   if C_new <= 0 || a0_new <= 0,
      Cm = C_old;
      a0 = a0_old;
      reject = reject+1;
   else

   % generate a random # (uniform distribution)
   U = rand(1);

   % calculate f(a0',C' ...)/f(a0,C ...)
   a0_R = [a0_old,a0_new];
   C_R = [C_old,C_new];
   lklhd = LKD(A_crck,Y_ldcycl,N_ldcycl,VAR_VEC,a0_R,C_R,N_msample);
   pdf_new = lognpdf(C_new,miu_C,sigma_C)*lognpdf(a0_new,miu_a0,sigma_a0);
   pdf_old = lognpdf(C_old,miu_C,sigma_C)*lognpdf(a0_old,miu_a0,sigma_a0);
   ffratio = lklhd*(pdf_new/pdf_old);  %  Eqn (5.11) in dissertation

   % with probability min(1,ffratio), accept proposed move, otherwise, reject
   if ffratio > U
      Cm = C_new;
      a0 = a0_new;
   else
      Cm = C_old;
      a0 = a0_old;
      reject = reject+1;
   end
   %%%%% Metropolis algorithm (End)

   end

   C_vec(simun) = Cm;
   a0_vec(simun) = a0;
   disp(simun);

end
toc
```

C.2 ***Function: LKD***

This function *LKD.m* is called by *maincode.m* to calculate the likelihood function ratio between that of proposed new parameters values and old parameter values in MCMC sampling.

```
function [lklhd]=LKD(A_crck,Y_ldcycl,N_ldcycl,VAR_VEC,a0_R,C_R,N_msample)
% LKD is used to calculate the likelihood function value for Bayesian updating
% last revised: April 7, 2013

% C_old, C_new: old and proposed values for the material constant, C factor
% a0_old, a0_new: old and proposed values for initial crack length
% A_crck: crack length measurement vector;
% N_ldcycl: No. of load cycles;
% lklhd: likelihood function ratio in MCMC
% VarMsm: variance of Brownian motion (Wiener Process) for measurement
%   error
% VarMdl: variance of Gaussian process for model error

C_old = C_R(1);
C_new = C_R(2);
a0_old = a0_R(1);
a0_new = a0_R(2);
VarMsm = VAR_VEC(1);
VarMdl = VAR_VEC(2);
a_old = crackestimate(C_old,a0_old,N_ldcycl); % a_old, a_new: crack lengths from fatigue model calculation.
a_new = crackestimate(C_new,a0_new,N_ldcycl); % a_old, a_new: crack lengths from fatigue model calculation.

% crack length increment Ad,adold,adnew calculation
Yd_ldcycl = zeros(N_msample,1);
Ad_crck = zeros(N_msample,1);
ad_old = zeros(N_msample,1);
ad_new = zeros(N_msample,1);

for i = 1:N_msample
        Yd_ldcycl(i) = Y_ldcycl(i+1)-Y_ldcycl(i);
        Ad_crck(i) = A_crck(i+1)-A_crck(i);
        ad_old(i) = a_old(i+1)-a_old(i);
        ad_new(i) = a_new(i+1)-a_new(i);
end

% likelihood function ratio
lklhd = exp((-sum((Ad_crck-
ad_new).^2./(2*(VarMsm*Yd_ldcycl+2*VarMdl))))+sum((Ad_crck-
ad_old).^2./(2*(VarMsm*Yd_ldcycl+2*VarMdl))))...
   *exp(-(A_crck(1)-a_new(1)).^2./(2*VarMsm*Y_ldcycl(1)+2*VarMdl)+(A_crck(1)-
a_old(1)).^2./(2*VarMsm*Y_ldcycl(1)+2*VarMdl));
```

C.3 ***Function: crackestimate***

This function *crackestimate.m* is called by *LKD.m* to calculate the crack length given the values for the parameters of the degradation model.

```
function [a] = crackestimate(C,a0,N)
% crackestimate(C,a0,N) is to calculate crack length as given loading cycle using
% Paris Law
% Last revised: April 8.2013

%% Parameter assignments
% C: material property of coefficient C;
% a0: initial crack length a0;
% N: load cycle;
% k: number of data points;
% Sa:equivalent stress range;
Sa = 13.1;
m = 3;
k = numel(N); %Length of measurements vector

%% crack length estimation by fzero command.
val = C*Sa^m*N;
a = zeros(1,k);

warning off %#ok<WNOFF>
for i = 1:k
   yu = val(i);                % Right of equation: CS^m(N-N0)
   g = @(x)quadl('crctfct',a0,x)-yu; % Left of equation: integration of
da/[(F(a,Y)*sqrt(Pi*a)]^m
   x = fzero(g,[a0+0.00001,a0+500]);    % crack lengths calculation from fatigue model given
No. of cycles
   a(i) = x;
end
```

C.4 ***Function: crctfct***

This function *crctfct.m* is called by *crackestiamte.m* to calculate the correction factor and then get the whole integar for Paris Law equation.

```
function f = crctfct(x)
% crctfct(x) is to calculate the correction factor and then get the whole integar for Paris Law
equation
% Last revised: April.07 2013

%% correction factor calculation
% c=5.457*a^1.133: aspect ratio relation
% Fe:elliptical crack front correction;1/E(k); curve fitting equation used
% Fs:front free surface correction factor; 1.211-0.186*sqrt(a/b);
% Fw:back free surface correction factor; 1.0
% Fg:stress gradient correction factor; SCF/(1+6.789*(a/Tf)^0.4348);
% SCF=-3.539*log(Z/Tf)+1.981*log(Tcp/Tf)+5.798;
% x: miner axis of the semi-elliptical crack (i.e., crack depth)
```

```
% Z:weld leg size. Tcp=cover-plate thickness; Tf=flange thickness
% Fe, Fs, Fw, Fg, refer to Fisher 1984

Z = 0.6*0.0254;
Tf = 1.26*0.0254;
Tcp = 1.25*0.0254;
Fe = 1./(7.5925e5*x.^4-6.0615e4*x.^3+1.7536e3*x.^2-23.4131*x+1.2976);
Fs = 1.211-0.186*sqrt(x./(5.457.*x.^1.133));
Fw = 1;
SCF = -3.539.*log(Z./Tf)+1.981.*log(Tcp./Tf)+5.798;
Fg = SCF./(1+6.789.*(x./Tf).^0.4348);

%% whole integar: da/[(F(a,Y)*sqrt(Pi*a)]^m
f = (Fe.*Fs.*Fw.*Fg.*sqrt(pi.*x)).^-3;
```

C.5 ***Function: trafficmodel***

This function *trafficmodel.m* is to transfer fatigue load cycle into years.

```
function [Yrs] = trafficmodel(CycleT)
% trafficmodel is used to transfer load cycle into years interval.
% for Yellow Mill Pond Bridge.
% Last revised: April.7.2013

% Exponential Traffic Growth Model is used. Annual Traffic increase rate is
% set as 3.47%  @1970: ADTT=5660; @2008: ADTT=20692;

a1 = 5660*1.0347^(-1970+1958); % 3760is the ADTT at the 1st year(1958).
q = 1.0347;  %
% M = a1*q.^(n-1)*365;  % Yearly total load cycle vector
% S = a1*(1-q.^n)/(1-q)*365;  % Total load cycle up to year vector

Yrs = zeros(1,numel(CycleT));

for i = 1:numel(CycleT)
   g = @(x)a1*(1-q.^x)/(1-q)-CycleT(i)/365;
   x = fzero(g,[-1 2000]);
   Yrs(i) = x;
end
```

C.6 ***Function: lognormal***

This function *lognormal.m* is to calculate the coefficients for lognormal distribution.

```
function [miu,sigma] = lognormal(Ex,Varx)
% lognormal is used to calculate the coefficients for lognormal distribution
% Last revised: June.16.2010
% Ex, Varx: mean value and variance for lognormal distribution
```

```
% miu, sigma: coefficients for lognormal distribution

miu = log(Ex)-0.5*log(1+Varx/Ex^2);
sigma = sqrt(log(1+Varx/Ex^2));
```

Bibliography

AASHTO (American Association of State Highway Transportation). (2004). *LRFD Bridge Design Specifications and Commentary, 3rd Edition*, Washington, D.C., USA.

Aghakouchak, A. A. & Stiemer, S. F. (2001). Fatigue reliability assessment of tubular joints of existing offshore structures. *Canadian Journal of Civil Engineering*, *28*(4), 691-698.

Alderson, J. L. (1999). Fatigue study of cantilevered traffic signal mast arms (Doctoral dissertation, University of Missouri-Columbia).

Archer, G. & Gurney, M. (1970). Fatigue strength of mild steel fillet welded tube to plate joints, *Metal Construction*, *2*(5), 207-210.

Barsom, J. M. & Novak, S. R. (1977) *Subcritical crack growth in steel bridge members* (NCHRP Report 181). Washington, DC: Transportation Research Board, National Research Council.

Bell, A. F., Naylor, M., Heap, M. J. & Main, I. G. (2011). Forecasting volcanic eruptions and other material failure phenomena: an evaluation of the failure forecast method. *Geophysical Research Letters*, *38*(15), L15304.

Bowness, D. & Lee, M. M. K. (1999). *Weld toe magnification factors for semi-elliptical cracks in T-butt joints* (OTO Report 99 014). Bootle, Merseyside, UK: Health and Safety Executive

Chotickai, P. (2005). *Fatigue reliability-based analysis methods for the evaluation of steel bridge structures*. (Doctoral dissertation, Purdue University).

Chung, H. Y. (2005). Fatigue reliability and optimal inspection strategies for steel bridges (Doctoral dissertation, the University of Texas at Austin).

Chung, H. Y., Manuel, L. & Frank, K. H. (2006). Optimal inspection scheduling of steel bridges using nondestructive testing techniques. *Journal of Bridge Engineering*, *11*(3), 305-319.

Cobb, A. C., Michaels, J. E. & Michaels, T. E. (2009, March). Ultrasonic structural health monitoring: a probability of detection case study. In *AIP Conference Proceedings* (Vol. 1096, p. 1800).

Coppe, A., Haft, R. T., Kim, N. H. & Yuan, F. G. (2009, May). Statistical characterization of damage propagation properties in structural health monitoring. *11th AIAA Non-Deterministic Approaches Conference*, Palm Springs, CA.

Cornelius, R. R. & Scott, P. A. (1993). A materials failure relation of accelerating creep as empirical description of damage accumulation. *Rock mechanics and rock engineering*, *26*(3), 233-252.

Culp, J., Witteveen, M. & Wong, H. L. (1990). *Action Plan for Cantilever Sign Problem* (Report to Management). Lansing, MI: Michigan Department of Transportation).

Cremona, C. (1996). Reliability updating of welded joints damaged by fatigue. *International journal of fatigue*, *18*(8), 567-575.

Dauner, H. G., Oribasi, A. & Wery, D. (1998). The Lully Viaduct, a composite bridge with steel tube truss. *Journal of constructional steel research*, *46*, 67-68.

Deschamp, B. (2002) Fatigue testing of traffic signal structures, (Master Thesis, University of Wyoming)

Dekkers, A. L. M., Einmahl, J. H. J. & De Haan, L. (1989). A moment estimator for the index of an extreme-value distribution. *Annals of Statistics*, *17*:1833-55.

Dexter, R. J. & Ricker, M. J. (2002). *Fatigue-resistant design of cantilevered signal, sign, and light supports* (NCHRP Report 469). Washington, DC: Transportation Research Board of the National Academies.

Doksum, K. A. & Hoyland, A. (1993). Models for variable-stress accelerated life testing experiments based on Wiener processes and the inverse Gaussian distribution. *Theory of Probability & Its Applications*, *37*(1), 137-139.

Engesvik, K. M. & Moan, T. (1983). Probabilistic analysis of the uncertainty in the fatigue capacity of welded joints. *Engineering Fracture Mechanics*, *18*(4), 743-762.

Enright, M. P. & Frangopol, D. M. (1999). Condition prediction of deteriorating concrete bridges using Bayesian updating. ASCE *Journal of Structural Engineering*, *125*(10):1118–1125.

Fisher, J. W., Hausammann, H., Sullivan, M. D. & Pense, A. W. (1979). *Detection and Repair of Fatigue Damage in Welded Highway Bridges* (NCHRP Report 206). Washington, DC: Transportation Research Board of the National Academies.

Fisher, J. W., Kulak, G. L. & Smith, I. F. (1998). *A fatigue primer for structural engineers*. Chicago, IL: National Steel Bridge Alliance.

Fisher, J. W., Pense, A. W., Hausammann, H. & Slockbower, R. E. (1981). Long time observation of a fatigue damaged bridge. *Journal of the Technical Councils of ASCE*, *107*(1), 55-71.

Fisher, J. W. (1984). *Fatigue and fracture in steel bridges. Case studies*. Sussex, England: Wiley (John) & Sons, Limited.

Forman, R. G., Kearney, V. E. & Engle, R. M. (1967). Numerical analysis of crack Propagation in cyclic-loaded structures. *Journal of basic Engineering*, *89*(3), 459-464.

Fouad, F. H., Davidson, J.S., Delatte, N., Calvert, E.A., Chen, S. Nunez, E. & Abdalla, R. (2003). *Structural supports for highway signs, luminaires, and traffic signals* (NCHRP Report 494). Washington, DC: Transportation Research Board of the National Academies.

Frangopol, D. M., Strauss, A. & Kim, S. (2008). Use of Monitoring Extreme Data for the Performance Prediction of Structures: General Approach. *Engineering Structures*, *30*, 3644-53.

Gebraeel, N. Z., Lawley, M. A., Rong, L. I. & Jennifer, K. (2005). Residual-life distributions from component degradation signals: A Bayesian approach. *IIE Transactions*, *37*(6), 543-557.

Gelman, A. & Shirley, K. (2010). Inference from simulations and monitoring convergence. *Handbook of Markov Chain Monte Carlo: Methods and Applications*(131-143). (Brooks, S. Editor, Gelman, A. Editor, Jones, G.L. Editor & Meng, X. Editor (Eds)), Boca Raton, FL: Chapman & Hall/CRC.

Gilani, A. & Whittaker, A. (2000)a. Fatigue-life evaluation of steel post structures. I: Background and analysis. *Journal of Structural Engineering*, *126*(3), 322-330.

Gilani, A. & Whittaker, A. (2000)b. Fatigue-life evaluation of steel post structures. II: Experimentation. *Journal of Structural Engineering*, *126*(3), 331-340.

Gilks, W. R., Richardson, S. & Spiegelhalter, D. (Eds.). (1996). *Markov Chain Monte Carlo in practice: interdisciplinary statistics*. Boca Raton, FL: Chapman & Hall/CRC.

Guan, X., Jha, R. & Liu, Y. (2012). Probabilistic fatigue damage prognosis using maximum entropy approach. *Journal of Intelligent Manufacturing*, *23*(2), 163-171.

Harlow, D. G. & Wei, R. P. (2001). Probability modelling and statistical analysis of damage in the lower wing skins of two retired B‐707 aircraft. *Fatigue & Fracture of Engineering Materials & Structures*, *24*(8), 523-535.

Hastings, W. K. (1970). Monte Carlo sampling methods using Markov chains and their applications. *Biometrika, 57*(1), 97-109.

Hill, B. M. (1975). A simple general approach to inference about the tail of a distribution. *Annals of Statistics, 3,* 1163-74.

Hosking, J. R. M. & Wallis, J. R. (1987). Parameter and quantile estimation for the Generalized Pareto Distribution. *Technometrics, 29,*339-49.

Kaczinski, M. R., Dexter, R. J. & Van Dien, J. P. (1998). *Fatigue-resistant design of cantilevered signal, sign and light supports* (NCHRP Report 412). Washington DC: Transportation Research Board of the National Academies.

Keating, P. B. & Fisher, J. W. (1986). *Evaluation of fatigue tests and design criteria on welded details*. (NCHRP Report 286). Washington DC: Transportation Research Board of the National Academies.

Kilbum, C. R. & Voight, B. (1998). Slow rock fracture as eruption precursor at Soufriere Hills volcano, Montserrat. *Geophysical Research Letters, 25*(19), 3665-3668.

Kirkemo, F. (1988). Applications of probabilistic fracture mechanics to offshore structures. *Applied Mechanics Reviews, 41,* 61.

Klingerman, D. J. & Fisher, J. W. (1973). *Threshold crack growth in A36 steel* (No. FEL-386.2 Intrm Rpt.). Bethlehem, PA: Lehigh University.

Ko, J. M. (2003), Health monitoring and intelligent control of cable-supported bridges, *in Proceedings of the First International Conference on Structural Health Monitoring and Intelligent Infrastructure*, Tokyo, Japan.

Koenigs, M. T. (2003). Fatigue resistance of traffic signal mast-arm connection details (Doctoral dissertation, University of Texas at Austin).

Law, D. W., Cairns, J., Millard, S. G. & Bungey, J. H. (2004). Measurement of loss of steel from reinforcing bars in concrete using linear polarisation resistance measurements. *NDT & E International*, *37*(5), 381-388.

Lu, C. J. & Meeker, W. O. (1993). Using degradation measures to estimate a time-to-failure distribution. *Technometrics*, *35*(2), 161-174.

Madsen, H.O. (1987). "Model updating in reliability theory," *Proceeding of ICASP-5*, *Vancouver*, Canada.

MATLAB version R2011b (7.13.0.564), Natick, Massachusetts: The MathWorks Inc., 2011

Main, I. G. (2007). A modified Griffith criterion for the evolution of damage with a fractal distribution of crack lengths: application to seismic event rates and b - values. *Geophysical journal international*, *107*(2), 353-362.

Metropolis, N., Rosenbluth, A. W., Rosenbluth, M. N., Teller, A. H. & Teller, E. (1953). Equation of state calculations by fast computing machines. *The journal of chemical physics*, *21*, 1087.

Milgrom, P. R. (1981). Good news and bad news: Representation theorems and applications. *The Bell Journal of Economics*, 380-391.

Miner, M. A. (1945). Cumulative damage in fatigue. *Journal of applied mechanics*, *12*(3), 159-164.

Moan, T. & Song, R. (2000). Implications of inspection and repair on system fatigue reliability of offshore structures. *Journal of Offshore Mechanics and Arctic Engineering*, *122*,173-180.

Ocel, J. M., Dexter, R. J. & Hajjar, J. F. (2006). *Fatigue-resistant design for overhead signs, mast-arm signal poles, and lighting standards* (No. MN/RC-2006-07). St. Paul, MN: Minnesota Department of Transportation.

Paris, P. C., Gomez, M. P. & Anderson, W. E. (1961). A rational analytic theory of fatigue. *Trends of Engineering*, *13*, 9-14.

Perrin, F., Sudret, B. & Pendola, M. (2007). Bayesian updating of mechanical models-Application in fracture mechanics. *18ème Congrès Français de Mécanique*, Grenoble, France.

Raju, I. S. & Newman, J. C. (1979). Stress-intensity factors for a wide range of semi-elliptical surface cracks in finite-thickness plates. *Engineering Fracture Mechanics*, *11*(4), 817-829.

Resnick, S. (1997). Heavy tail modeling and teletraffic data. *The Annals of Statistics*, *25*, 1805-1849.

Righiniotis, T. D. & Chryssanthopoulos, M. K. (2003). Probabilistic fatigue analysis under constant amplitude loading. *Journal of Constructional Steel Research*, *59*(7), 867-886.

Robinson, M. E. & Crowder, M. J. (2000). Bayesian methods for a growth-curve degradation model with repeated measures. *Lifetime Data Analysis*, *6*(4), 357-374.

Romeijn A. (1994). *Stress and strain concentration factors of welded multiplanar tubular joints*. (Doctoral dissertation. The Netherlands: Delft University of Technology).

Sachs, N. W. (2005). Understanding the surface features of fatigue fractures: how they describe the failure cause and the failure history. *Journal of Failure Analysis and Prevention*, *5*(2), 11-15.

Satyanarayan, L., Sridhar, C., Krishnamurthy, C. V. & Balasubramaniam, K. (2007). Simulation of ultrasonic phased array technique for imaging and sizing of defects using longitudinal waves. *International Journal of Pressure Vessels and Piping*, *84*(12), 716-729.

Sobczyk, K. & Spencer Jr, B. F. (1992). *Random fatigue: from data to theory*. San Diego, CA: Academic Pr, INC.

South, J. (1997). *Fatigue of tube-to-plate fillet welds and methods for their improvemen* (Physical Research Report No. 118). Springfield, IL: Illinois Department of Transportation

Strauss, A., Frangopol, D. M. & Kim, S. (2008). Use of monitoring extreme data for the performance prediction of structures: Bayesian updating. *Engineering Structures*, *30*(12), 3654-3666.

Schumacher, A. & Nussbaumer, A. (2006). Experimental study on the fatigue behaviour of welded tubular K-joints for bridges. *Engineering structures*, *28*(5), 745-755.

Shetty, N. K. & Baker, M. J. (1990). Fatigue Reliability of Tubular Joints in Offshore Structures: Reliability Analysis. *In Proceedings of the 9th International Conference on Offshore Mechanics and Arctic Engineering*, *ASME*, Vol. 2, Houston, USA (pp. 223-230).

Shinozuka, M. (1983). Basic analysis of structural safety. *Journal of Structural Engineering*, *109*(3), 721-740.

Steel, R. G. D. & Torrie, J. H. (1980). *Principles and procedures of statistics: a biometrical approach 2nd Edition*. New York, NY: McGraw-Hill

Virkler, D. A., Hillberry, B., & Goel, P. K. (1978). *The statistical nature of fatigue crack propagation* (Technique Report AFFDL-TR-78-43). West Lafayette, IN: Purdue University.

Vosikovsky, O., Bell, R., Burns, D. J. & Mohaupt, U. H. (1985). Fracture mechanics assessment of fatigue life of welded T-Joints, including thickness effect. *In Proceedings of the 4th international conference on the behavior of offshore structures*. Delft, the Netherland.

Walbridge, S. (2005). *A probabilistic study of fatigue in post-weld treated tubular bridge structures* (Doctoral dissertation, Ecole Polytechnique Federale De Lausanne (EPFL), Lausanne, Switzerland)

Walbridge, S. & Nussbaumer, A. (2007). A probabilistic model for determining the effect of post-weld treatment on the fatigue performance of tubular bridge joints. *International journal of fatigue*, *29*(3), 516-532.

Wang, C., Yu, X., Feng Y. & Liu, X. (2008 July). Fatigue reliability updating through inspections and monitoring data of steel bridges, *Proc. IAMBAS2008: Bridge Maintenance, Safety, Management, Health Monitoring and Informa*tics – Koh & Frangopol (eds), Seoul, Korea.

Whitmore, G. A. (1995). Estimating degradation by a Wiener diffusion process subject to measurement error. *Lifetime Data Analysis*, *1*(3), 307-319.

Voight, B. (1989). A relation to describe rate-dependent material failure. *Science*, *243*, 200-203.

Yazdani, N. & Albrecht, P. (1987). Risk analysis of fatigue failure of highway steel bridges. *Journal of Structural Engineering*, *113*(3), 483-500.

Zhang, R. & Mahadevan, S. (2000). Model uncertainty and Bayesian updating in reliability-based inspection, *Structural Safety*, *22*(2), 145-160

Zhao, X. L., Herion, S., Packer, J. A. & Puthli, R. S. et al. (2001). *Design guide for circular and rectangular hollow section welded joints under fatigue loading*. Koln, Germany.

Zhao, Z., Haldar, A. & Breen Jr, F. L. (1994). Fatigue-reliability updating through inspections of steel bridges. *Journal of Structural Engineering*, *120*(5), 1624-1642.

Zhao, Z. & Haldar, A. (1996). Bridge fatigue damage evaluation and updating using non-destructive inspections. *Engineering fracture mechanics*, *53*(5), 775-788.

Zheng, R. & Ellingwood, B. R. (1998). Role of nondestructive evaluation in time-dependent reliability analysis. *Structural Safety*, 20(4), 325–339.